

Longitudinal Diffeomorphic Fetal Brain Atlas Learning for Tissue Labeling using Geodesic Regression and Graph Cuts

DIPLOMARBEIT

zur Erlangung des akademischen Grades

Diplom-Ingenieurin

im Rahmen des Studiums

Medizinische Informatik

eingereicht von

Roxane Licandro

Matrikelnummer 0442108

an der Fakultät für Informatik der Technischen Universität Wien

Betreuung: Ao. Univ. Prof. Dipl.-Ing. Dr. techn. Robert Sablatnig

Mitwirkung: Ass. Prof. Dipl.-Ing. Dr. techn. Georg Langs

Dipl.-Ing. Ernst Schwartz

Wien, 22.10.2015

(Unterschrift Verfasserin)

(Unterschrift Betreuung)

Longitudinal Diffeomorphic Fetal Brain Atlas Learning for Tissue Labeling using Geodesic Regression and Graph Cuts

MASTER'S THESIS

submitted in partial fulfillment of the requirements for the degree of

Diplom-Ingenieurin

in

Medical Informatics

by

Roxane Licandro

Registration Number 0442108

to the Faculty of Informatics
at the Vienna University of Technology

Advisor: Ao. Univ. Prof. Dipl.-Ing. Dr. techn. Robert Sablatnig

Assistance: Ass. Prof. Dipl.-Ing. Dr. techn. Georg Langs

Dipl.-Ing. Ernst Schwartz

Vienna, 22.10.2015

(Signature of Author)

(Signature of Advisor)

Erklärung zur Verfassung der Arbeit

Roxane Licandro
Nussdorferstraße 53 Top 27, 1090 Wien

Hiermit erkläre ich, dass ich diese Arbeit selbständig verfasst habe, dass ich die verwendeten Quellen und Hilfsmittel vollständig angegeben habe und dass ich die Stellen der Arbeit - einschließlich Tabellen, Karten und Abbildungen -, die anderen Werken oder dem Internet im Wortlaut oder dem Sinn nach entnommen sind, auf jeden Fall unter Angabe der Quelle als Entlehnung kenntlich gemacht habe.

(Ort, Datum)

(Unterschrift Verfasserin)

Acknowledgements

I want to thank my supervisor Georg Langs at the Medical University of Vienna. His lectures and exercises on medical image processing and the inspiring discussions during my practical training project, woke my fascination for this field of research during my study. I appreciate the chance he gave me to work on the interesting field of fetal brain development, which motivated me every day. I also want to thank Ernst Schwartz for the ongoing support, his helpful advice and the guidance through the jungle of mathematical formulations. It was a great pleasure to work with them. Acknowledgements to my supervisor Robert Sablatnig at the Vienna University of Technology. His profound knowledge and encouragement in the scientific working progress have been of great value for me. The demanded accurate work and challenges constantly pushed myself to new limits.

I also want to thank Walter G. Kropatsch and the Pattern Recognition Image Processing Group of the University of Technology Vienna for providing me an insight into the working field of research during my employment, inspiring discussions and friendly support.

I am grateful to my parents Margit and Gianfranco Licandro, who supported me my whole life and made all this possible. Thank you for your love, financial support and time. Words are not able to express my appreciation for everything you have done.

Thanks to Michael Koutensky for his motivation, loving encouragement, patience and for being my tower of strength during the working progress. He gave me the forces to brake down the upcoming barriers. I also want to thank Hilda Koutensky for her support during the proof reading process and the valuable feedback.

In loving memory of Alfred Koutensky. He always believed in me and shared the same excitement for mathematics and geometry. With his passing, during the writing of this master's thesis, I lost a friend and soulmate. Thank you for your support and I hope to see you again in another dimension.

Abstract

The human brain undergoes structural changes in size and in morphology between the second and the third trimester of pregnancy, according to accelerated growth and the progress of cortical folding. The most accurate non-invasive method for observing these events is the fast Magnetic Resonance (MR) imaging technique. It allows to image a fetus within 20 seconds and consequently reduce artefacts, caused by the fetal movement. A problem of MR imaging is the lack of comparability and constancy of gray-values. To make fetal brains comparable, atlases are used as a standard space for studying brain development, fetal pathology locations, fetal abnormalities or anatomy. The fetal atlas building process takes into account both inter-patient variability of brain shapes and the gestational age dependent structural changes. Thus, a time-varying atlas is required. The aim of the work is to provide a continuous model of brain development and to use it as base for an automatic tissue labeling framework. This master's thesis provides a novel longitudinal fetal brain atlas construction concept for geodesic image regression using three different age-ranges which are parametrized according to the developmental stage of the fetus. The dataset used for evaluation contains 45 T2-weighted 1.5 Tesla MR images between Gestational Week (GW) 18.0 and GW 30 day 2. The proposed tissue labeling framework uses the learned spatio-temporal atlas as cost term in a graph cut based annotation procedure to automatically segment cortical and ventricle brain tissue. The automatic tissue labeling framework estimates cortical segmentations with a Dice Coefficient (DC) up to 0.85 and ventricle segmentations with a DC up to 0.60.

Kurzfassung

Das Gehirn eines Fötus weist während des zweiten und dritten Schwangerschaftstrimesters Veränderungen sowohl in der Größe als auch Morphologie auf, welche auf Wachstumsprozesse des Hirnes und Faltungsprozesse der Hirnoberfläche zurück zu führen sind. Eine geeignete Aufnahmemodalität für das Hirn des Fötus ist die beschleunigte Magnetresonanztomographie. Sie ermöglicht es auf nicht invasivem Weg Bilder innerhalb von 20 Sekunden aufzunehmen, um Bewegungsartefakten, erzeugt durch die fetale Bewegung, entgegen zu wirken. Diese Technik weist jedoch ein Problem der Konstanz von Grauwerten für gleiche Strukturen auf. Um fetale Hirne vergleichen zu können wird ein Atlas als ein Referenzmodell verwendet, welcher daraufhin die Untersuchung der Gehirnentwicklung, fetaler Pathologielokalisationen, von Abnormalitäten des Fötus oder dessen Hirnanatomie ermöglicht. Bei der Erstellung eines Atlas für das Hirn eines Fötus müssen sowohl die strukturellen Veränderungen in Form und Größe als auch patientenbezogene Unterschiede des Hirnes einbezogen werden. Daher ist es Ziel dieser Masterarbeit ein kontinuierliches Modell der Hirnentwicklung zu erstellen, um dieses als Ausgang für die automatisierte Markierung von Hirnstrukturen zu verwenden, welches in einem selbsterstellten Framework integriert ist. Diese Arbeit stellt ein neues Konzept zur Berechnung eines spatio-temporalen fotalen Hirnatlas' unter der Verwendung von geodätischer Bildregression vor. Anhand der Analyseergebnisse des Atlasbildungsprozesses werden drei Altersgruppen definiert, um gezielt drei unterschiedliche Atlanten angepasst auf den Entwicklungsstatus des fetalen Hirns zu modellieren. Der für die Evaluierung verwendete Datensatz besteht aus 45 T2 gewichteten 1.5 Tesla Magnetresonanz-Bildern von Föten im Alter zwischen 18 und 30 Schwangerschaftswochen. Das vorgestellte Framework verwendet den berechneten Atlas als Kostenterm in einem Graph Cut Ansatz um automatisiert kortikale Hirnstrukturen und Ventrikel zu segmentieren. Vom Framework automatisiert bestimmte Segmentierungen für Kortexstrukturen weisen einen Dice Koeffizienten bis zu 0.85 und für Ventrikelstrukturen bis zu 0.60 auf.

Contents

1	Introduction	1
1.1	The Development of the Brain	1
1.2	Motivation and Problem Statement	4
1.3	Aim of the Work	5
1.4	Methodical Approach	5
1.5	Related Works	6
1.6	Results	7
1.7	Structure of the Thesis	7
2	State-of-the-art	9
2.1	Concept of Atlases	9
2.2	Atlases of the Developing Brain	13
2.3	Discussion	16
2.4	Spatio-temporal Atlas Construction	19
2.5	Relation to this Thesis	21
2.6	Summary	23
3	Image Registration and Diffeomorphisms	25
3.1	Denotation	25
3.2	Overview of Image Registration Methods	26
3.3	Large Deformations Diffeomorphic Metric Mapping	32
3.4	Geodesic Shooting	34
3.5	Geodesic Regression	34
3.6	Summary	35
4	Image Segmentation and Graphcuts	37
4.1	Denotation	37
4.2	Overview of Image Segmentation Methods	37
4.3	Binary Graph Cuts	40
4.4	Multi Label Graph Cuts	41
4.5	Potts Models	42
4.6	Continuous Max-Flow Model	43
4.7	Summary	44

5 Preliminary Experiments	45
5.1 Experiment 1: Analysis Regarding the Composition of Vector Fields	47
5.2 Experiment 2: Analysis Regarding the Preprocessing of Template and Target Images	49
5.3 Experiment 3: Analysis Regarding the Dependence Between GW Difference and Registration Result	52
5.4 Experiment 4: Analysis Regarding the Initialisation of Combination of Registration Procedures	54
5.5 Summary	56
6 Automatic Tissue Labeling Framework	57
6.1 Magnetic Resonance Imaging (MRI) Acquisition Setup	59
6.2 Preprocessing	60
6.3 Learning a Continuous Model of Fetal Brain Development	62
6.4 Automatic Tissue Labeling using Graph Cuts	76
6.5 Summary	84
7 Evaluation of the Tissue Labeling Framework	85
7.1 Evaluation of the Continuous Model of Fetal Brain Development	86
7.2 Evaluation of the Tissue Labeling Procedure	99
7.3 Summary and Contributions	108
7.4 Conclusion	109
7.5 Future Work	110
A Acronyms	113
Bibliography	115

Introduction

This chapter starts with an introduction to the medical background of the fetal brain development studied in this master's thesis. The occurring problems and motivation to tackle these are summarised and a brief overview of the work and methodical approach to build a tissue labeling framework for fetal brains are given. The chapter continues with an enumeration of state-of-the-art approaches and related work and concludes with a report on the results achieved.

1.1 The Development of the Brain

The development of the human brain starts in the embryonic phase (GW one to eight). In the first GW, the fertilised egg divides several times and forms a blastocyst (cell ball) [55]. In the second week of gestation these cells begin to differentiate and form a three tissue (ectoderm, mesoderm, endoderm) layered elongated disk, also called embryonic disc [7]. The thickening of the dorsal ectoderm on the human embryonic disc in the third GW (~ 16 Gestational Days (GD)) leads to the forming of a neural plate, from which the nervous system develops [55]. At the beginning of the fourth GW the neural plate starts to fold and evolves from the neural groove to the neural tube [55]. The caudal part of the neural tube becomes the spinal chord and the rostral portion differentiates into the three primary brainvesicles: prosencephalon (forebrain), mesencephalon (midbrain), rhombencephalon (hindbrain) [55] [49] (cf. Figure 1.1). In the fifth and sixth GW the brain vesicles distinguish and become the secondary brain vesicles [7]: Telencephalon and diencephalon emerge from the proencephalon, mesencephalon remains one structure and metencephalon and myelencephalon are the separated parts of the rhombencephalon. Starting in GW 6, the outline of the nervous system becomes apparent. In the second and third gestational month, the brain grows rapidly and attains its rough adult shape [49]. The myelencephalon develops into the medulla, the metencephalon into the pons and the cerebellum. The pons connects the telencephalon with the cerebellum and the medulla oblongata [49]. The diencephalon differentiates into the thalamus and hypothalamus. The telencephalon consists of two hemispheres

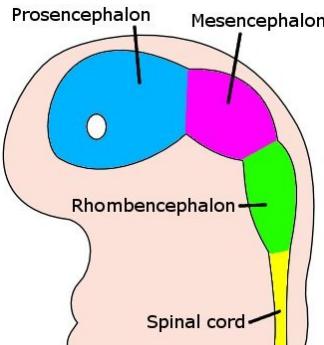


Figure 1.1: Illustration of the primary brain vesicles of an embryo at GW 4¹.

and contains the motor centres (basal nuclei), hippocampus, amygdala and the cerebral cortex. It shows a rapid growth in the fetal stadium and covers the diencephalon in the third, the mesencephalon in the sixth and the metencephalon in the eighth gestational month [49]. The cortex cerebri consists of the White Matter (WM) on the in- and the Gray Matter (GM) on the outside. The WM is made up of nerve fibers, the GM consists of the neuronal cellbodies, glia cells and capillary vessels [7] [49]. The structural changes of the fetal cortex during the second and third trimester of pregnancy are illustrated in Figure 1.2. The cortical surface area increases during the cortical folding processes [73]. The smooth surface of the cerebral cortex at GW 11 first starts to fold and expands [20] between GW 25 and 30 [80]. This process continues with a moderate organised formation of gyri and sulci (gyrification) [20] which concludes within the first two years of life [47]. The Central Sulcus (CeS), sulcus lateralis also called Sylvian Fissure (SF), ParietoOccipital Sulcus (POS) and preoccipital notch divide the brain into four lobes, which are illustrated in Figure 1.3a. Figure 1.3b illustrates the gyri and lobes of the brain: Frontal Lobe (FL) (yellow), Parietal Lobe (PL) (red), Occipital Lobe (OL) (purple) and temporal lobe (green). The ventricle system of the human brain evolves from the neural canal and is illustrated in Figure 1.4. It lies in the neural tube and is divided into segments, which remain connected. The rhombencephalon segment of the neural canal becomes the fourth ventricle with a rhombus shaped ground. The canalis centralis is in the medulla segment. A tight canal named aqueductus mesencephali lies in the midbrain. The diencephalon hosts the third ventricle and the lateral ventricles sit in the cerebrum hemispheres. Ventricles produce CerebroSpinal Fluid (CSF), which protects the brain from hitting against the cranial bone, has temperature regulatory functions and serves as nutrition for the neural tissue. Ventricles are also interesting for the image acquisition with MR, as they are easy to distinguish and indicators for diseases and brain development [7] [49].

Quantification of fetal brain development

For measuring the fetal brain growth and for quantifying the folding progress, shape descriptors and curvature-based folding measures are used in state-of-the-art approaches [80], [20], [19],

¹Image taken from https://upload.wikimedia.org/wikipedia/commons/4/4c/4_week_embryo_brain.jpg [assessed 21-September-2015]

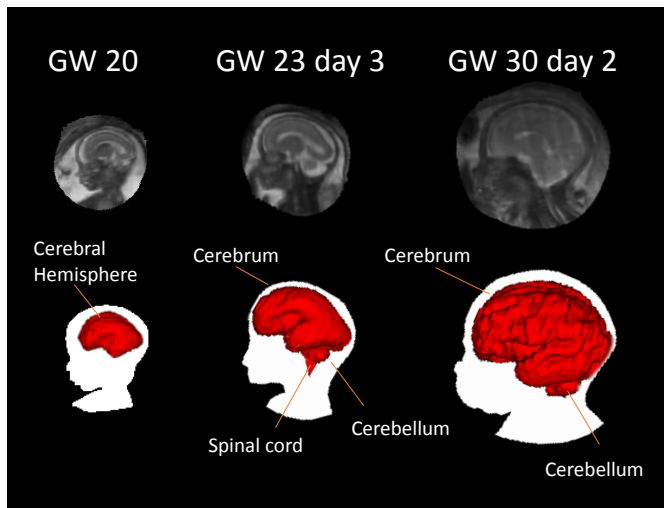


Figure 1.2: MRI and schematic illustration of the fetal brain development at GW 20, 23 day 3 and 30 day 2. MR images courtesy of Medical University of Vienna (MUW).

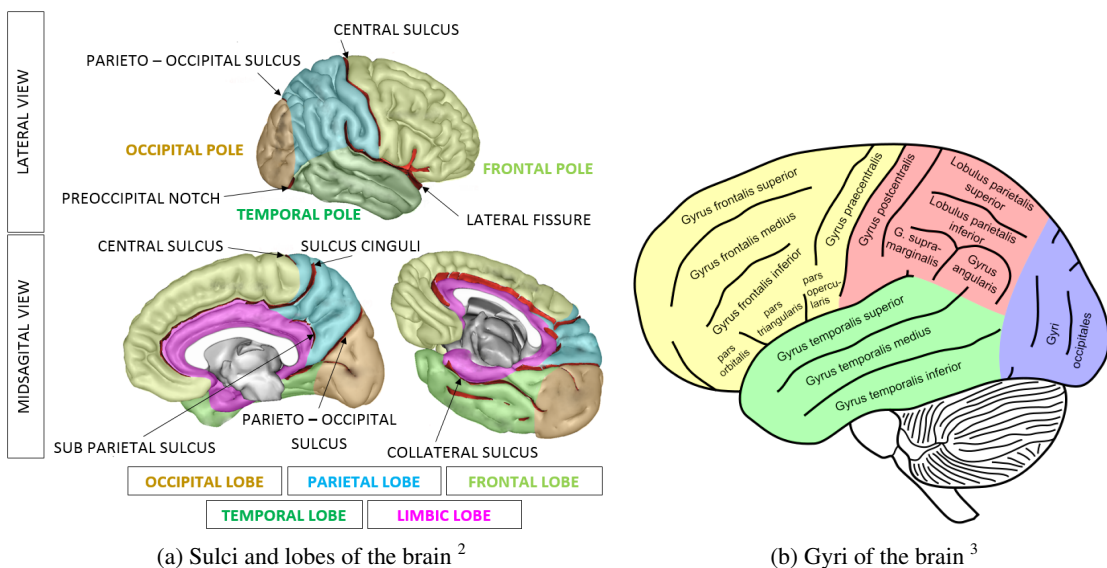


Figure 1.3: Illustration of the organisation of the cortical surface and brain.

[47]: Total and regional brain volume, cortical surface measures (surface area, gyration index, surface curvature, surface thickness) and growth rate. In state-of-the art approaches the following quantities for describing the healthy fetal brain development are reported: According

²Image taken from <https://upload.wikimedia.org/wikipedia/commons/3/3d/LobesCapts.png>; [accessed 13-September-2015]

³Image taken from https://commons.wikimedia.org/wiki/File:Gehirn,_lateral_-_Hauptgyri_beschriftet.svg; [accessed 13-September-2015]

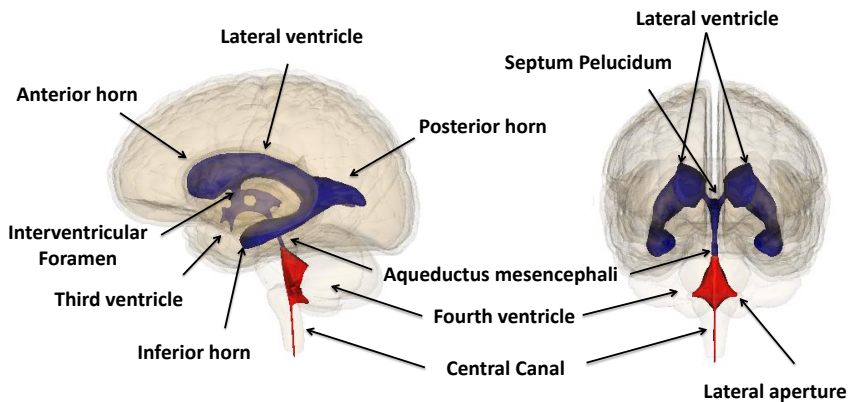


Figure 1.4: Illustration of the ventricle system.⁴

to Roelfsema et al. [59]: the "*Median brain volume increases from 34 cm³ at 18 weeks to 316 cm³ at 34 weeks*". Clouchoux et al. observes in [20] an average cortical plate area between 125 cm² and 420 cm² from GW 25 to GW 35. In [19] they examine the cortical folding progress by estimating cortical plate volume (25 cm³ - 100 cm³), the WM volume (50 cm³ - 170 cm³), the sub-cortical GM volume (4 cm³ - 16 cm³) and surface area (70 cm² - 200 cm²) between GW 25 and GW 36. Gholipour et al. [30] investigate the ventricular development from GW 19 to GW 28 which shows a volume expansion from 3.5 cm³ to 6 cm³.

1.2 Motivation and Problem Statement

The human brain undergoes structural changes in size and in morphology between the second and the third trimester of pregnancy, according to accelerated growth and the progress of cortical folding [64]. The most accurate non-invasive method for observing these events is the fast MR imaging technique, a method first proposed in 1983 [70]. Imaging of a fetus in utero is challenging because of its constantly changing position, which causes image unsharpness and artefacts. Thus, standard MRI was extended to fast MRI for fetal imaging by shortening the image acquisition time to 20 seconds and developing motion correction techniques [9]. A problem of MR imaging is the lack of comparability and constancy of gray-values. In contrast to computer tomography images, where gray-values are mapped to a tissue type based on X-ray absorption characteristics of a specific tissue [11], the gray-values of MR images are mapped according to the proton (hydrogen) concentration. This concentration varies among patients and results in varying gray-values for varying proton density [13, 37]. Thus, for the comparison of brains of adult patients, an atlas as a standard space is required, which avoids the gray-value discrepancies. The brains are mapped to a standardized coordinate system according to marked anatomical lo-

⁴Image modified from https://commons.wikimedia.org/wiki/Category:Fourth_ventricle#/media/File:Fourth_ventricle.png; [accessed 13-September-2015]

cations. However, the fetal brain is a developing structure. In comparison to building an atlas of an adult brain, the fast change of a fetal brain in shape and size has to be taken into account like the cortical folding process and rapid growth of the brain [42]. Also, fetal brains at a certain GW show differences in shape and size. Possible reasons are the inaccuracy in determination of the gestational age, inter-patient variability or pathological growth processes [53, 63]. The motivation for building a fetal atlas is the possibility to compare fetal brains for studying brain development, fetal pathology locations, fetal abnormalities or anatomy.

1.3 Aim of the Work

The aims of this master's thesis are the building of a longitudinal model of fetal brain development on the one hand and an automated labeling procedure for fetal brains on the other. Together, they form an atlas of the developing fetal brain.

Continuous, Quantifiable Model of Brain Development

Within the scope of this master's thesis, an atlas is built to encode all stages of brain development during the fetal stadium in pregnancy. Therefore, both inter-patient variability of brain shapes at a certain GW and the variability in the course of the brain's development in a certain time period are taken into account.

Automated Labeling Procedure

The longitudinal atlas is built based on gray-value information of the fast MR images as well as deduced segmentation of brain structures. The annotation of medical images is time consuming and requires expert knowledge, which leads to high costs [5]. The motivation to consider manual segmentations for building the atlas is the possibility to predict a segmentation model for a new unsegmented MR image. Such a segmentation is derived automatically by registering the model predicted by the atlas to the data.

1.4 Methodical Approach

The methodical procedure for this master's thesis is divided into four main steps: The first step comprises a literature research (cf. Chapter 2, 3 and 4), to identify the methodologies and the results of existing approaches. As second step the behaviour of a state-of-the-art diffeomorphic registration algorithm and a geodesic image regression algorithm (cf. Chapter 5 and 6) is analysed, to understand how these algorithms have to be parametrised for learning a fetal brain atlas. In a third step a tissue labeling framework is created: Geodesic image regression is used to build a longitudinal atlas for fetal brains and geodesic shooting to register new data to the reference space learned. The atlas-based brain annotations serve as cost terms in a graph-cut based segmentation procedure. The last step of this thesis focuses on the evaluation of the framework developed (cf. Chapter 7). For this a dataset of fetal brains containing gray-value MR images

and corresponding annotations is used. Leave-one-out cross validation is applied to create training and test datasets. The accuracy of the estimated and refined annotations for a new patient is computed using a DC [22] similarity measure between the atlas based segmentations and the test dataset as well as the graph cut based segmentations and the test dataset. For assessing the fetal brain development over the gestational age the following parameters are computed: volume of the cortical brain structure, volume of the ventricles and the area of the brain surface. This work concludes with a comparison of the results of this master's thesis to data of medical statistics for verification.

1.5 Related Works

In this master's thesis geodesic image regression (cf. Chapter 3) is used to learn a longitudinal atlas of the fetal brain. Current approaches concerning geodesic regression are found in [1], [54] and [38]. The latest approaches on geodesic shooting are shown by **Ashburner et al.** [2] and **Vialard et al.** [78]. Related works have not considered yet to use geodesic image regression for building a spatio-temporal model of fetal brain growth. State-of-the-art approaches combine registration methods and interpolation techniques to obtain continuity in time (cf. Chapter 2): **Kuklisova-Murgasova et al.** [42] propose a spatio-temporal probabilistic fetal brain atlas. They use a pairwise affine registration approach in image space and a kernel-regression based approach in time to construct the atlas for an age range between 28.6 and 47.7 GWs. The calculation of age-dependent probability maps is proposed for intensity and atlas-based segmentation of brain structures. **Serag et al.** [65] extend the approach proposed in [42], by using non-rigid pairwise registration in space and an adaptive kernel-regression approach in time to build a fetal brain atlas for the age range of 26.7 to 44.3 GWs. **Habas et al.** [33] construct a time-varying fetal brain atlas with application on segmentation. The gestational age ranges from 20.57 to 24.71 GWs. In image space they use groupwise elastic registration of manual segmentations to build tissue probability maps. Voxelwise non-linear modelling is applied to create age-specific MRI templates. To model continuity in time, polynomial fitting is applied. **Risser et al.** [58] use Kärcher means and Large Deformation Diffeomorphic Metric Mapping (LDDMM) for the creation of a diffeomorphic spatio-temporal fetal brain model. Instead of calculating the weighted average of the longitudinal dataset in the image space, the image averaging is computed on the tangent space of the evolution with respect to the chosen Riemannian metric. **Zhan et al.** [84] use the groupwise diffeomorphic registration approach of the Advanced Normalization Tools (ANTs) to construct a fetal brain atlas. 7.0 Tesla MRI images of postmortem fetuses in the early second trimester (15.0 to 22.0 GW) are acquired. The consequently higher tissue contrast enables the development study of additional identifiable brain structures. However, atlases are not only used as a reference space, but also as an improvement of atlas-based automatic segmentation, which is demonstrated in the approaches of **Serag et al.** [67] and **Habas et al.** [34] (cf. Chapter 4). Another main part of this master's thesis covers the refinement of automated segmentation estimations of the atlas using a graph cut based approach for multi label segmentation proposed by **Yuan et al.** [83]. The analysis of state-of-the-art (cf. Chapter 2) approaches shows that both diffeomorphic atlases and atlases for automated segmentations have been proposed, however, the combination of graph cut segmentation and geodesic regression methods

for building an atlas for fetal brains has not been considered yet.

1.6 Results

In the course of this thesis a tissue labeling framework is created for the automatic annotation of cortical and ventricle structures in the fetal brain from GW 18 to GW 30. Geodesic image regression is used in a novel formulation for fetal brains. The results of the analysis of the fetal brain atlas learning procedure lead to the identification of three different age ranges (GW20 - GW 22 day 6, GW22 day 6 - GW 25 day 5, GW 25 day 5 - GW 30 day 2), to compute three separate atlases parametrised according to the fetal brain developmental stage. The proposed tissue labeling framework uses the learned spatio-temporal atlas as cost term in a graph cut based annotation procedure to automatically segment cortical and ventricle brain tissue. The automatic tissue labeling framework estimates cortical segmentations with a DC up to 0.85 and ventricle segmentations with a DC up to 0.60.

1.7 Structure of the Thesis

This master's thesis starts with an introduction, where an overview of this work is given. Chapter 2 describes how atlases are created and applied in the medical field. Examples for fetal as well as adult atlases are given and state-of-the-art methods are summarized. The approaches that are used in this master's thesis for building an atlas are discussed in Chapter 3. Chapter 4 gives an overview of multi-label graph cuts, describes how segmentations of a fetal brain are estimated and contains a description how the automated labeling procedure is designed. Chapter 5 summarizes the preliminary experiments and documents the analysis of a pairwise diffeomorphic algorithm and its registration behaviour regarding the modelling of fetal brain development. In Chapter 6 the created automatic tissue labeling framework is introduced and the analysis of the state-of-the-art algorithms used is documented. Chapter 7 illustrates the evaluation of this work and its experimental setup and concludes with the evaluation results as well as their critical discussion and possible directions for future research.

CHAPTER 2

State-of-the-art

In this Chapter an overview of state-of-the-art approaches of fetal brain atlases is given. Section 2.1 describes the rationale behind brain mapping and explains why atlases are important in that field. Additionally an introduction to fetal brain imaging, the challenges and methods used in that field is given. Section 2.2 analyses differences between adult and fetal brain atlases and state-of-the-art approaches for fetal brain atlas construction are introduced. The presented works are discussed and compared in Section 2.3 with respect to the following criteria: the way how fetal brain atlases are constructed, the datasets used (number of images, image acquisition, preprocessing), advantages, disadvantages and limitations and which brain structures are considered for segmentation and development studies. In Section 2.4 an overview of state-of-the-art approaches for longitudinal atlas construction concerning pathology progression and growing procedures is given. A discussion of the relation of the introduced approaches to this master's thesis concludes the chapter in Section 2.5.

2.1 Concept of Atlases

The aim of brain mapping is to create maps (models), based on investigations, to understand structural and functional brain organization. To this aim, neuroimaging methods as well as knowledge of neuroanatomy and physiology are combined. Due to the fundamental changes occurring in the human brain during pregnancy, a single map is not sufficient to model brain development [75]. Changes in size, according to accelerated growth, changes in morphology, due to the progress of cortical folding and deceleration of the proliferation of ventricular progenitor cells [64] occur. Thus, a collection of brain maps is needed to describe these alterations as a function of time. For studying the brain organisation during its development, abnormalities and locations of pathologies, brain maps are used as a reference model [73]. Newly acquired brain images are labelled to identify structures and possible abnormal changes or to find indicators for diseases. This labeling can be performed manually by annotating the images. This needs an expert and time, which consequently leads to increasing costs compared to an automatic labeling procedure [5]. In this case, labels for non annotated images are estimated automatically

by software using a brain model for the mapping. Such an automated labeling procedure on the one hand and a reference model on the other form an atlas. To cover the time-dependent development of the fetal brain, primarily collections of individual images of different fetuses at different gestational age were used as an atlas [15]. Subsequently, time-varying reference models, which combine interpolation and template building techniques, are considered for building spatio-temporal atlases.

Image acquisition of the fetal brain

Atlases are built based on different properties of medical brain images. The image acquiring modality chosen depends on its ability to illustrate the investigated structure, the efforts of capturing the data and on the patient (fetus, child, adult). The most accurate non-invasive neuroimaging method for observing the second and the third trimester of pregnancy is **fetal MRI** [16]. This method was first proposed in 1983 [70]. MRI images are taken from pregnant women as an alternative to ultrasonography images for prenatal diagnosis. Inadequate ultrasound assessment or upcoming intrinsic ultrasound disadvantages are indications to acquire fetuses with the MRI imaging technique. This technique uses magnetic fields to acquire an image in a non-invasive way. The image acquisition with MRI has no effect on the fetal heart rate, movement or growth and there is no evidence on mutagenic influence [32]. Imaging a fetus is challenging, due to its constantly changing position causing unsharpness and artefacts in images [18]. In Figure 2.1 an example of fetal motion during scan acquisition is illustrated. To

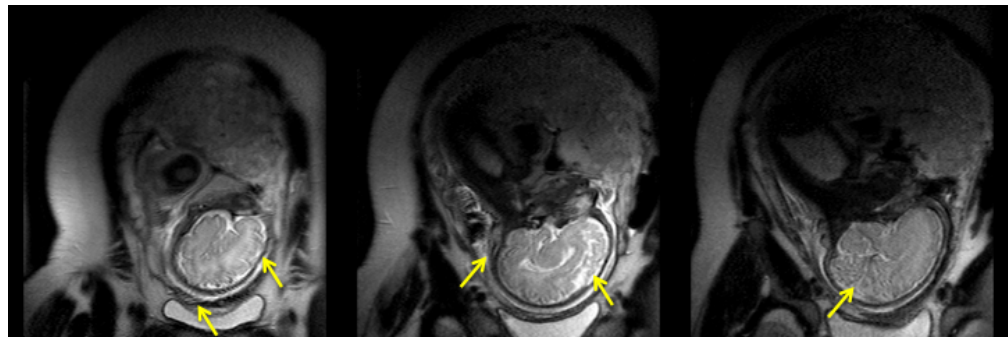


Figure 2.1: Example for image artefacts (yellow arrows) caused by fetal motion during scan acquisition. MR images courtesy of Medical University of Vienna (MUW)

counteract the effects that are caused by fetal movement, fetal MRI was improved through the development of the **fast MRI technique**. Compared to standard MRI, fast MRI has a shorter image acquisition time, that allows to image a fetus in 20 seconds with less motion artefacts [9]. Figure 2.2 shows an example of fast MRI images with an acquisition time about 20 seconds per volume. A disadvantage of MRI is the lack of comparability and constancy of gray-values [37]. In contrast to computer tomography images, where gray-values are mapped to a tissue type based on X-ray absorption characteristics of a specific tissue [11], the gray-values of MR images are mapped according to the proton (hydrogen) concentration. This concentration varies among patients and results in varying gray-values for varying proton density [13] [37]. Thus,

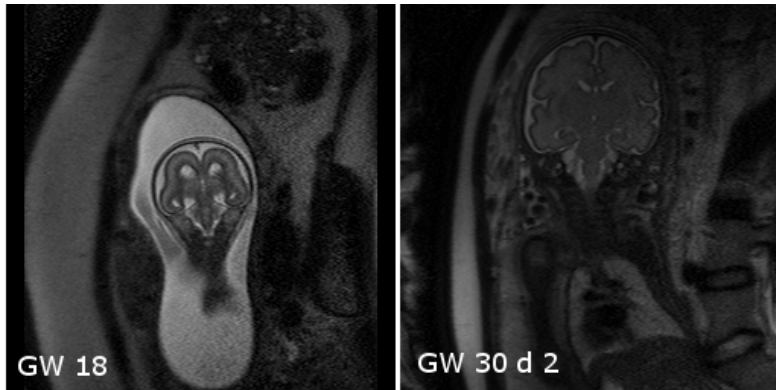


Figure 2.2: Single-shot, FSE T2-weighted MRI slices of fetuses at GW 18 (left) and GW 30 and 2 days (right) (scan time ≤ 20 s). MR images courtesy of Medical University of Vienna (MUW).

for comparison of images an atlas as a standard space is required in which discrepancies in the gray-value distribution are alleviated.

Preprocessing

Depending on the chosen approach to construct a fetal brain atlas, different preprocessing steps are considered to improve the results. To obtain an image acquisition time with 20 seconds image slices have a thickness of about 4 mm. In order to compute a high resolution volume **volumetric fetal brain MRI reconstruction** is used. The series of sagittal, axial and coronal planes of a subject are merged in a preprocessing step to achieve an isotropic three-dimensional image. State-of-the-art approaches are found in [41], [43] and [60]. Due to the fetus' varying position, a main preprocessing issue lies in the **correction of motion artefacts**. Since image acquisition of a fetus also implies the acquisition of the surrounding mother-tissue, all introduced approaches consider **masking** to exclude regions of less interest. Approaches considering **inhomogeneity correction** as a preprocessing step focus on eliminating disturbing influences, which depend on constancy variation of gray-values caused by the MRI technique. The **annotation** of brain tissue or surfaces are also included in preprocessing procedures for building segmentation based models for labelling and developing study purposes.

Atlas Construction

To cover the time-dependent development of a fetal brain, a continuous time-varying template is required to model the structural and shape changes over the gestational age [73]. The corresponding state-of-the-art construction methods combine registration approaches for atlas building and interpolation approaches to obtain continuity over time. Atlas template building approaches are grouped into all-to-one, pairwise and groupwise registration methods [42].

1. **Atlas Template Building:** As found in the literature atlas templates are constructed in different ways and are grouped into the following approaches [42]:

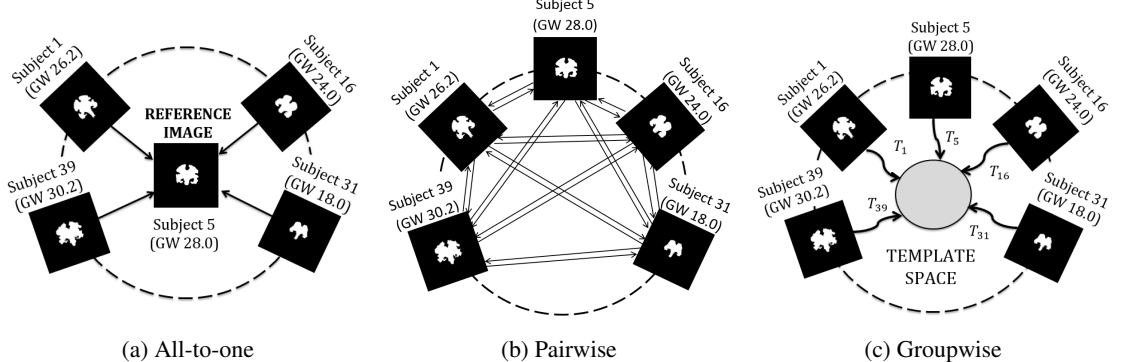


Figure 2.3: Template building procedures

- All-to-one registration: a subject out of the whole population is chosen as reference and all other subjects are registered on to it. This causes bias towards the chosen reference, which does not represent the average geometry of the dataset. An example of such a reference coordinate system was proposed by Talairach and Tournoux [74] for the adult brain. The procedure is illustrated in Figure 2.3a on the left.
- Pairwise registration: All images in the dataset are pairwise registered to a selected reference image (cf. Figure 2.3b in the middle). Subsequently, the resulting (inverse of the) affine or non-rigid transformations, represented by arrows, are averaged, to build an average reference image. An example of pairwise affine registration is proposed in [42] and of pairwise non-rigid registration in [65].
- Groupwise registration: This approach avoids the need for an initial reference space and constructs an unbiased average atlas. For estimating the unknown average template space all images in the dataset are used. During the registration the unknown template is updated to obtain an optimized unbiased reference model (cf. Figure 2.3c on the right). Risser et al. [58] propose an unbiased MRI atlas using a diffeomorphic approach. Habas et al. [33] use elastic groupwise registration to build a probabilistic spatio-temporal atlas of the fetal brain [33]. Zhan et al. [84] also use a groupwise diffeomorphic approach to construct a fetal brain atlas, based on images of post mortem fetuses.

2. Time Continuity and Interpolation: To obtain a continuous spatio-temporal model, the retrieved anatomical templates have to be set into relation dependent on a parameter, that characterizes the gestational age. The following corresponding approaches can be found in the literature: kernel-regression based [42], adaptive kernel-regression based [67], polynomial fitting [33], B-Spline fitting [3], Kärcher means [58].

2.2 Atlases of the Developing Brain

Compared to the adult brain a fetal brain is a developing structure, that changes in shape and size during pregnancy [64]. Also the cortical folding process and rapid growth have to be taken into account in the atlas building process. The longitudinal variability is addressed by building a time-varying (spatio-temporal) atlas, i.e. a brain model is represented as a function of time (gestational age) [42]. Due to inaccuracy in the determination of the gestational age, inter-patient variability or pathological cell proliferation, fetal brains also differ at a certain gestational week [53, 63]. Furthermore, atlases are differentiated between probabilistic (probability maps encode the variability of the population) and deformable atlases (deformation fields encode the variations) [42]. The following fetal brain atlas approaches are found in the literature:

Pairwise Registration Approaches

Kuklisova-Murgasova et al. [42] use a kernel regression based approach in time and a pairwise affine registration method in the image space to build a spatio-temporal probabilistic atlas. The database used contains 142 T2 weighted FSE MRI images of fetuses between GW 28.6 and 47.7. The images are bias corrected and a brain mask is applied. Afterwards the images are aligned to a reference image by using affine registration. The resulting affine transformations are mapped to a time-dependent average space using a Gaussian kernel to create a continuous spatio-temporal model. The computation of the *average age-dependent template anatomy* contains a transformation of all images to an average age dependent reference space and a voxelwise weighted intensity averaging. The *probability maps* are created by transforming all segmentation to an average age dependent reference space and a voxelwise weighted averaging. Kuklisova-Murgasova et al. handle the segmentation of source images using a segmentation methodology that combines intensity-based and atlas-based segmentations.

Serag et al. [65] illustrate a spatio-temporal fetal brain atlas using pairwise registration combined with adaptive (time-varying) kernel regression: 204 T1 and T2 weighted FSE MR images of premature neonates between the post-menstrual age 26.7 to 44.3 weeks are acquired. In a preprocessing step a brain mask is applied to the data to exclude non brain structures and field inhomogeneity is corrected. Adaptive kernel regression is used to generate a spatio-temporal atlas represented as a sequence of volumes at a set of regularly sampled time-points. The kernel width is adapted according to the amount of subjects at a certain time-interval and the change in brain volume over time. In order to estimate an atlas at specific time-points the dataset is divided into time-interval groups. First, a global affine registration derives transformation parameters for global size and shape differences (rotation, scale, shear). The next step is a local non-rigid registration step using free-form deformation. Figure 2.4 illustrates the procedure how the age-dependent average space atlas is built by pairwise registration and transformation averaging. Every image within a time-interval is chosen as target image and registered to the remaining images in the group. For every target the resulting transformations, denoted with $T_{\cdot,\cdot}$, are averaged by adaptive kernel regression. Subsequently, the resulting average transformations \bar{T}_{\cdot} are used to map the reference images to average images \bar{I}_{\cdot} . The mean images of all targets

build a mean atlas. To create a final average atlas for a time-interval group, the images of the mean atlas are also averaged by adaptive kernel regression.

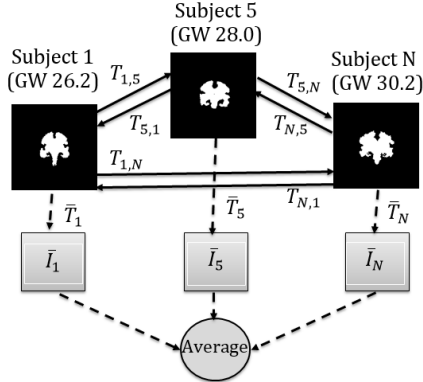


Figure 2.4: Pairwise Fetal Brain Atlas Construction of [65]. Only three images are illustrated here to achieve clearer visualisation of the registration process. Modified from [65].

Groupwise Registration Approaches

Habas et al. [33] create a probabilistic spatio-temporal atlas based on MR intensity, tissue probability and shape changes of the fetal brain, for tissue segmentation. 20 T2 weighted Single Shot Fast Spin-Echo (SSFSE) MR images between GW 20 and 25 are acquired and motion corrected. Five different anatomical structures (marked with a corresponding label) are manually annotated in the images by setting the voxels of a label type to one and the rest to zero to create tissue label maps. Subsequently, the binary images are smoothed to reduce aliasing and error artefacts and to obtain smooth maps. Tissue maps are firstly aligned in the average space of the dataset used by estimating global transformation parameters (rotation, scaling, translation). Subsequently, subject specific displacement fields are estimated to eliminate fine scale differences, like changes in cortical folding. To this aim, a local deformable template-free groupwise registration approach, based on an elastic deformation model, is used. In a gradient descent based procedure, a set of subject-specific displacement fields between subject and the groups' average shape are determined by the minimisation of a linear elastic energy function. The temporal modelling of anatomical deformations, scaling components and MR intensities is performed by using polynomial fitting. Habas et al. [33] use the estimated models for atlas-based tissue segmentation of anatomies of new fetal brain data. The atlas-based segmentations at a gestational age are estimated by discretising the continuous temporal models. The new MR intensity image is first globally registered to the intensity model of the same gestational age and subsequently transformed by multiple elastic deformations. For tissue labelling the age matching tissue probability map is registered onto the subject's space, using the inverse of the previous estimated transformations. The resulting labels define a prior source for spatial variation and are used for atlas-based tissue segmentation of a new subject's anatomy.

Risser et al. [58] use Kärcher means and LDDMM for the creation of a diffeomorphic spatio-temporal fetal brain model. The Kärcher means are intrinsic means on Riemannian manifolds. Instead of calculating the weighted average of the longitudinal dataset in the image space, the average image is computed in the tangent space of the evolution with respect to the chosen Riemannian metric. The dataset used consists of T2 weighted MR images of different neonates acquired between the 29th and 42nd GW. In a preprocessing step corresponding probabilistic segmentations with the same topology are estimated using the approach of [42]. Additionally, the images are masked in order to exclude non-brain tissues, bias field corrected and rigidly aligned. There is no data for every time point available and a subject is represented nearly once in the dataset. For computation, regular sampled time points $t : t_1, \dots, t_N$ are considered, for which weighted averages A_t of the image shapes in the databases are calculated using the Principal Geodesic Analysis (PGA) method. This method obtains efficient description of the anatomical variability of data on the manifold of brain images for every regular sampled time point. For constructing the fetal brain atlas initial guesses of the average shapes are defined and the diffeomorphism ϕ_t , which encodes the entire deformation of the average shapes in time, is calculated. For this, pairwise LDDMM registration of subsequent average shapes ($A_{t_i}, A_{t_{i+1}}$) is performed and the resulting transformations are integrated over time. Subsequently, the average shapes are optimized in the following way using a gradient descent based procedure: An initial momentum $P_0(I_S, A_{t_S})$ is computed for every image I_S in the dataset by registering the time corresponding average shape A_{t_S} onto the image, using LDDMM. An illustration of this approach is shown in Figure 2.5. In a second step the Kärcher mean of the obtained momenta

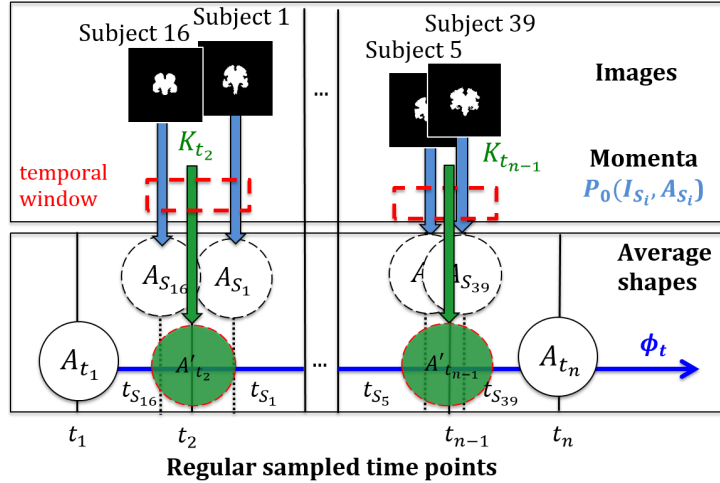


Figure 2.5: Building of a diffeomorphic fetal brain atlas using Kärcher means K . Modified from [58]

is calculated for every regularly sampled time point t . For handling temporal sparsity in the Kärcher mean computation, Gaussian kernels are used as an additional parameter for defining a temporal window. The deformed template images A'_t are computed by transforming the average templates A_t by the estimated average momenta using the shooting equation. The last step of

this procedure contains the update of the template with $A_t = A'_t$ and recomputing of ϕ_t . The procedure is executed until the norm of the gradient of a Kärcher mean representing energy function is below a defined threshold.

Zhan et al. [84] build a spatio-temporal reference model of the early second trimester by using the diffeomorphic approach based Advanced Normalization Tools (ANTS). 34 post-mortem human fetal brain images between the GW 15 and 22 are acquired with a 7.0 Tesla MRI technique. In a preprocessing step inhomogeneity and bias field correction are applied and non-brain tissue is manually removed. The templates are created by first estimating diffeomorphic paths from an initial template guess to the brain images. Subsequently the obtained diffeomorphisms are updated by changing the initial condition of each diffeomorphic path to optimize the template shape. Therefore, symmetric diffeomorphic pairwise registration is used in an optimisation procedure for the new mappings between the template and the images in the dataset. All resulting optimised deformation fields are combined and made into one total deformation field.

2.3 Discussion

The introduced pairwise and groupwise approaches in Section 2.2 are compared and summarized in Table 2.1: The methods are discussed with respect to the imaging technique used where FSE denotes Fast Spin Echo, SSFSE Single Shoot Fast Spin Echo and T the considered relaxation time. Furthermore, the type of template building (Space) and continuity establishing (Time) approaches are identified as well as the number (No.) of considered subjects, their state and the age range of the dataset in gestational weeks (GW). The limits of the approach of

Table 2.1: Comparison of fetal brain atlas construction approaches

Approach	MRI	Space	Time	Age range (GW)	No.	State
Kuklisova-Murgasova 2010	T2, FSE, 3.0 Tesla	pairwise affine	kernel-regression	(29,44)	142	invivo
Serag 2012	T1,T2, FSE, 3.0 Tesla	pairwise non-rigid	adaptive kernel-regression	(26,44)	204	invivo
Habas 2010	T2, SSFSE, 1.5 Tesla	groupwise elastic	polynomial fitting	(20,25)	20	invivo
Risser 2011	T2, FSE, 3.0 Tesla	groupwise diffeomorphic	Kärcher means	(29,37)	50	invivo
Zhan 2013	T2, Micro-MRI, 7.0 Tesla	groupwise diffeomorphic	Deformation field composition	(15,22)	34	post-mortem

Kuklisova-Murgasova et al. [42] lie in the registration of extremes of the gestational age-range (29 GW, 44 GW) with errors between 1.3 and 1.8 gestational weeks. Another limit lies in the sensitivity of the kernel-based regression to the distribution of the data [42]. In comparison to [42], Serag et al. [65] use a non-rigid registration approach in image space, since the affine alignment of images cannot compensate for local inter-subject shape variability, and to overcome the effect of blurred regions in intensity-averaged templates. Because of the folding of the brain surface, cortical regions have a larger local inter-subject variability compared to other brain structures and thus are susceptible to blurring. In the time domain they use an adaptive kernel approach and show clearer level of detail at all ages compared to [42], which results in an improved registration of atlas-based segmentation to new subjects [65]. Compared to groupwise approaches, Kuklisova-Murgasova et al. as well Serag et al. use a more comprehensive dataset: A wider gestational age range of 15 to 18 GWs compared to 5 to 8 GWs, and in average a three time higher amount of images. For more detail cf. Table 2.1. Habas et al. [33] use a smaller dataset of 20 healthy fetuses and a lower gestational age range (20.57 to 24.71 GW) as well. The limitations of atlases constructed by groupwise registration lie in the coverage of relatively narrow age ranges compared to pairwise approaches [65]. Another disadvantage is the lower ability to be comparable in anatomic definition [65]. Risser et al. use a topology preserving approach based on diffeomorphic mapping to build a fetal brain atlas. Instead of averaging in the image space, a Kärcher mean is applied in the tangent space. A further advantage of this approach is the temporal consistency, which is achieved by estimating missing data in a growth-trajectory. Zhan et al. [84] present the only approach that uses 7.0 Tesla MRI, because only post-mortem fetuses in the early second trimester of pregnancy are observed in the dataset. The imaging technique used proposes higher tissue contrast compared to the other approaches and so Zhan et al. are able to model additional structures like the main subcortex structures and also the laminar organization of the cerebral wall. In comparison to the other approaches, a spatio-temporal atlas of fetal brain surfaces was generated instead of volumes. The aim of this approach is to study global growth trajectories and temporal changes of lateral ventricles, nuclear structures and the Sylvian fissure [84].

Discussion Preprocessing

Habas et al. [33] only documented the use of a **motion correction** technique using Slice Intersection Motion Correction (SIMC) [41]. Since Zhan et al. [84] only acquired post-mortem images of fetuses no motion correction is needed. Kuklisova-Murgasova et al. [42] use non-rigid registration to propagate the brainmask from a reference subject to the other images in the dataset for brain **masking**. Additional brainmasks are created to enable consistent registrations of the brain boundary. For this, morphological operations are applied onto intensity based annotations of brain tissue and show higher accuracy than the first created masks. Serag et al. [65] used the Brain Extraction Tool (BET) [71] to mask non-brain tissues in the images of fetuses. Zhan et al. first tried to automatically mask the fetal brain volumes using a Skull Stripping Meta-Algorithm (SSMA) [45]. Since they were not successful they manually strip the skull using the Brain Suite software and a protocol for extra cerebral tissue exclusion [84]. Kuklisova-Murgasova et al. [42], Zhan et al. [84] as well as Risser et al. [58] perform **bias correction** with the N3 method [69]. Serag et al. [65] use the updated version of the N3 approach

- the **N4** algorithm to correct inhomogeneity [77]. **Alignment and rescaling** approaches are considered as preprocessing step to reduce registration error in the atlas building procedure: Kuklisova-Murgasova et al. manually align the acquired images with the MNI atlas [28] by using affine transformations. Serag et al. [65] use global transformations (shape differences, size), obtained from affine registration, to align the data. Risser et al. [58] align the data in a rigid way. Zhan et al. [84] prefer to align the data using a volume preserving rigid transformation to perform normalisation in space. Atlases are constructed based on MR images, but also on **annotations of brain-structures or surfaces**. The latter models are used for labelling and developing study purposes. Kuklisova-Murgasova et al. [42] use a fully automatic segmentation procedure, combining an intensity-based as well as an atlas-based segmentation approach, to segment different brain structures. Risser et al. use the atlas-based segmentation approach of Kuklisova-Murgasova et al. [42] to obtain annotations of the fetal brains. Zhan et al. identify surfaces by using the surface extraction tool of the BrainSuite Software.

Discussion Brain Structures

The standard MR imaging technique for invivo fetuses is to use 1.5 to 3.0 Tesla scanners to acquire T1 and T2 weighted data. Distinguishable structures in this case are illustrated in Figure 2.6: Grey Matter (GM), White Matter (WM), the VENTricles (VENT) and the Germinal MATrix (GMAT) [84]. Also extraventricular Cerebro Spinal Fluid (CSF), Deep Grey Matter (DGM) and Non-Brain structures (NB), like skull or amniotic fluid are identifiable. Using a MR scanner

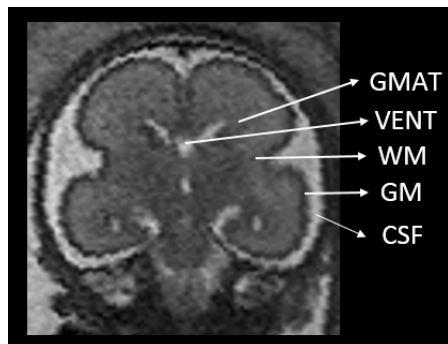


Figure 2.6: Illustration of identifiable brain structures in a T2 weighted fast MRI acquired with a 1.5 Tesla scanner (Germinal MATrix (GMAT), VENTricles (VENT), White Matter (WM), Grey Matter (GM) and Cerebro Spinal Fluid (CSF)). MR image courtesy of Medical University of Vienna (MUW).

with 7.0 Tesla, additional brain structures are recognized due to higher tissue contrast: Main subcortex structures as well as the laminar organization of the cerebral wall (Ventricular Zone (VZ), Intermediate Zone (IZ), SubPlate zone (SP), Cortical Plate (CP)) [84]. In Table 2.2 a summary of the modelled brain structures of every approach is given.

Table 2.2: Comparison of modelled fetal brain structures

Approach	brain annotations
Kuklisova-Murgasova 2011 [42]	Cortex (cortical GM), WM, DGM, CSF, Background, brainstemm, cerebellum
Serag 2011 [65]	No annotation based templates are created
Habas 2010 [33]	Cortex, WM+GMAT, VENT+CSF+NB
Risser 2011 [58]	Cortex
Zhan 2013 [84]	VZ, IZ, SP, CP, lateral VENT

2.4 Spatio-temporal Atlas Construction

Spatio-temporal atlas construction differs between subject-specific and time-specific approaches. **Subject-specific** modelling aims to average individual trajectories for obtaining a typical growth scenario. In this case the inter-subject variability is assumed to be constant over time [25] (cf. Figure 2.7a) and provides a template at each age [25]. **Time-specific** modelling makes it possible to describe the inter-subject variability over time by a mean scenario of evolution (cf. Figure 2.7b) and provides a template at each age [25]. In the field of longitudinal regis-

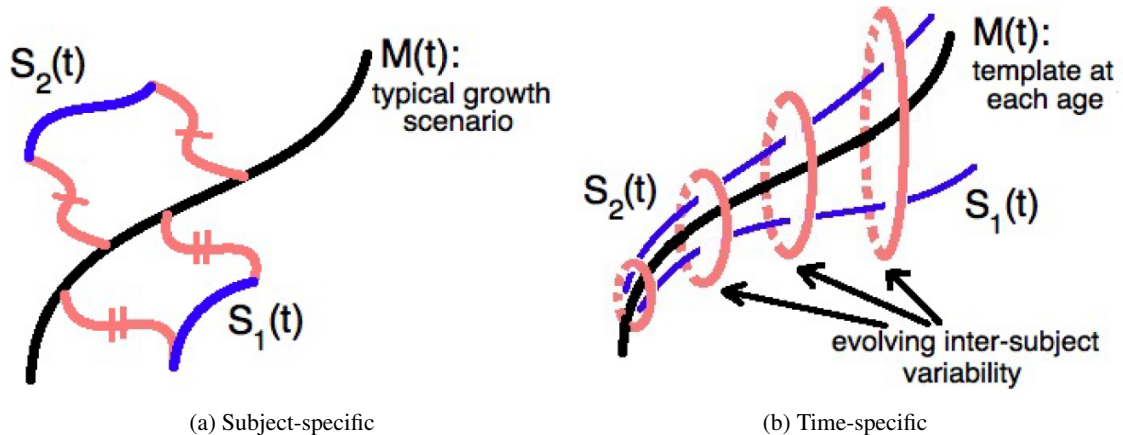


Figure 2.7: On the left side the subject-specific modelling is visualised: The individual trajectories are denoted by $S_i(t)$ and their averages are used to obtain a typical growth scenario $M(t)$. Time-specific modelling is illustrated on the right side. It shows the estimation of a mean scenario $M(t)$ of evolution to describe the inter-subject variability over time. Image courtesy of Stanley Durrleman [25].

tion, data types are divided into three main groups [25]: **Cross-sectional data** consists of a set of comparable or homologous samples with no effect of time or age on the data. **Time-series data** is labeled by an age dependent temporal marker, which indicates a developmental stage, progression of pathology or growing. It is not necessarily assumed that the data represents the same subject at different time-points. **Longitudinal data** contains more than one observation of

a subject by acquiring data over a time period at different time-points.

Image Regression

Image regression works with time-series data and builds a continuous model of development. With this approach it is possible to measure shape changes between discrete observations in time [25].

An example of an approach which uses geodesic regression as base for atlas construction is found in **Niethammer et al.** [54]. They use five MR images of adults with dementia at different ages to model dementia depending ventricle changes over time. **Hong et al.** [38] use metamorphic geodesic regression to compute a mean scenario from a time-series brain dataset of nine macaque monkeys of age 3, 6 and 12 months (27 images). It is based on a LDDMM formulation and estimates a regression function of geodesics using geodesic equations for metamorphosis. **Fishbaugh et al.** [29] use a geodesic image regression formulation with reduced model parametrisation. Three T1 weighted brain images of one child at age 6, 12 and 24 months are used to assess pediatric brain development. **Singh et al.** [68] use geodesic image regression to construct an atlas of MRI brain images from the Alzheimer's Disease Neuroimaging Initiative (ADNI) database at age 70.75, 71.38, 71.78 and 72.79 and show the expansion of the lateral ventricles over time. Additionally, the calculated atlas is used to predict future brain changes and atrophic behaviour of patients with Alzheimer's disease using EPDiff equations.

Longitudinal Analysis

Longitudinal analysis only uses longitudinal data, where images of a subject are acquired more than once. This method first determines individual trajectories of a subject and subsequently measures the differences and similarities between them [25].

Serag et al. [66] perform longitudinal registration via atlas propagation. They use freely available spatio-temporal atlases to cover the missing anatomical information between two observations of a fetus over a time-interval of 10.33 GW. Images of 50 fetuses are acquired and used for evaluation. The calculation of the subject-specific trajectory involves only two images of a subject (template and target), acquired at different time points. Instead of estimating the direct transformation from template to target, the images are registered to the corresponding atlas templates to obtain a mean deformation field. Subsequently this field is used as initialisation for the direct registration of template and target. **Durrleman et al.** [25] propose a framework for statistical analysis of longitudinal shape data. In a first step continuous subject-specific growth trajectories are modelled. Subsequently the resulting temporal shape changes across subjects are compared, by estimating a mean growth scenario (atlas) using intrinsic statistics in the space of spatio-temporal deformations. The framework evaluation includes the measurement of the developmental delay of deep brain structures using a longitudinal brain dataset of children between age three and five years with autism. **Liao et al.** [48] propose a longitudinal atlas construction framework, that considers as well subject-specific as global population information. The ADNI and Baltimore Longitudinal Study of Aging (BLSA) databases are used in this approach, containing brain images of elderly subjects. A feature based 4D HAMMER image registration method is used to estimate the subject specific growth models. Subsequently, the obtained lon-

itudinal information of each subject is used to propagate it to each time point in the subject space. Information of global population is captured by constructing an unbiased template using groupwise registration among all the subject sequences. To map from the subjects space to the atlas space only one transformation is needed. A kernel regression process is applied on the whole set of warped images from different subjects to achieve temporal consistency in the atlas space.

Discussion

As found in literature ([3, 25, 29, 38, 54]), image regression for time-series data has been evaluated only using adult- and child-brain datasets, which record changes of brain structure over time. The fetal brain shows a variability in time as well and thus is qualified to be used for image regression to build a spatio-temporal atlas. Time-specific approaches concentrate on statistical correlations of the observed dataset over time and are used to encode the inter-subject variabilities of fetuses in a single deformation for every subject. The building of this mean scenario forms a base for constructing a continuous fetal brain atlas by modelling the brain development of every fetus in the time-series dataset with a single diffeomorphic deformation. Using a longitudinal dataset of fetal brains, subject-specific methods are applicable for studying fetal brain development. Subject-specific approaches are used to compare the brain growth patterns of two different subjects. The main focus lies here in estimating the variation of individual growth trajectories to identify development delays at any time-point. Subject-specific approaches use temporal re-aligning to bring different subjects into correspondence. Serag et al. [66] use only two images per subject and freely available fetal brain atlases for estimating a subject-specific trajectory. They perform atlas-based initialisation for local non-rigid longitudinal registration, because without this initialisation, poor registration results are achieved [66]. The challenges of longitudinal registration lie in capturing the fine local anatomical variations between scans, which have been acquired over a large period of time (in average 10.33 GWs) [66]. In contrast to this, the question arises if it is possible to represent a growing pattern of a subject only using two images and atlas based initialisation, since the atlases used encode mean shape information and do not represent the subject specific characteristics. Replacing the initialisation procedure by using more than two images per subject is difficult to perform, since obtaining more than one image of the same subject without medical indication, is not performable due to the stressful and costly image acquisition procedure for pregnant women [44].

2.5 Relation to this Thesis

This thesis unites advantages of the discussed registration approaches. The fast MRI technique is identified as a **suitable imaging technique** for in-vivo fetuses, since it is a non-invasive technology, which has no mutagenic influence on the fetus and its brain development. Additionally, motion artefacts are reduced by faster image acquisition time up to 20 seconds compared to standard MRI scanning [9]. Since the lack of comparability and constancy of gray-values in MRI, an atlas is used as reference model to make fetal brains comparable in development studies. Depending on the approach chosen to construct a fetal brain atlas, different **preprocessing** steps

like alignment, masking and inhomogeneity correction are performed to improve the results. The human fetus has a varying orientation and motion according to its Gestational Age (GA) [12]. Thus, there is a need of an rigid-aligning preprocessing step, to avoid and reduce orientation related registration errors. Also masking of the fetal brain is considered, since the acquired data contains the surrounding mother tissue, which causes distorted registration results for fetal tissues. The examination of atlas building methods show that every approach introduced uses global alignment and non-brain tissue masking of the fetal brain images as preprocessing step to improve the registration result. Thus, brain masking and alignment by rigid registration (rotation, translation) are considered as necessary preprocessing steps in this thesis to normalize the fetal brain images in space. In this thesis an **image dataset** of 46 healthy fetal brains is used. It contains 1.5 Tesla MR images of different subjects. One subject is represented only once. The age is measured in gestational days. There does not exist a dataset for every gestational day. For more than one gestational time point, more than two images of different subjects are available. The observed age range reaches from 129 to 212 gestational days. All the brains are annotated manually by an expert. According to these facts, the following assumptions are made:

The use of an "all-to-one" approach for constructing the fetal brain atlas is discarded for this thesis, because choosing a single subject as reference introduces substantial bias. The brain structures of fetuses cannot be described by one image, since it does not reflect occurring changes over time [65] [42]. Exclusive pairwise affine registration for image alignment results in blurred regions in the templates obtained by intensity averaging. Affine registration is not capable of compensating local inter-subject variability. This leads to worse registration results between atlas-based segmentations and individual objects compared to non-rigid approaches, which show a higher level of detail [65]. An advantage of pairwise approaches lies in the registration of wider age-ranges between 15 to 18 GWs, compared to groupwise approaches, which are able to cover only small age ranges between 5 to 8 GWs. An advantage of groupwise registration approaches is the template-free estimation of the initial reference space. The template is estimated and updated during the registration procedure [42]. Compared to other approaches, the main limitations of groupwise registration lie in the lower level of anatomic definition [65]. For the fetal brain tissue labelling framework constructed in this thesis a **non-rigid longitudinal** registration approach is considered, because as found in the literature [3, 25, 29, 38, 54], image regression for time-series data have been evaluated only using adult- and child-brain datasets, that record changes of brain structure over time. The fetal brain shows a variability in time as well and thus, is qualified to be used for image regression to build a spatio-temporal atlas. In this thesis a time-series dataset of fetuses is used. In this case subject-specific approaches are not taken into account, since there is only a single image per subject available in the dataset. Instead, a **time-specific approach** is considered, which concentrates on statistical correlations of the observed dataset over time and is used to encode the inter-subject variabilities of fetuses in a single deformation for every subject. Image regression is used to model a mean scenario as base for constructing a continuous fetal brain atlas. A single diffeomorphic deformation models the brain development of every fetus in the time-series dataset. Thus, instead of calculating discrete age-dependent templates combined with interpolation, in this thesis the local inter-subject variability is considered to be modelled continuously in time and non-rigidly in space, by geodesic regression (cf. Section 3.5). For modelling the time dependence of structural changes, inter-

pulation or averaging approaches were examined. The application of Kärcher mean in the tangent space achieved a higher temporal consistency compared to image averaging in the image space, because of the capability to estimate missing data in a growth trajectory. The comparison of non-rigid registration approaches show that **diffeomorphic registration** preserves topology. This approach constrains deformation fields to be diffeomorphic, in other words to be smooth and invertible. Therefore, it is guaranteed that every image entity (pixel or voxel) in the template corresponds to another one in the target. Thus, it is considered to use diffeomorphic based registration in this thesis, because it ensures anatomically valid templates, which is important in the medical field. The quality of **alignment of the atlas with a new subject** is proportional to the quality of segmentation. Affine registration is used to register the atlas to a new subject's anatomy, which is not significantly different from the average of the population. Therefore, it shows higher robustness towards alignment error than non-rigid approaches. In case of changing structures non-rigid registration shows increasing segmentation accuracy compared to affine registration [42]. In this master's thesis a non-rigid approach (geodesic shooting, cf. Section 3.4) is used to register the resulting segmentations to a new fetal brain image. For achieving a higher level of detail of the atlas-based segmentations, a graph cut based approach (cf. Chapter 4) is used to refine them. Since the dataset used is illustrating invivo fetuses acquired with a 1.5 Tesla MRI scanner the additional **brain structures** (main subcortex structures, laminar organization of cerebral wall) modelled by the approach of Zhan et al. [84] cannot be considered, since they are not distinguishable in the images, due to lower imaging contrast of 1.5 Tesla scanner compared to 7.0 Tesla scanner. Since only images acquired with a 1.5 Tesla scanner are used in this thesis, the main focus lies on modelling differentiable structures of vivo fetuses, e.g. ventricles and developing cortical matter.

2.6 Summary

In this chapter the concept of atlas construction and its motivation are explained. Differences between adult and fetal brain atlases are presented and challenges regarding the image acquisition, preprocessing and construction are enumerated. The introduced state-of-the-art approaches ([65], [42], [33], [84], [58]) for fetal brain atlas construction combine template building techniques (all-to-one, pairwise, groupwise) and interpolation techniques (kernel-regression, polynomial fitting, B-Spline fitting, Kärcher means). These approaches are discussed with respect to the preprocessing and acquisition setup used, brain structures modelled, age range, number of subject and state (invivo, post-mortem). Additionally, an overview of spatio-temporal atlas construction techniques (image regression, longitudinal analysis) is given and corresponding state-of-the-art approaches are introduced and discussed. This chapter concludes with the relation to this thesis and discusses the approaches chosen to build.

CHAPTER 3

Image Registration and Diffeomorphisms

This chapter gives an overview of basic registration concepts and explains how registration of two images or a collection of images works. Subsequently, it is addressed how atlases are learned by using geodesic regression and an explanation of the underlying methods is given. In Section 3.2 an overview of image registration methods is given and the functionality of general optimization frameworks is illustrated. Section 3.3 gives an overview of LDDMM, illustrates the optimisation problem and introduces the tuning parameters. In Section 3.4 the differences between geodesic shooting and LDDMM are shown and Section 3.5 explains how geodesic regression works. The 2D analysis of a state-of-the-art LDDMM algorithm is documented in Chapter 5. The 2D analysis of a state-of-the-art geodesic regression algorithm is demonstrated in Chapter 6.

3.1 Denotation

In this thesis images are denoted with I , a source image with I_0 , a target image with I_1 , and image features or intensities with x, y . Images are defined on a image domain Ω . Transformation functions from a source to a target are expressed using ϕ . A diffeomorphic transformation φ is also denoted as ϕ if it is expressed as a curve. The denotation $v_t()$ represents the flow of a time t dependent vector field which lies in the space of smooth velocity vector fields denoted with V . L expresses a differential operator and L^2 the standard L^2 norm for square integrable functions. u_0 names the initial momentum, v_0 the initial vector field and Id the identity. The capital K is used to describe the pseudo inverse Green's function, D acts as representative of the Jacobian operator and ∇ denotes the gradient.

3.2 Overview of Image Registration Methods

Subjects differ in anatomical definition, change over time due to diseases, growing or surgery and move during image acquisition (breathing, body movement). This is the motivation for using so-called registration methods which establish spatial correspondence between images in order to be able to perform the following tasks in the medical field [72]:

- Performing longitudinal studies using images before and after a treatment
- Atlas-based automatic labelling
- Positioning of a patient in an image and alignment to temporal series
- Alignment and comparison of images of different modalities (multi-modal registration)

Image registration is used to find an optimal spatial transformation or a correspondence among two images (a source (template) image I_0 and a target image I_1) of the same (mono-modal) or different (multi-modal) imaging modality. In the mono-modal case we can differentiate between feature-based and intensity-based methods. **Feature-based** registration approaches first calculate image features based on local information of the images, and then establish correspondence between these image attributes [51] [62]. **Intensity-based** methods consider the whole gray-value information of the source and target image to match them [72]. The construction of a mapping function for transforming a template image as close as possible to the target image requires analysis of the geometric deformation of the observed objects. The mapped structures are analysed according to the possible positions in image space, expecting rotation angle, translation distance, ability to be illustrated in a sheared or warped way, to be displayed entirely or partially, scaled or not scaled. The choice of a suitable mapping function incorporates the needed accuracy of the mapping and the image acquisition setup, due to possible occurring distortions and errors. **Parametric** and **non parametric** mapping approaches exist. Parametric methods estimate the geometric deformation by searching the optimal parameters of a function [85]. Additionally, registration approaches differentiate between **linear** registration, which **globally** affects the image, or **deformable** registration, which **locally** deforms image patches.

Linear Registration

Linear registration are categorised using the following transformation types:

- **Rigid** transformation: This registration approach contains only translation and rotation transformations of images [51] and preserves angles and distances.
- **Affine** transformation: Preserves parallel lines by mapping them on their identity [51]. It allows only to correct global differences in size and shape of an object (e.g. mapping a parallelogram onto a square). In case of an atlas, local and spatial variability of its underlying population is obtained [42] [85].
- **Perspective-projective** transformation preserves straight lines (e. g. mapping a general quadrangle onto a square) [85].

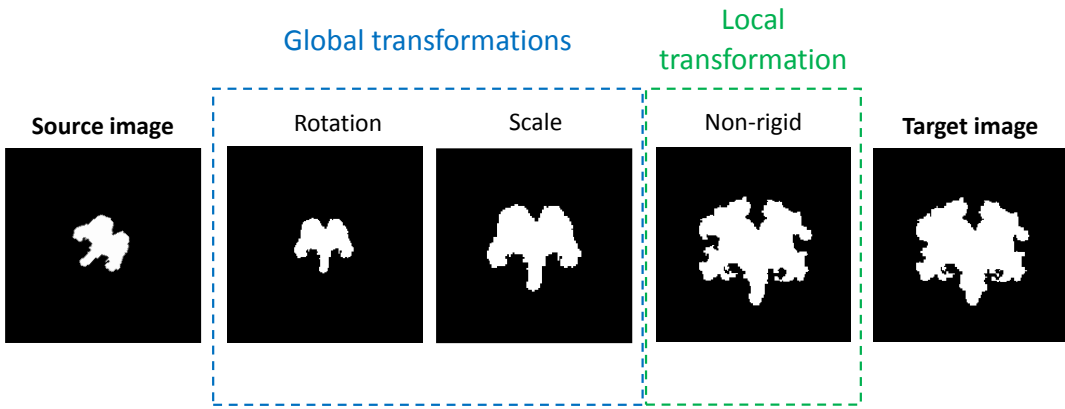


Figure 3.1: Illustration of affine and non-rigid registration. Template and target image show differences in size, orientation and also internal structures. The use of affine registration as global image transformation achieves correspondences according to the scaling and alignment of the source- and target picture. Correspondence of internal structures is achieved by local non-rigid registration.

Deformable Registration

In contrast to linear registration, deformable (non-rigid) registration additionally allows local stretching operations in order to achieve correspondence between two images [21] and is based on a **deformation model**. Figure 3.1 illustrates schematically the mechanics of rigid and non-rigid transformations and their global and local effect on a source image. Deformation models are divided into three groups [72]:

1. Physical models

- **Elastic model:** This approach uses the concept of external (stretching) and internal (stiffness, smoothness) forces instead of parametric mapping functions to formulate a model of complex distortions. The aim is to find the optimal matching by a minimal amount of bending and stretching of the template image. In contrast to parametric mapping, correspondence detection and definition of a transformation function is carried out simultaneously [85].
- **Fluid model:** This approach represents the deformation based on the Navier-Stokes equation, which models the behaviour of the flow of viscous fluids [72].
- **Diffeomorphic model:** This transformation type restricts registration of one image onto another to be diffeomorphic: the priority of this model lies on physical validity in the first place and a good matching in the second. No tearing transformations are allowed to preserve the diffeomorphism constraint (cf. Section 3.3) [21].
- **Demons - Diffusion model:** This approach constrains the properties of the transformation function based on a diffusion process. First all image elements are selected

as demons. Subsequently, optical flow constraints are used to compute demon forces for displacement fields in an image matching procedure. Regularisation is performed using convolutions with Gaussian filters [72].

- **Curvature model:** This registration approach is formulated based on the curvature equilibrium equation. The regularisation is performed by allowing affine linear transformations to avoid preregistration of a linear and affine type [72].

2. Interpolation models

- **Radial Basis Function (RBF) based model - splines:** This approach defines control points (samples) in the template and target image. Correspondences further away from these samples are established using spline-based interpolation with respect to their distance to a control point [21] [72]. Examples are Thin-Plate Splines (TPS), Clamped-Plate Splines (CPS), Geodesic Interpolating Splines (GIS), multi-quadratics, Wenland functions, Wu functions or Elastic Body Splines (EBS) [72].
- **Basis-function based model:** In comparison to RBF, basis-function transformations are modelled based on analysis regarding wavelet and Fourier. Instead of estimating the distance to defined control points for interpolation, the correspondences are established by finding a linear combination of basis functions (cosine, Fourier or Wavelet basis functions). A further advantage using basis functions is the possibility to decompose displacement fields for multi-resolution computations [72].
- **Free-Form Deformation (FFD) model - B-splines:** the observed images are sampled using a regular grid. The deformation is computed by "*a summation of tensor products of univariate splines*" [72]. Extensions of FFD are cubic B-splines, multi level B-splines or Non Uniform Rational B-Splines (NURBS) [72].
- **Locally affine model:** This approach parametrises transformation functions by deformations which are locally linear. Piecewise affine or poly-affine models exist. Piecewise affine divides an image into a set of tetrahedras or triangles, and uses the resulting nodes as parametrisation of the transformation. Affine interpolation is used inside a region to obtain invertible deformations. A disadvantage is the reduced smoothness of region boundaries. In contrast to this, poly-affine models focus on estimating smooth transformations by dividing the image into fuzzy regions [72].

3. Models based on knowledge-based geometry

- **Statistical Deformation Model (SDM):** This approach aims at extracting statistical properties of transformations by analysing the population of observed subjects. Additionally, SDMs are able to reduce the problem's dimension to improve computational performance [72]. Examples for statistical tools used are Principal Component Analysis (PCA), the Gaussian Mixture Model (GMM) or Probability Density Function (PDF) estimation.
- **Biomechanical - Finite element (FE) model:** The images are divided into cells. A physical description (elastic, rigid, fluid, ...) of the anatomical structure is assigned

to each cell. Also external forces are applied to this model. The transformation deforms the template image according to the material behaviour defined for each cell [21]. Examples are tumor growth models, biomechanical models of the breast or prostate [72].

General Optimisation Framework for Deformable Registration

A general optimization framework for deformable registration is divided into three phases: loading, optimisation and update. In the loading phase the object for registration is loaded and if necessary preprocessed to obtain a whole image, image parts or object corresponding features. The next phase optimises the transformation function ϕ from a source I_0 to a target image I_1 based on a deformation model and by minimising an energy model E (cf. Equation 3.1 [72]).

$$E = \underset{\phi}{\operatorname{argmin}} \left[E_S(I_1, I_0 \circ \phi) + \lambda E_R(\phi) \right] \quad (3.1)$$

An energy model consists of two terms: a **similarity measure** E_S between target I_1 and transformed source image $I_T = I_0 \circ \phi$ and a **regularisation term** E_R . The latter term models the properties and constraints of the underlying deformation model (internal energy) [72]. In the last phase the current transformation function is updated according to the estimated result of the optimisation, it is used to transform the template object and to interpolate non-integer coordinates [85]. This procedure continues with the optimisation phase and is iterated for a predefined number of iterations or until a pre-defined threshold for E is reached [62]. Figure 3.2 schematically illustrates this optimisation process for the registration of a template to a target image.

Similarity Measure

In the optimisation phase of a deformable registration procedure correspondences between the template and target object are specified to optimise a transformation function. Similarity measures, feature descriptors or relationships among features in space are used for measuring differences between two images (global) or image sections (local) [31] [21]. Similarity measures must have an extremum in case the images are correctly aligned, they have to be smooth, differentiable and efficient to compute [72]. The underlying image modality influences the choice of the measuring procedure [31] [21]. In case of **mono-modal** registration the following **similarity measures** are used:

- **Sum of Absolute Difference (SAD):** Measures the sum of absolute distances between features x, y of two images or volumes I_0 and I_1 (cf. Equation 3.2).

$$SAD = \sum_i \|I_0(x_i) - I_1(y_i)\| \quad (3.2)$$

- **Sum of Squared Differences (SSD):** is used as similarity measurement for least-squares fitting (cf. Equation 3.3).

$$SSD = \sum_i (I_0(x_i) - I_1(y_i))^2 \quad (3.3)$$

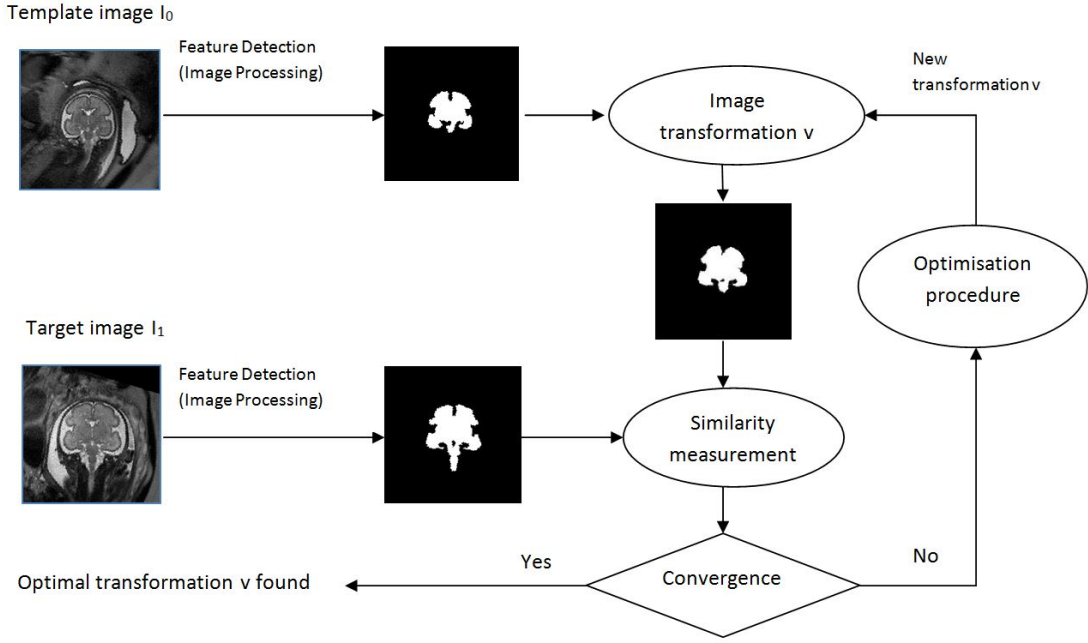


Figure 3.2: Optimisation procedure for estimating a mapping function for image registration. Figure modified from [62]. MR images courtesy of Medical University of Vienna (MUW).

- **Correlation Ratio (CR):** According to [21]: "The correlation ratio assumes a functional relationship between intensities. It can be defined in terms of sums and sums of squares of source voxels that correspond to a number N_i of iso-intense voxels in the target image" I_1 (cf. Equation 3.4 3.5 3.6 [21]).

$$CR [I_0, I_1] = 1 - \frac{1}{N\sigma^2} \sum_i N_i \sigma_i^2 \quad (3.4)$$

$$\sigma^2 = \frac{1}{N} \sum_{overlap(x)} I_0(x)^2 - m^2, m = \frac{1}{N} \sum_{overlap(x)} I_0(x) \quad (3.5)$$

$$\sigma_i^2 = \frac{1}{N_i} \sum_{x:I_1(x)=i} I_0(x)^2 - m_i^2, m_i = \frac{1}{N_i} \sum_{x:I_1(x)=i} I_0(x) \quad (3.6)$$

Multi-modal registration has the aim to find correspondences between two images or volumes of different modality, i.e. images with a more complex intensity relationship compared to images used for a mono-modal registration. The aim of multi-modal registration is to simulate a modality from the other. An example for a similarity measure used for **multi-modal** registration approaches is **Mutual Information (MI):** Computing of the MI assumes that a probabilistic relation between the intensity distribution of two images I_0 and I_1 is established (cf. Equation 3.7 and 3.8). H are terms representing the entropies of the intensity distribution. The entropy

reaches its maximum if the intensity distribution becomes uniform, i.e. if I_0 and I_1 are perfectly aligned. The joint entropy is minimal when the maximum of MI is reached. P denotes probability of intensity x occurring in I_0 and Q encodes the probability of the intensity y occurring in I_1 . p_{xy} denotes the joint probability of the intensities at the same place [21].

$$MI [I_1, I_2] = H_{I_2} + H_{I_1} - H_{I_1 I_2} \quad (3.7)$$

$$MI [I_1, I_2] = \sum_i \sum_j p_{xy}(i, j) \log \frac{p_{xy}(i, j)}{p_x(i)p_y(j)} \quad (3.8)$$

A further similarity measure used for multi-modal image registration is **Normalized Cross Correlation (NCC)**. Computing the NCC assumes that two images I_0 and I_1 both illustrate the feature of interest (x, y) (cf. Equation 3.9). \bar{I}_0 and \bar{I}_1 denote the mean values of the images I_0 and I_1 . The normalisation makes the NCC independent to brightness or contrast changes of the images, but is expensive to compute. In contrast to this NCC has a higher robustness in determining the position of the feature than SAD or covariance similarity measures [10].

$$NCC [I_0, I_1] = \frac{\sum_i ((I_0(x_i) - \bar{I}_0) * (I_1(y_i) - \bar{I}_1))}{\sqrt{\sum_i (I_0(x_i) - \bar{I}_0)^2 * \sum_i (I_1(y_i) - \bar{I}_1)^2}} \quad (3.9)$$

Regularisation Term

The deformable registration problem is under determined, since infinite solutions for deforming an image in a non-rigid way exist. For solving this problem regularisation is needed to alleviate ill-conditioned or unstable solutions and to constrain the optimised transformations to be topology-, volume- or rigidity-preserving [61]. Dependent on the deformation model chosen, one or more properties are satisfied. Additionally, regularisation enables the introduction of prior knowledge of the underlying tissue behaviour to overcome getting caught in local minima during optimisation. Regularisation is divided into explicit regularisation and implicit regularisation. Explicit regularisation uses two possible types of constraints: hard ones that have to be necessarily satisfied and soft constraints, which do not have to be. In contrast to this implicit regularisation uses smooth functions for parametrisation [72].

Spatial vs. Longitudinal Registration

In the field of spatial registration the focus lies on mapping two 3D images of the same or different modality. There are also approaches which register 2D data to 3D volumes. For modelling growing processes or for monitoring issues, time series of images are acquired (monitoring of bone or tumor growth, fetal brain development, postoperative healing). To compare monitoring events of different patients registration of time series of images have also been proposed [51]. Another type of longitudinal registration originates from the field of real time registration during surgical interventions. Here, pre-operative optimised high resolution image time series or synthetically modelled dynamic data are registered onto real time-data of different or identical modalities, captured during the intervention [46] [27].

All-to-one vs. Pairwise vs. Groupwise

For building reference images or volumes three types of procedures exist: All-to-one, pairwise and groupwise approaches. *All to one registration* is used in case of registering source images (all) to a reference template image (one). *Pairwise registration* creates biased templates, which have to be computed in advance. For this, correspondences between two images (a source and a target image) have to be determined. *Groupwise registration* approaches use an optimisation procedure to compute an unbiased reference model. No pre-computation of the template is necessary. For more details cf. Section 2.1 *Atlas Construction*.

3.3 Large Deformations Diffeomorphic Metric Mapping

The basic idea of Large Deformation Diffeomorphic Metric Mapping (LDDMM) is to register a template image I_0 and a target image I_1 using a diffeomorphic deformation model which constrains the transformation function obtained to be a diffeomorphism $\varphi : \Omega \rightarrow \Omega$. Ω denotes the image domain $\Omega \subseteq \mathbb{R}^d$ of dimension d . According to the Encyclopaedia of Mathematics¹, a diffeomorphism is defined as follows [36]: "A *one-to-one continuously-differentiable mapping of a differentiable manifold (e.g. of a domain in a Euclidean space) into a differentiable manifold for which the inverse mapping is also continuously differentiable*. If $f(M) = N$, one says that M and N are diffeomorphic.". The LDDMM problem is first studied by Trouvé (1995) [76] and Dupuis et al. [24]. Beg et al. [6] examine the Euler-Lagrange equations to solve this issue. The diffeomorphism φ is in this approach expressed as the end point ϕ_1 of a curve ϕ_t , $t \in [0, 1]$ where ϕ_0 is the identity. Beg et al. [6] estimate the optimal transformation in the space of smooth velocity vector fields V on the domain Ω . This is possible, because Trouvé (1995) and Dupuis et al. (1998) showed that a sufficient smoothing on allowable velocity vector fields in the space V makes sure that the solution to the differential equation (representing the flow of a time-dependent vector field) $\dot{\phi}_t = v_t(\phi_t)$, $t \in [0, 1], v_t \in V$ is in the space of diffeomorphisms. Beg et al. [6] formulate this issue by the cost function expressed in Equation 3.10, and is illustrated in Figure 3.3.

$$\hat{v} = \arg \min_{v: \dot{\phi}_t = v_t(\phi_t)} \left(\int_0^1 \|v_t\|_V^2 dt + \frac{1}{\sigma^2} \|I_0 \circ \phi_t^{-1} - I_1\|_{L^2}^2 \right) \quad (3.10)$$

The cost function consists, as introduced in Section 3.2, of two terms representing a similarity measure (image cost term) and a regularisation (deformation cost term):

- Image cost term: $\|I_0 \circ \phi_t^{-1} - I_1\|_{L^2}^2$ is a similarity measure and illustrates the squared of the L^2 difference of square integrable functions between the target image and the deformed template image. It characterises the "goodness" of the transformation.

¹Diffeomorphism. <http://www.encyclopediaofmath.org/index.php>; [accessed 13-September-2015]

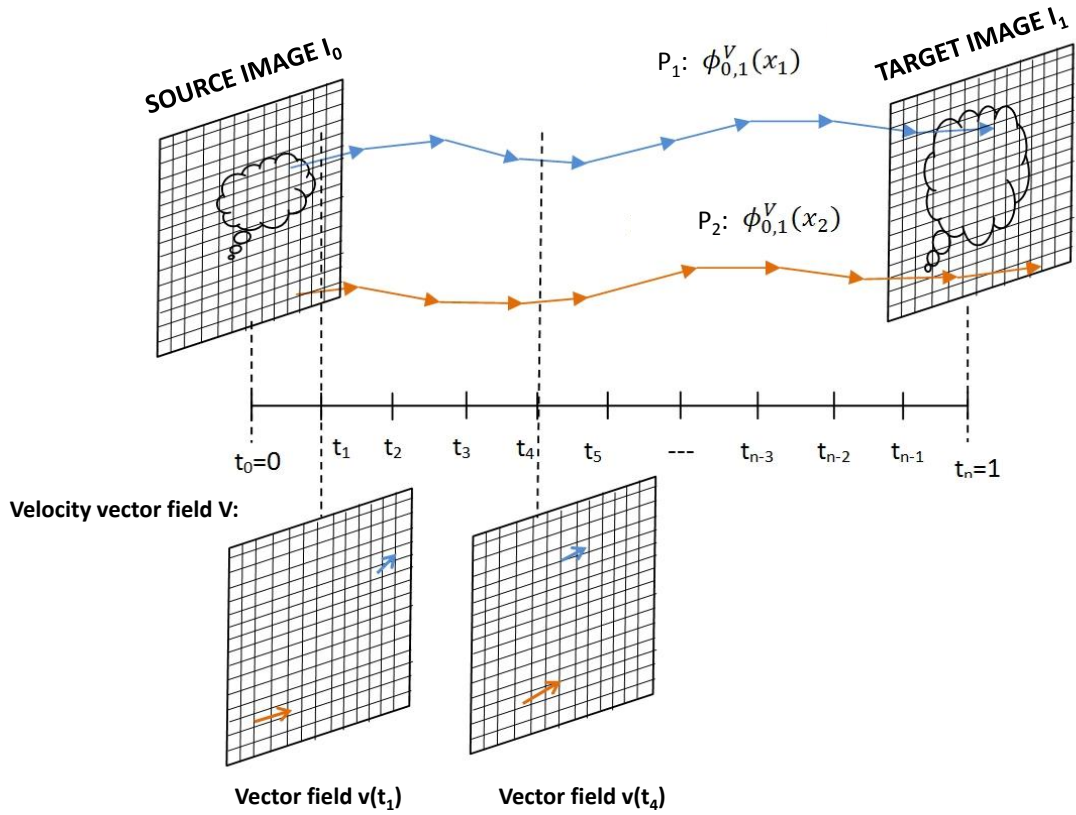


Figure 3.3: Schematic illustration of the concept of LDDMM. For clear representation only diffeomorphisms of two pixels P_1 and P_2 are shown. $\phi_{t_1,t_2}^V(x)$ is interpreted as the position at time t_2 of a pixel P that is at position x at time t_1 , in dependence on the associated velocity field V .

- Deformation cost term: $\int_0^1 \|v_t\|_V^2 dt$. It measures the smoothness of the estimated vector field via the norm on the space of vector fields V . The introduction of a differential operator L makes it possible to connect the different spaces of the deformation cost term and image cost term. Beg et al. prove the relation between these ($\|f\|_V = \|Lf\|_{L^2}$) in [6]. The deformation cost term is consequently reformulated as: $\int_0^1 \|Lv_t\|_{L^2}^2 dt$ and minimises according to increasing smoothness of the vector field. The optimal transformation is interpreted as the shortest diffeomorphism between two images, expressed by the vector field with the highest smoothness [6].

Beg et al. [6] realise the minimization of these cost terms by a gradient descent approach on the whole set of curves in the diffeomorphism group. The resulting time-depending vector field provides an optimized diffeomorphic transformation from template to target image.

3.4 Geodesic Shooting

The LDDMM approach needs the calculation of a series of velocity fields to find the optimal diffeomorphic mapping function from a template to a target image. In case of geodesic shooting, Ashburner et al. [2] estimate an initial velocity (v_0) and use it to derive an **initial momentum** u_0 expressed in Equation 3.11, where $A = L^\dagger L$ represents a model of the "inertia" of the system, i.e. a linear operator which operates on a time-dependent velocity that mediates the deformation over unit time.

$$u_0 = A * v_0 \quad (3.11)$$

The Ordinary Differential Equation (ODE) associated to the flow of the time-dependent velocity vector field $\dot{\phi}_t = v_t(\phi_t)$, $t \in [0, 1]$ is formulated in Equation 3.12 and shows that the velocity is given at any time by the initial velocity or momentum.

$$\dot{\phi}_t = K(|D\phi_t^{-1}|(D\phi_t^{-1})^T(u_0 \circ \phi_t^{-1})) \quad (3.12)$$

D denotes the Jacobian tensor, ϕ^{t-1} the inverse of the diffeomorphic mapping and the operator K the (pseudo-) inverse (Green's function) of $L^\dagger L$. It is applied to smooth the result. The **conservation of momentum** is the formulation of each iteration of the registration as an initial value problem. Geodesic shooting requires the following steps: The deformation at time point zero ϕ_0 is set to the identity transform (Id). Afterwards the initial momentum from the initial velocity is computed ($u_0 = L^\dagger L * v_0$) and the dynamical system $\dot{\phi}_t$ is integrated over unit time. A possible cost term for geodesic shooting is expressed in Equation 3.13.

$$E = \frac{1}{2} \|L^\dagger L v_0\|_{L^2}^2 dt + \frac{1}{2\sigma^2} \|I_0 \circ \phi_t^{-1} - I_1\|_{L^2}^2 \quad (3.13)$$

In comparison to LDDMM it is observed that the deformation cost term has changed. Instead of calculating a series of velocity fields, only the initial velocity has to be estimated. This cost term may differ in other geodesic shooting approaches [52] [2].

3.5 Geodesic Regression

In this master's thesis a longitudinal image regression approach is used for estimating a fetal brain atlas. Instead of using a combination of a template-building and interpolation technique as described in Section 2.1, geodesic shooting regression is used to compute a continuous time-dependent vector field encoding the longitudinal as well as time-specific variability of fetal brains. Figure 3.4 illustrates the basic concept of this approach: The aim is to find a time-dependent transformation (dark red line) from a source image to a target image representing the extremes of the gestational age range. For a given gestational age, the transformation function warps the source data (annotations, gray value images), to the corresponding time point in the age range, and thus is able to estimate time-dependent templates as well segmentations. In contrast to pairwise registration, the whole dataset is involved in the longitudinal registration procedure. The challenges of geodesic regression lie in defining the optimal velocity field regularisation parameters to model the detailed shape changes in time, induced by cortical folding processes. A detailed description of a geodesic regression algorithm, of Ashburner et al. [2] [1], is given in Section 6.3.

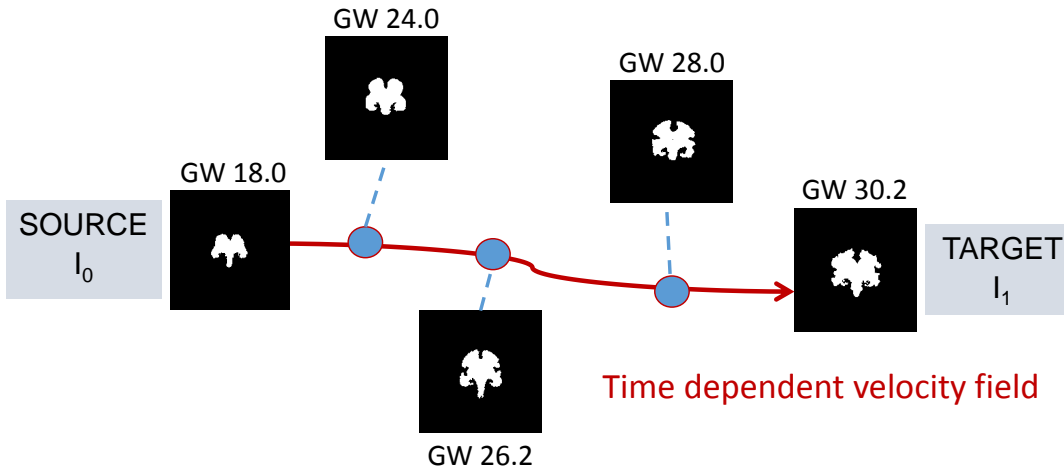


Figure 3.4: Schematic illustration of the concept of geodesic regression.

3.6 Summary

This chapter gives an overview of registration techniques for the construction of an atlas and for the propagation of atlas-based tissue maps to an image. For pairwise registering the volume changes of fetal brains and the different fetal orientation over gestational age [64] linear registration procedures ([51], [42], [85]) are introduced, consisting of translation, rotation, scaling or shearing transformations. For modelling the morphological changes of fetal brains (cortical folding) deformable (non-rigid) approaches ([72], [21]) are summarised in this chapter. The corresponding transformations are estimated using an optimisation framework [62] for minimizing a costfunction consisting of a similarity measure and a regularisation term. The non-rigid behaviour is influenced by the underlying deformation model. Physical, knowledge-based geometry or interpolation based models are presented ([72], [21], [85]). According to the analysis of state-of-the-art approaches (cf. Chapter 2) a pairwise and a longitudinal diffeomorphic registration approach are considered to learn an atlas of fetal brain development instead of combining a template building and an interpolation technique. This chapter concludes with an introduction to pairwise diffeomorphic registration (LDDMM [6] and geodesic shooting [78], [2]) and an introduction to longitudinal diffeomorphic registration (geodesic regression [1], [2]).

CHAPTER 4

Image Segmentation and Graphcuts

In this chapter an overview of image segmentation techniques is presented (cf. Chapter 4.2) and the basics of graph cuts are introduced. In Section 4.3 first binary graph cuts and then the Min-Cut/Max flow problem are explained. Section 4.4 gives an introduction to multi-label graph cuts. The Potts and Continuous Max-Flow (CMF) model formulation is discussed in Section 4.5 and Section 4.6. The analysis regarding the graph cut approach used are summarised in Chapter 6 in Section 6.4.

4.1 Denotation

Beside the denotations introduced in Section 3.1 the following additional terms are introduced to describe image segmentation procedures and graph cuts. G denotes a graph with the corresponding set E of edges and V of vertices denoted by the letters v, s, t , where s denotes the source and t the target (sink) vertex. $t - \text{links}$ are also named unary (cost) term and expressed using the denotation source flows $p_s(\cdot)$ and target flows $p(\cdot)$. $n - \text{links}$ are also denoted as binary or penalty term and have the additional notation as spatial flows $q(\cdot)$. The letter w is used to describe weights or labeling probabilities and $u_l(\cdot)$ to express a labeling function for a label l . The cost for assigning a label l to a image feature x is expressed by $D_x(\cdot)$ or $\rho(\cdot, \cdot)$.

4.2 Overview of Image Segmentation Methods

Medical image segmentation techniques give the possibility to determine the position and volume of anatomical structures. In the medical field this is needed to make diagnosis, medical simulations or different types of treatment planning (preoperative, postoperative, radiation treatment) [39] [50]. A segmentation is defined as an assignment of a label to a voxel that represents the underlying structure. Depending on the image acquisition technology (Computer Tomography (CT), Positron Emission Tomography (PET), MRI), occurring image artefacts make this task challenging and thus, have to be taken into account in the labeling procedure [39]. Table

2.2 gives an overview of medical image segmentation techniques divided into four main classes. Additionally, corresponding methods and examples are listed [39] [5].

- **Region-based:** These approaches focus on similarities within a region and differences between regions [39].
- **Boundary-based:** These methods are categorised into parametric and non parametric deformable models and are represented as curves or surfaces. Their form is influenceable by internal or external forces [5].
- **Hybrid techniques:** These techniques exploit region and boundary-image features [39].
- **Atlas based:** These approaches estimate image segmentations based on atlases [39].

Supervised vs. Unsupervised

Image segmentation approaches differentiate between manual, annotation-based (supervised) or automatic methods (unsupervised) [5]. Supervised image segmentation approaches require an initialisation for defining and placing an initial segmentation model in the image. Manual approaches require interaction of a user to identify the placement of an initial model. An extended version of manual initialisation are annotation-based approaches where users mark defined image locations. Thus, it is possible to involve prior knowledge to fit an initialisation model on to the marked points. Automatic approaches do not need interaction of users. The required initialisation model is encoded in templates and automatically obtained for example by a General Hough transformation or an atlas (reference model) computation [5]. Subsequently, the initialisation is performed by automatically registering the estimated template to the image.

Fetal Brain Segmentation Approaches

Fetal brain segmentation approaches are divided into supervised classification and automatic segmentation based methods [14].

Following approaches use supervised classification for labeling fetal brain tissue: **Weisenfeld et al.** [79] use probabilistic atlases for training a classifier for fetal MR tissue segmentation. In contrast to this, **Prastawa et al.** [56] use probabilistic atlases as features for classification. **Xue et al.** [81] perform non-supervised statistical tissue masking. They use label propagation as a prior in a Bayesian framework.

The following approaches segment images or volumes automatically: **Habas et al.** [35] propose an Expectation-Maximization (EM) Framework for building a probabilistic atlas for automatic fetal brain segmentation. **Claude et al.** [17] focus on automatic atlas-based labeling of the posterior fossa. **Cuadra et al.** [4] present a tissue labeling approach using an Expectation Maximization Markov Random Field (EM - MRF) procedure. **Keraudren et al.** [40] propose an approach for automatic segmentation of 2D MR slices for motion correction using Scale-Invariant Feature Transform (SIFT) and a combination of Maximally Stable Extremal Regions (MSER) and a Conditional Random Field (CRF). **Wright et al.** [80] adapt the automatic brain

Table 4.1: Overview of Medical Image Segmentation Techniques

Method Group	Methods	Examples
Region-based	Thresholding	
	Region growing	
	Region splitting	
	Merging	
	Clustering	k-means Fuzzy c-mean
	Bayesian	Maximum Likelihood (ML) Expectation Maximization (EM)
		Maximum a posteriori (MAP)
		Markov Random Field (MRF)
Boundary-based	Active contour (snakes)	Parametric
	Geometric active contour	Non-Parametric
	Level set	Edge Stopping Level sets Energy Minimizing Level Sets Level Sets Extensions
	Discrete	Meshes Particle Systems
		Active Shape Models (ASM) Active Appearance Models (AAM)
	Deformable Fourier Models	
	Modal Analysis based	
	Superquadrics	
	Graph-Cut Based	
	External Forces Model	Basic Forces (Pressure, Laplacian Smoothing, Simple Image)
		Advanced Forces (Image Intensity Profiles, Multiscale Gaussian Potential, Distance Potential, Dynamic Distance, Gradient Vector Flow, Omnidirectional Displacements)
		Interactive Forces
Hybrid	Levelset with regional forces	
	Graph cut with regional and boundary terms	
	Condition Random Fields	
Atlas-based	Atlas as average shape	Active Shape Models (ASM) Active Appearance Models (AAM)
	Atlas as individual image	Registration Methods

extraction algorithm of **Eskildsen et al.** [26] for fetal brains. This approach is based on nonlocal segmentation techniques and the resulting segmentations are used to investigate the cortical folding patterns of fetuses' brains. **Gholipour et al.** [30] propose an automatic segmentation procedure for studying ventriculomegaly using a multi-atlas multi-shape approach.

Relation to this Thesis

This master's thesis aims to create an automatic tissue labeling framework for fetal brains, since manual segmentation approaches are time-consuming, need experts and consequently lead to higher costs [5] compared to automatic approaches. For creating an automatic segmentation framework, state-of-the-art approaches as introduced in Section 4.2, are atlas-based. For obtaining automatisation, the framework introduced uses a diffeomorphic longitudinal atlas as initialisation of a graph cut based segmentation approach. Apart from the advantage of automatic segmentation, a further benefit of graph cuts is the possibility to perform multiple label estimation, since a segmentation of two brain structure types (cortex, ventricles) is examined in this work. For this master's thesis the CMF formulation is used to define tissue priors between values 0 and 1, to be able to use the value range of the atlas based prior maps. Thus, the min cut/max flow formulation which only accepts a labeling value of 0 or 1 is not considered in this thesis.

4.3 Binary Graph Cuts

An introduction to binary graph cuts is given for a better understanding of the multi label approach. The aim of binary graph cuts is to segment an image or volume I of size $a \times b \times d$ in two regions: foreground and background. Therefore, every pixel $x \in I$, $I = \{z_1, \dots, z_m\}$ is interpreted as a node x in a graph $G = \langle V, E \rangle$. V represents the set of vertices in the graph; $V = \{X, s, t\}$: $X = \{x_1, \dots, x_m\}$ the set of pixel corresponding nodes, a source node s (representing the background) and a target node t (representing the foreground). E is the set of directed edges. Two types of connections exist [8]:

1. t-links: Connections between every pixel node with the source and sink node with a weight $w(x, q)$, $x \in X$, $q \in \{s, t\}$. w represents the probability of a node x being background ($q = s$) or foreground ($q = t$). These weights are derived from atlas based segmentations. T is the set of all t-links.
2. n-links: Interconnections between pixels with a weight $w(x, y)$, $(x, y) \in X$, $x \neq y$. $w(x, y)$ represents the probability of the nodes x and y being from different regions. For these weights a local gradient of the image is used. N is the set of all n-links.

Figure 4.1 illustrates the principle organisation of the graph used. On the left an input image is presented. In the middle a rough division of the image (representing the pixels) is shown by using labeled circles. These are used as nodes in the graph and are illustrated in yellow (foreground) and in blue (background). On the right, for achieving a clearer level of visualisation only the nodes of one row of the input image are shown. The t-links are marked in black the n-links are marked in red.

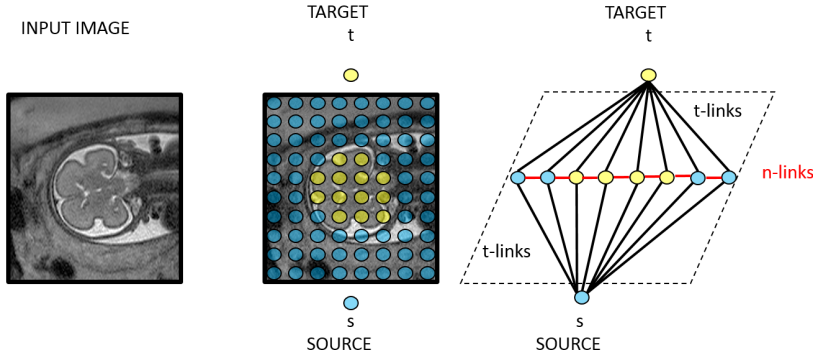


Figure 4.1: Illustration of the principle of a binary graph cut approach. MR image courtesy of Medical University of Vienna (MUW).

Min-Cut Problem

For the segmentation of an image into fore- and background, an optimal cut C through the graph has to be determined such that the nodes are partitioned into two disjoint subsets T (foreground) and S (background). The cost of a cut is measured by summing up the weights of the cut edges (t-links and n-links). In Equation 4.1 the mathematical formulation of the cut cost function is illustrated.

$$|C| = \sum_{x \in X, q \in \{s, t\}} w(x, q) + \sum_{(x, y) \in X, x \in T, y \in S} w(x, y) \quad (4.1)$$

A cut is interpreted as a binary labeling of pixels in an image, expressed by a mapping function $u_l(\cdot)$: $u_l(x) = l$, $l \in \{0, 1\}$. Nodes that correspond to the subset S after the cut receive the label 0 and nodes in the subset T the label 1. Thus, the cost function is rewritten in terms of the energy of the corresponding labeling function $u_l(\cdot)$ as expressed in Equation 4.2 where L consists only of two label types (foreground and background) in the binary case. In a combinatorial optimisation procedure the min-cut problem is solved by finding the minimum cost term among all cuts. The maximum flow problem is defined as the determination of a maximum flow from S to T , that saturates a set of edges in the graph by dividing the nodes into two disjoint subsets $\{S, T\}$. Based on the formulation of these two problems the minimum cut cost is equal to the maximum flow value from the source to the target [8].

4.4 Multi Label Graph Cuts

In this section the binary graph cut approach, observing two labels, is extended to multi labels. The task of the multi label approach is to segment an image or a volume $I = \{pix_1, \dots, pix_m\}$ of size $m = a \times b \times d$ into n regions. In contrast to the binary graph, we have additional target nodes representing the labels and consequently additional t-link edges connecting the pixels with each of them. A mapping function $u_l(\cdot)$ is used to assign a label $l \in L = \{l_1, \dots, l_n\}$ to a node

$x \in X$ in the graph. The energy of the multi label mapping function is expressed in Equation 4.2 [8].

$$E(u_l) = |C| = \sum_{x \in X} D_x(u_l(x)) + \sum_{(x,y) \in X} P_{xy}(u_l(x), u_l(y)) \quad (4.2)$$

$D_x(u_l(x))$ stands for the cost for assigning a label l to a pixel node x .

P_{xy} represents the pairwise interaction potential between neighboured pixels where $x, y \in X$ and $x \neq y$. The task of multi label graph cuts as well as of the binary graph cut is to find the minimum cut. There exist different optimization approaches, e.g. the **exact multi label optimization** where labels are assumed to be integers in the range $L = \{1, \dots, n\}$ such that Equation 4.3 is valid.

$$P_{xy} = \lambda |u_l(x) - u_l(y)| \quad (4.3)$$

In comparison to this, the **approximate optimization** approach uses the Potts model (cf. Section 4.5) where Equation 4.3 is reformulated into Equation 4.4.

$$P_{xy} = \lambda_{xy} * Id(u(x) \neq u(y)) \quad (4.4)$$

$Id(\cdot)$ is the identity function and equals one if its argument is true and zero otherwise [8].

4.5 Potts Models

The Potts model partitions a continuous image domain Ω into n disjoint subdomains $\{\Omega_l\}$ where $l \in L = \{l_1, \dots, l_n\}$ represents the set of labels for each region and minimizes Equation 4.5 [83]. L denotes the set of labels, $x \in \Omega$, $|\sigma\Omega_l|$ is the weighted length of each region Ω_l , $\rho(l, x)$ computes the costs for assigning the label l to the pixel x and λ represents a weighting term.

$$\min_{\{\Omega_l\}} \sum_{l \in L} \int_{\Omega_l} \rho(l, x) dx + \lambda \sum_{l \in L} |\sigma\Omega_l| \quad (4.5)$$

$$\text{s.t. } \bigcup_{l \in L} \Omega_l = \Omega, \Omega_{l_r} \cap \Omega_{l_s} = \{\}, l_r \text{ and } l_s \in L, \forall r \neq s$$

Convex Relaxation and Partially-Ordered Potts Model

The difference between the Potts model and the convex relaxed Potts model lies in the definition of the labeling boundaries. Since the Potts model specifies tight labeling boundaries represented by the labeling function $u_l(\cdot)$ in Equation 4.6, the convex relaxed Potts model relaxes the binary constraints to an interval between zero and one (cf. Equation 4.7)

$$u_l(x) = \begin{cases} 1, & x \in \Omega_l \\ 0, & x \notin \Omega_l \end{cases}, l \in L = \{l_1, \dots, l_n\} \quad (4.6)$$

$$\forall x \in \Omega : \sum_{l \in L} u_l(x) = 1; u_l(x) \in [0, 1] \quad (4.7)$$

If the results of the relaxed convex optimization problem are computed in the continuous image domain Ω , a continuous **min-cut model** (cf. Equation 4.8) for graph cuts is obtained by reformulating Equation 4.5 in terms of the labeling function $u_l(\cdot)$ used [83].

$$\min_{u_l \in U} \sum_{l \in L} \int_{\Omega} u_l(x) \rho(l, x) dx + \alpha \sum_{l \in L} \int_{\Omega} |\nabla u_l| dx \quad (4.8)$$

$u_l(x)$... labeling function for label l of the corresponding region Ω_L
 U ... represents the convex constrained set of labeling functions $u_l(x)$, $U = \{(u_{l_1}(x), \dots, u_{l_n}(x))\}$
 $\int_{\Omega} |\nabla u_l| dx$... the perimeter of each disjoint subdomain - determines the pairwise interaction potential between neighbouring pixels [83].

4.6 Continuous Max-Flow Model

The continuous max-flow model is also dual to the minimum cut through a graph from source to target, as discussed in Section 4.3 for the max-flow model. It is formulated in a binary as well as in a multi-label way and the corresponding setup is illustrated in Figure 4.2 for the multi label case. This formulation assumes n labels. The continuous image domain Ω is copied n times,

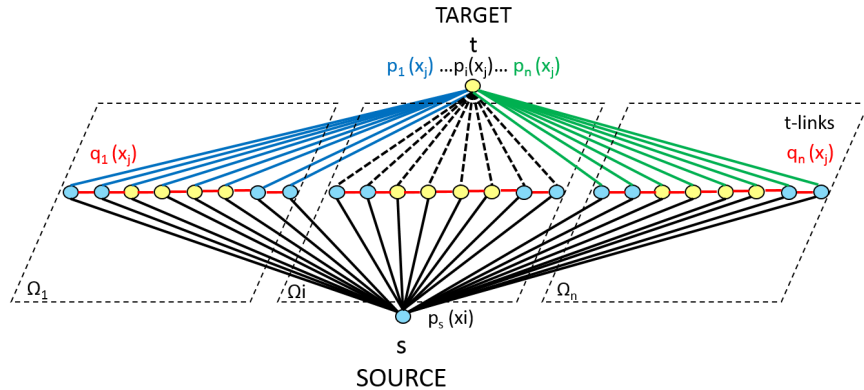


Figure 4.2: Example for a setup of a continuous maximum flow formulation with multiple labels: The unique source flows $p_s(x_j)$, target flows $p_i(x)$ and spatial flows $\{q_i(x)\}$ are marked on the corresponding edges in the graph. For a clearer visualisation only the nodes (blue and yellow circles) of one row in an image are illustrated.

where $\Omega = \{\Omega_i, i = 1 \dots n\}$. Three flow types ($p_l(x_j)$, $q_l(x_j)$ and $p_s(x_j)$) are defined for every position x_j in every image copy ($x_j \in \Omega_i$) [83].

- The source flow $p_s(x_j)$ leads from source to every position x_j in every image copy where $p_s(x_j)$ is unique, since the same source flow field is assumed for every image copy.

- The sink flow $p_i(x_j)$ flows from every position x in every image copy to the target. There are n different target flow fields $p(x) = \{p_i(x)\}$, $i = 1 \dots n$.
- The spatial flow fields $q(x_j) = \{q_i(x_j)\}$, $i = 1 \dots n$ are defined within each copy of Ω_i and are different for every image copy.

The flow constraints in Equation 4.9 and 4.10 have to be observed for every position x_j in every copy Ω_i of the image domain [83].

$$|q_i(x)| \leq C_i(x), p_i(x) \leq \rho(l_i, x), i = 1 \dots n \quad (4.9)$$

$$(div q_i - p_s + p_i)(x) = 0, i = 1 \dots n \quad (4.10)$$

Then the continuous max-flow model is defined as expressed in Equation 4.11.

$$\max_{\{p_s, p, q\}} \left\{ \int_{\Omega} p_s dx \right\} \quad (4.11)$$

4.7 Summary

The aim of this thesis is to provide a labeling framework for fetal brain tissue. Thus, first an overview of state-of-the-art segmentation techniques is presented in this chapter. The approaches introduced are divided into region-based, boundary-based, hybrid and atlas based techniques. Subsequently the difference between supervised and unsupervised labeling is explained and fetal brain segmentation approaches in these fields are summarised. Since manual segmentation approaches are time-consuming, need experts and consequently lead to higher costs [5], an automatic segmentation approach based on a graph cut formulation is used, which can be initialised by a diffeomorphic longitudinal atlas. This chapter concludes with an introduction to binary and multi label graph cuts and presents the Potts Model and CMF based formulation.

CHAPTER 5

Preliminary Experiments

This chapter documents the preliminary experiments for this thesis. They are performed to test the behaviour of a state-of-the-art diffeomorphic pairwise registration algorithm, if it is possible to model the changes of the fetal brain during pregnancy and to investigate which preprocessing pipeline is required. The same denotation introduced in Section 3.1 and 4.1 is used to document the preliminary experiments.

The behaviour of diffeomorphic registration of two dimensional fetal brain images is analysed using the LDDMM algorithm of Davis¹, which is based on the LDDMM formulation proposed by Beg et. al [6]. They formulate the optimal transformation vector field \hat{v} as denoted in Equation 5.1.

$$\hat{v} = \arg \inf_{v \in L^2([0,1], V)} E(v) = \left(\int_0^1 \|v_t\|_V^2 dt + \frac{1}{\sigma^2} \|I_0 \circ \phi_{1,0}^v - I_1\|_{L^2}^2 \right) \quad (5.1)$$

$\|v_t\|_V$ is the expression of the Sobolev norm on the velocity field $v_t(\cdot)$ and $\|\cdot\|_{L^2}$ represents the squared-error norm. I_0 denotes the template and I_1 the target image in the range $t \in [0, 1]$. The geodesic shortest paths are determined by computing $\int_0^1 \|v_t\|_V dt$ and $\phi_{1,0}^v$ stands for the velocity field dependent diffeomorphic transformation from template at $t = 0$ to target at $t = 1$. Beg et. al [6] use the gradient of the costfunction $E(v)$ in a gradient descent approach to find the optimal transformation vector field. The gradient of Equation 5.1 leads to the Fréchet derivative ∇_v, E_t in the vector field space V and is expressed in Equation 5.2.

$$(\nabla_v, E_t)_V = 2v_t - K \left(\frac{2}{\sigma^2} \left| D\phi_{t,1}^{\hat{v}} \right| \nabla I_t^0 (I_t^0 - I_t^1) \right) \quad (5.2)$$

¹<https://code.google.com/p/iawerksmatlab/source/browse/trunk/Algorithms/LDDMM/?r=3;> [accessed 13-September-2015]

Instead of calculating a transformation vector field from template to target, two mappings $v_1 = \phi_{0,t}$ and $v_2 = \phi_{1,t}$ are computed:

The first vector field (v_1) transforms the template image at $t = 0$ to a time point t and the second (v_2) transforms the target image at $t = 1$ to the same time point t . Subsequently, the resulting transformed images $I_t^0 = I_0 \circ \phi_{t,0}$ and $I_t^1 = I_1 \circ \phi_{t,1}$ are compared and the difference is determined. K denotes a compact self-adjoint operator. Since the Sobolev norm has to be obtained in space V and the squared error norm in space L^2 , K enables V to be defined through a differential operator L . Assuming that a and b are smooth vector fields in vector space V , and L^\dagger is the adjoint of L , we receive the following constraints concerning K [6]:

- $K(L^\dagger L)a = a$
- $\langle a, b \rangle_{L^2} = \langle Ka, b \rangle_V$

This formulation enables to achieve an optimisation solution in the space of vector fields V [6] and is necessary to include results of one optimisation step in the update of the transformation vector field $v^{n+1} = v^n - \epsilon \nabla_{v^n} E$ after each iteration. ∇I_t^0 is the gradient of I_t^0 and $\phi_{t,1}$. $|D\phi_{t,1}^{\hat{v}}|$ denotes the determinant of the Jacobian D . The analysed algorithm of Bradley C. Davis uses the formulation of the costfunction by Beg et al. [6]. The algorithm first loads the template and the target image and initialises the following parameters:

- σ : Weights the smoothed velocity field in the gradient energy computation
- ϵ : Weights the gradient energy in the velocity update equation
- α, β and γ : Determine the smoothing of the velocity fields.
The values are by default: $\alpha = 0.5, \beta = 0, \gamma = 1$.
- maxIter: Defines the maximum number of iterations
- N: Defines the smoothness steps of the vector field at one iteration step from time point zero to time point one.
- I_0 and I_1 : Template- and target image for pairwise registration.
- v (optional): Requires an initial vector field or zero value as input. In case of zero, the vector field is initialised by zero values.

In every iteration step the template image and target image are transformed by the current vector field. After this step the similarity between these two transformed images is measured and the Fréchet derivative of the cost function is calculated. According to the computational results, the vector field is updated and a new iteration step is entered till the predefined maximum number of iterations is reached. After termination the algorithm has the optimised transformation vector field as an output.

The following four experimental groups are executed to analyse the behaviour of the algorithm:

1. Experiments regarding the composition of vector fields (cf. Section 5.1)

2. Experiments regarding alignment (rotation, translation, scaling) (cf. Section 5.2)
3. Analysis regarding the dependence between registration result and the GW differences of source and template image used (cf. Section 5.3)
4. Experiments regarding the initialisation of registration procedures (cf. Section 5.4)

Every experiment is based on a research question which is answered in its documentation. To determine the quality of the registration, the similarity between the transformed template and the target image is measured by computing the DC [22] as expressed in Equation 5.3, where $P(\cdot)$ denotes the set of segmentation corresponding pixels, I_0^T the transformed template image and I_1 the target image. It is assumed that I_0^T and I_1 have the same image size.

$$DC(I_0^T, I_1) = \frac{2 * (P(I_0^T) \cap P(I_1))}{P(I_0^T) * P(I_1)} \quad (5.3)$$

5.1 Experiment 1: Analysis Regarding the Composition of Vector Fields

The following research questions are answered in this experiment:

"Is it possible to use a composition of a forward and an inverted backward transformation, which is estimated by registering source and target to an average image? Is it possible to use this composed deformation to map a source image to a target image directly?"

The following parameter setting is used:

$N=15$, $\sigma=0.09$, $\epsilon=0.001$, $[\alpha, \beta, \gamma]=[0.5, 0, 1]$, $v_0=[]$.

In experiment 1, two composition methods for calculating the DC of the registration results are compared. The algorithm outputs a forward v_1 and a backward v_2 transformation from source and target to an average image. For computing the DC two methods are considered in this experiment and illustrated in Figure 5.1:

- **Method 1:** This method is illustrated at the top of Figure 5.1 and transforms the source image at time point 0 by the deformation v obtained by the composition of v_1 and $-v_2$ ($I_1^0 = (I_0 \circ v_1) \circ -v_2$). The DC is computed using the target I_1 and transformed source I_1^0 image as input.
- **Method 2:** This method is illustrated at the bottom of Figure 5.1. Two estimated transformations v_1, v_2 are used to compute average images at a time point t . For calculating the DC a transformed source image ($I_t^0 = I_0 \circ v_1$) and a transformed target ($I_t^1 = I_1 \circ v_2$) image at time point t are compared.

For this experiment images with a GW difference of less than five GWs (image No. 19 (GW 19 day 2) and image No. 22 (GW 23 day 4)) and with a GW difference of twelve weeks (image No. 31 (GW 18) and image No. 39 (GW 30)) are used.

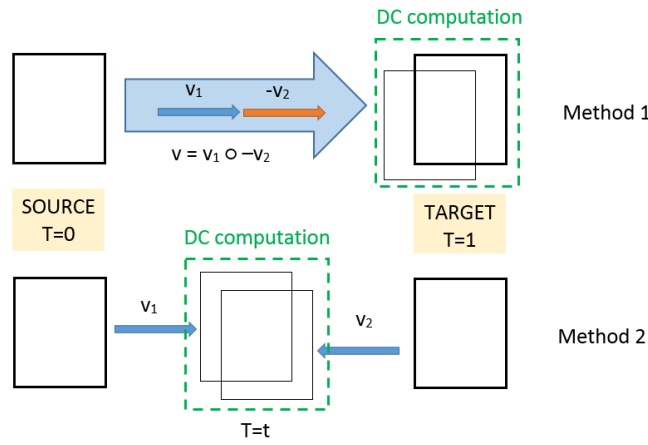


Figure 5.1: Schematic illustration of the two methods how DC computation is performed for experiment 1.

Results: In Figure 5.2 the results of experiment 1 are shown. Method 2 scores a higher DC than method 1, independent from the GA difference of the registered images. This fact is explained by the structure of the algorithm of Bradley C. Davis which optimizes the vector field based on the comparison using Method 2.

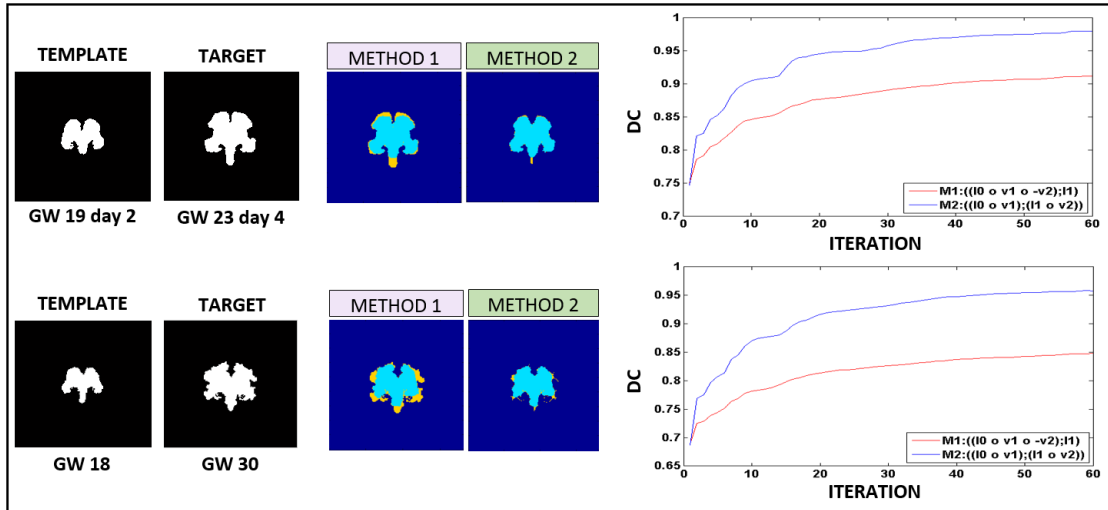


Figure 5.2: Results of experiment 1 using images with GW difference of less than five weeks and a GW difference of 11 weeks.

5.2 Experiment 2: Analysis Regarding the Preprocessing of Template and Target Images

The second group of experiments investigates the behaviour of the LDDMM registration approach in case of existing alignment relations between template and target image. Binary 2D images are created by using the software introduced in Section 6.2. Instead of comparing two transformed pictures at a time point t , as described in Section 5.1, only the template image I_0 is transformed from time point $t=0$ to $t=1$. Therefore the resulting vector fields v_1 and v_2 are used: $I_1^0 = (I_0 \circ v_1) \circ -v_2$. For calculating the DC, the transformed image I_1^0 is compared with the target picture I_1 . The results of this comparison are visualised using **labeled images** which illustrate True Negative (TN) pixels in dark blue, True Positive (TP) pixels in light blue, False Negative (FN) pixels in yellow and False Positive (FP) in dark red.

Rigid Alignment

The following research questions are answered in this experiment:

"Does alignment as preprocessing step improve the DC if two 2D binary brain images are registered using LDDMM? Is it possible to model rotational and translational mapping behaviour of vector fields using LDDMM?"

The following parameter setting for the alignment experiment is used:

$N=10$, $\sigma=0.09$, $\epsilon=0.001$, $[\alpha, \beta, \gamma]=[0.5, 0, 1]$, $v_0=[]$.

Results: In Figure 5.3 in the first row the LDDMM registration result of two non rotated, non centred or aligned pictures is shown. Image No. 1 (GW 26 days 2) and image No. 3 (GW 26 days 2) are used to create binary brain images. No alignment leads to gradual disappearance of the template image (i.e. rising number of background pixels), caused by the behaviour of the algorithm. The parametrisation of external and internal forces are able to execute local transformations. Instead of moving the template image in the direction of the target image, the external forces compress the picture. The algorithm is not able to provide a vector field that contains translational information. Since no alignment is achieved, consequently a DC of 0.0 is scored. In the second row of Figure 5.3 the registration result using two rotated and horizontally but not vertically aligned pictures is shown. As template and target image No. 1 (GW 26 day 2) and image No. 2 (GW 26) are used. The missing vertical alignment leads to a widening of the InterHemispheric Fissure (IHF). According to the illustrated TP pixels in the brainstem region, it is concluded that it is possible to register the brainstem of the template to the brainstem form of the target. In total a DC of 0.8 is reached after 60 iteration steps. In the third row of Figure 5.2 the result of two rigidly aligned images is presented. Rotated, centred and aligned images are used: image No. 1 (GW 26 day 2) and image No. 2 (GW 26). After 60 iterations a DC of 0.97 is reached. According to these results, all images in the dataset are preprocessed to be in rigid alignment.

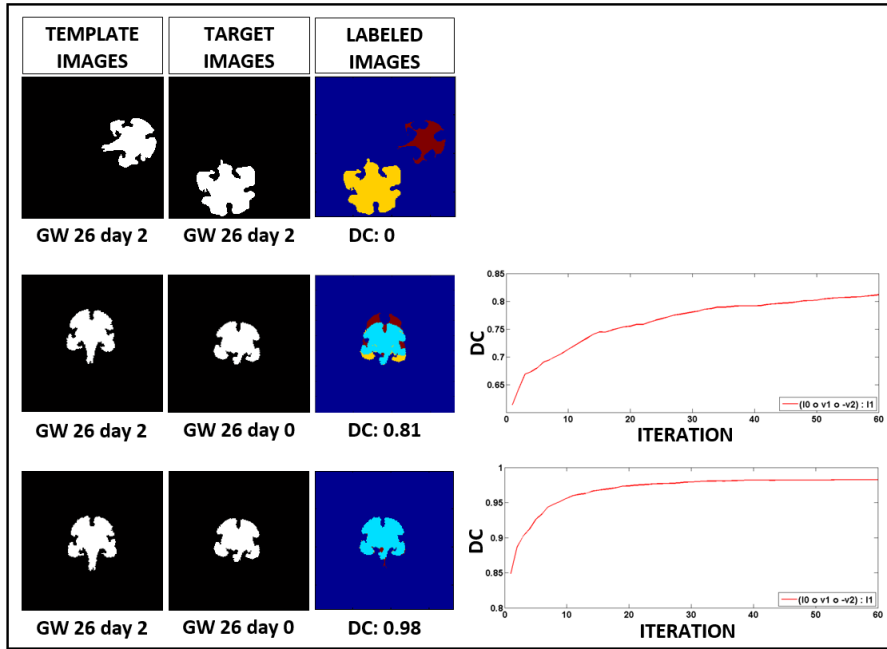


Figure 5.3: Illustration of experimental results regarding the rigid alignment of template and target images. The first row illustrates the registration result of two non rotated aligned centred pictures. The second row shows the registration result of two rotated horizontally but not vertically aligned pictures. The third row represents the registration results of two rigid aligned pictures. TN pixels are marked in dark blue, TP pixels in light blue, FN pixels in yellow and FP pixels in dark red.

Image Scaling

The following research questions are answered in this experiment:

"Does the scaling of two binary 2D brain images influence the quality of the registration? Which image properties are influenced by the parameter σ ?"

The following parameter settings are used:

1. Setting: $N=30, \sigma=0.090, \epsilon=0.001, [\alpha, \beta, \gamma]=[0.5, 0, 1]$.
2. Setting: $N=30, \sigma=0.05, \epsilon=0.0002, [\alpha, \beta, \gamma]=[0.5, 0, 1]$.

The following analysis shows the quality of registration of scaled and non-scaled images. Transformation method 1 ($I_1^0 = (I_0 \circ v_1) \circ -v_2$) is used for calculating the DC. The algorithm models differences in scaling or local detail between source and target image, dependent on the parameter σ . It is responsible for the weighting of the smoothed velocity field in the gradient energy computation. Thus, two runs of LDDMM with a different σ (weight of the smooth vector field) and ϵ parameters (weight of the gradient of the cost function) are considered when registering non-scaled images. Therefore, the first run uses the parameter setting 1: 0.09 for σ is used for

compensating the differences between shape size. The resulting optimized velocity field is used as initialisation of the second run with parameter setting 2: a different value of 0.05 for σ is used to register details in brain structure like the cortical foldings. For registering scaled images only one run of the algorithm with parameter setting 2 is performed.

Results: The results are visualised in Figure 5.4. On the right the DC as function of the iteration step is illustrated. The first (green) and second (red) run for non-scaled images as well as the single run (blue) for scaled images are illustrated. In the first column the template images I_0 and in the second column the target images I_1 are presented. In the third column the similarity between transformed template and template image is illustrated using a labelled image. TN pixels are marked in dark blue, TP pixels in light blue, FN pixels in yellow and FP in dark red. The first case shown at the top of Figure 5.4 uses images with a GW difference \geq five weeks:

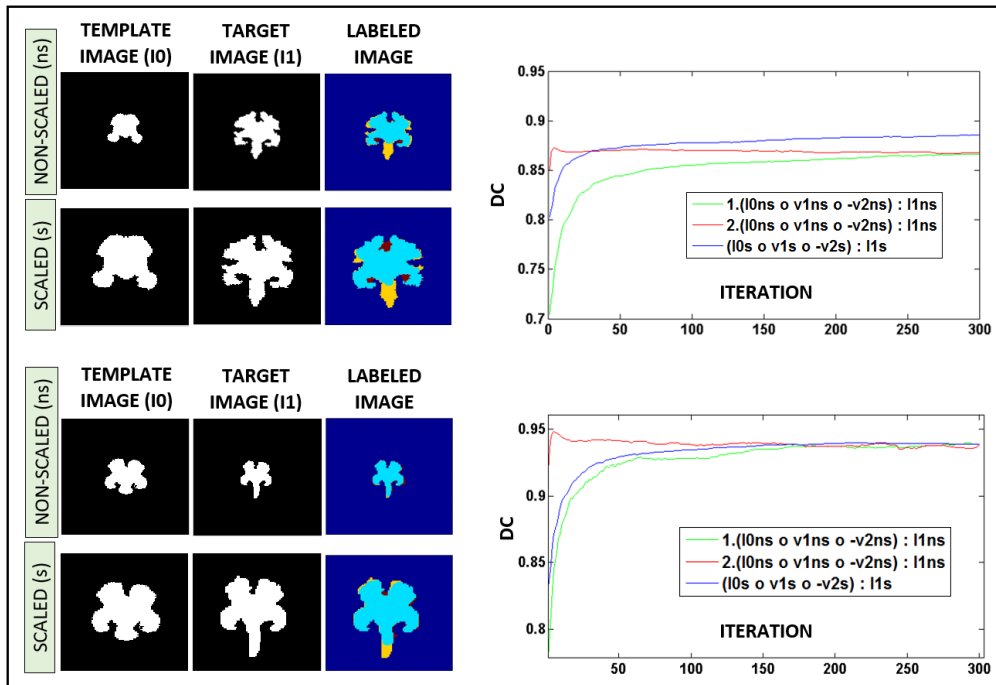


Figure 5.4: Illustration of experimental result regarding the analysis of the differences between using scaling and non-scaling as preprocessing step. TN pixels are marked in dark blue, TP pixels in light blue, FN pixels in yellow and FP pixels in dark red.

Image 26 (GW 22 day 5) and image 46 (GW 29 day 5). The DC is 0.88 in the scaled case and 0.86 in the non-scaled case converging to value 0.87 for scaled and non-scaled images. The corresponding labeled image shows that the deep cortical foldIHf is registered in a more detailed way using non-scaled images than scaled ones.

The second case is shown below in Figure 5.4 and uses images with a GW difference \leq five weeks: Image No. 34 (GW 21 day 5) and image No. 25 (GW 20 day 6). At iteration step 200 the DC of scaled and non-scaled pictures converges to 0.94. The corresponding labelled image

shows a more detailed registration using non-scaled images compared to scaled pictures.

5.3 Experiment 3: Analysis Regarding the Dependence Between GW Difference and Registration Result

The following research question is answered in this experiment:

"Is there a relation between the DC and the GW-difference of pairwise-registered binary brain images?"

The following parameter settings are used:

1. Setting: N=15, maxIter=100, $\sigma=0.09$, $\epsilon=0.003$, $[\alpha,\beta,\gamma]=[0.5, 0, 1]$.
2. Setting: N=15, maxIter=50, $\sigma=0.05$, $\epsilon=0.0002$, $[\alpha,\beta,\gamma]=[0.5, 0, 1]$.

All images in the dataset used are rigidly aligned and scaled to a fixed cortical radius size of 60 pixels. In Table 5.1 the image number in the dataset and the corresponding gestational age in GWs and in GDs are summarised. Transformation method one (cf. experiment 1 in Section 5.1)

Table 5.1: Illustration of image numbers (No.) used in the dataset and corresponding gestational age expressed in gestational weeks.days (GW.D) and in gestational days GD.

Image No.	31	44	43	35	25	30	20
GW+D	18	19.3	19.6	20	20.6	20.6	21.3
GD	126	136	139	140	146	146	150
Image No.	21	19	34	29	23	32	17
GW+D	21.4	21.5	21.5	22	22.2	22.4	22.5
GD	151	152	152	154	156	158	159
Image No.	26	18	22	16	33	24	6
GW+D	22.5	23.3	23.4	24	24.2	24.3	24.4
GD	159	164	165	168	170	171	172
Image No.	12	8	2	1	3	9	10
GW+D	25.4	25.5	26	26.2	26.2	26.4	27
GD	179	180	182	184	184	186	189
Image No.	4	14	5	27	36	11	28
GW+D	27.2	27.2	28	28	28.1	28.3	28.4
GD	191	191	196	196	197	199	200
Image No.	38	45	37	46	39	7	40
GW+D	29	29	29.3	29.5	30	30.2	30.2
GD	203	203	206	208	210	212	212

is used to calculate the composition of the vector fields. For images with a GW difference greater

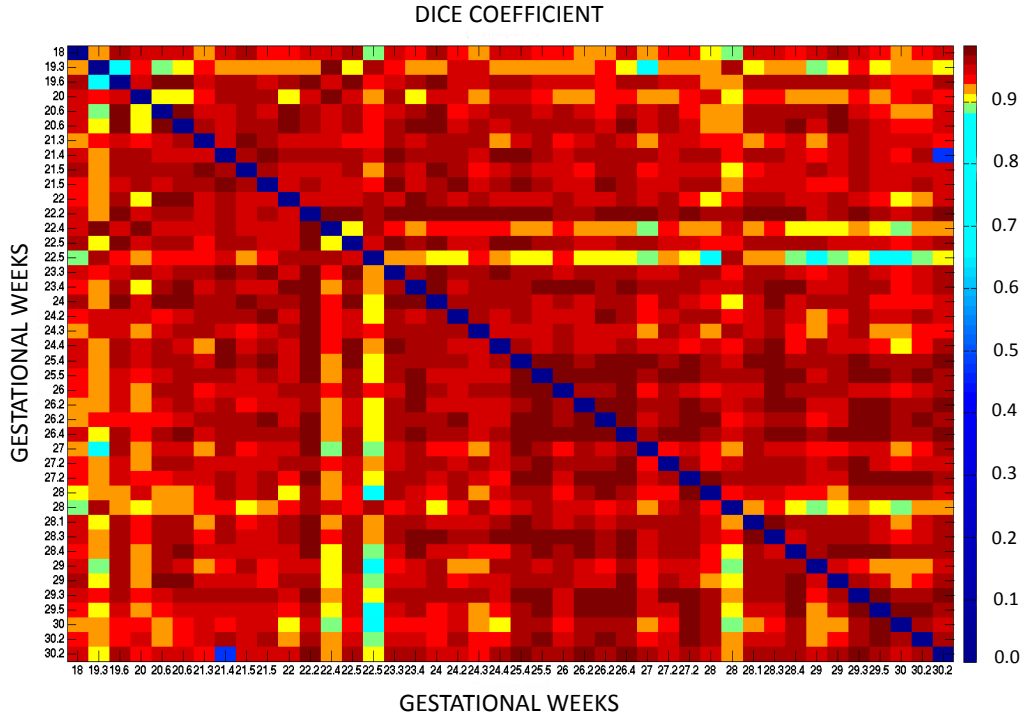


Figure 5.5: Dice coefficient matrix. The dataset used is rigidly aligned and scaled. For images with a GW difference greater than five weeks the following parameters are used: N: 15, iterations: 100, ϵ : 0.003 and σ : 0.09. For a GW difference smaller than five weeks, the same parameters are used for N, ϵ and σ . The iterations are set to 50 to reduce computation time.

than five weeks parameter setting 1 is used. The difference between the sets lie in the number of iterations. For registering images with a GW difference smaller than five weeks parameter setting 2 with 50 instead of 100 iterations is used to reduce computation time.

Results: Figure 5.5 illustrates the DCs of the pairwise registration of the images in the dataset. The computation and visualisation of a DC matrix makes it possible to investigate relations between registration quality and GW difference. Due to the age dependent increase of the local variability of the cortex, a rising DC is expected with increasing GW difference between the two registered images. In this experiment no rising of DC at the extremes of the gestational age range is observed. Due to the GW-difference dependent parametrisation of the iteration steps clear boundaries between GW 22 and 22.2 are visible as well as between GW 24.4 and 25.4. Pairwise registration involving images with No. 44 (GW 19 day 3), 35 (GW 20), 32 (GW 22 day 4), 26 (GW 22 day 5) and 27 (GW 28) shows a more than three times lower DC than 0.9, compared to the remaining images in the dataset. Figure 5.6 illustrates the affected images. The difference between the images shown and the remaining ones in the dataset is the appearance of the brain-stem (tail) structure on the lower part of the image. Registering an image with visu-

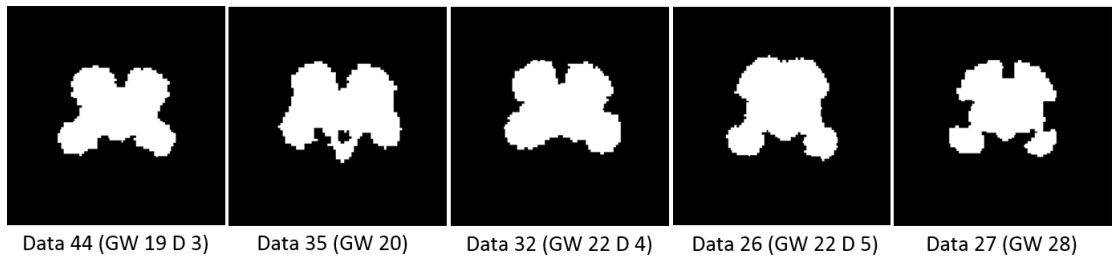


Figure 5.6: Illustration of images that achieve a more than three times lower DC than 0.9 in pairwise registration procedures.

alised brain-stem to a non visualised brain-stem structure, requires a different parametrisation of the smoothing of the velocity field, i.e. α , β and γ have to be adjusted for being able to model the brain-stem 'tail'.

5.4 Experiment 4: Analysis Regarding the Initialisation of Combination of Registration Procedures

The following research questions are answered in this experiment:

"Is it possible to pairwise register unmasked gray value fetal brain images and is there a difference if a brain or box mask is used? Is it possible to use the vector field that has been learned by registering gray value images to transform the corresponding binary source image or to initialize the registration procedure of binary images?"

The following parameter settings are used:

1. $N=30$, $\text{maxIter}=50$, $\sigma=0.09$, $\epsilon=0.0009$, $[\alpha, \beta, \gamma]=[0.5, 0, 1]$
2. $N=15$, $\text{maxIter}=50$, $\sigma=0.09$, $\epsilon=0.001$, $[\alpha, \beta, \gamma]=[0.5, 0, 1]$

In this experiment gray value images as well as the corresponding binary images are used. The images are rigidly aligned and scaled to a fixed cortical radius size of 60 pixels. In Figure 5.7 the result of the experiment is shown. Image No. 44 (GW 19 day 3) and image No. 9 (GW 26 day 4) with a GW difference of more than 5 weeks are used. First, the two gray value pictures $I0g$ and $I1g$ are loaded and a corresponding vector field is learned, using the parameter setting 1. The blue curve in Figure 5.7 illustrates the corresponding DC results over the iteration and the labelled image at iteration step 50. The vector field obtained acts as initialisation vector field for registering the corresponding binary images $I0s$ and $I1s$. This procedure is made to analyse the possibility to obtain a vector field for binary images computed from gray values. This approach is compared to a registration approach with binary images without computing an initialisation vector field using parameter setting 2. The red curve in Figure 5.7 shows the corresponding DC results over the iteration and the labeled image at iteration step 50. The DC of the gray value

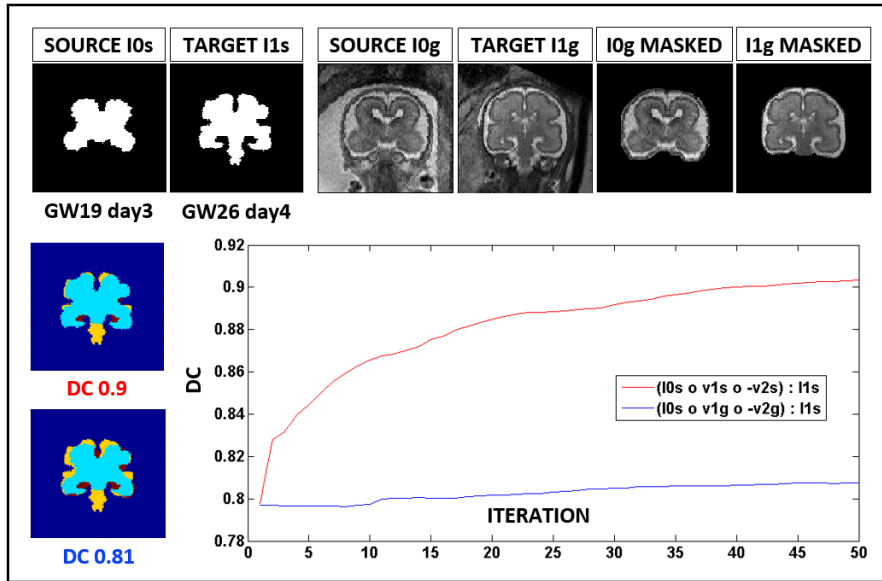


Figure 5.7: Vector field optimisation based on non masked gray value images ($I0g, I1g$), as initialisation for the registration of the corresponding binary scaled images ($I0s, I1s$). Picture 44 (GW 19 day 3) and 9 (GW 26 day 4) are used.

approach (blue curve) shows no significant DC differences over the iteration steps in comparison to the binary case (red curve). A reason for this result is the influence of the surrounding mother tissue on the registration. In a next step the mother tissue is excluded using a box and a brain mask to investigate its influence on the quality of registration. The results show that the optimised vector field based on masked gray value images is not able to transform the corresponding binary image to the binary target. The DC shows no value over 0.9 as well as the blue curve in Figure 5.7, also after excluding the surrounding tissue.

In the next part of the experiment, images containing all annotation labels instead of gray value images are used to learn an initialisation vector field to register the binary images. The images are rigidly aligned and scaled to a fixed cortical radius size of 60 pixels. In Figure 5.8 the registration results using annotations are shown. Top left image No. 31 (GW 18 day 0) and image No. 40 (GW 30 day 2) are illustrated. The corresponding DC results over the iteration are shown top right. On the bottom left image No. 39 (GW 30 day 0) and image No. 43 (GW 19 day 6) are presented. The corresponding DC results over the iteration are shown on the bottom right. The registration of a brain at GW higher than 30 on a brain at GW lower than 19 weeks and vice versa show in both cases that a DC between 0.85 and 0.9 is achievable, when initialising the registration of binary images with a vector field, learned on annotations. This is less than registering the binary images directly, which achieves a DC of 0.93.

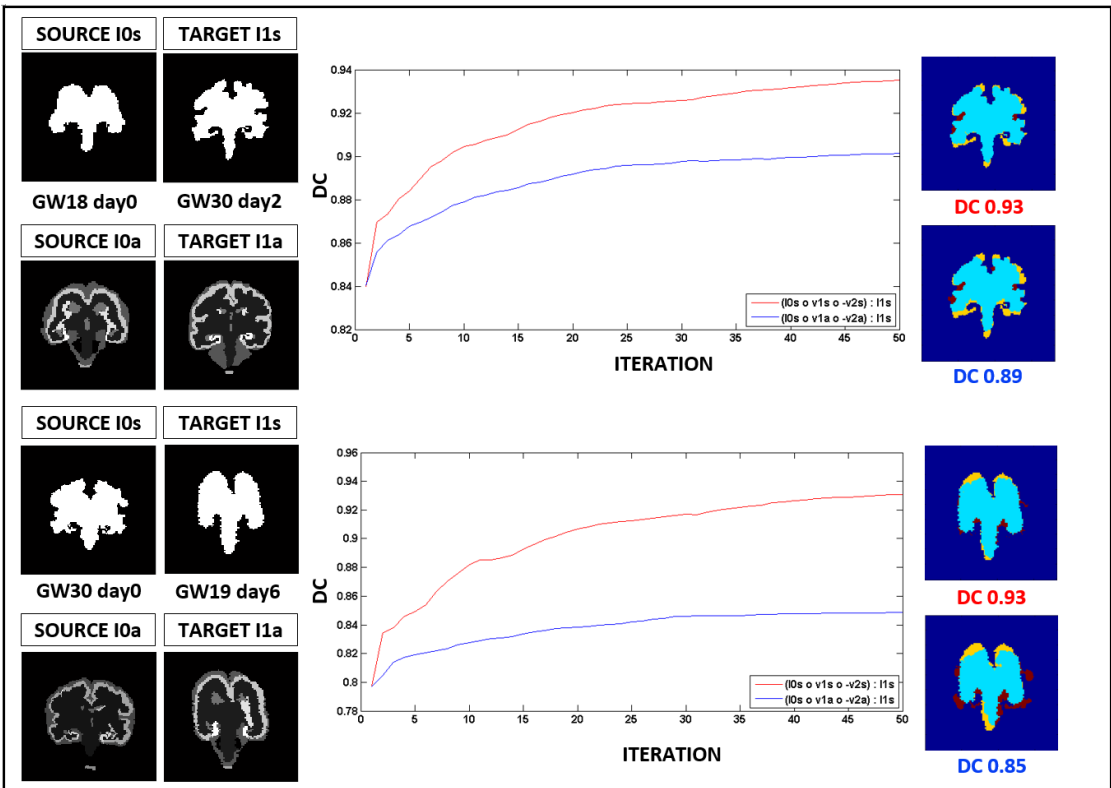


Figure 5.8: Vector field optimisation based on scaled image annotations as initialisation for the registration of the corresponding binary scaled images.

5.5 Summary

This chapter summarizes the preliminary experiments, which are performed to test the registration possibilities of fetal brains using a state-of-the-art diffeomorphic pairwise registration algorithm. Experiments regarding the composition of vector fields, the alignment, the dependence between registration results and GW differences of source and template image used and the initialisation of registration procedures are documented. The observed result leads to the conclusion that a composition of a forward and a backward transformation, which are estimated by registering source and target to an average image, can be used to map a source image to a template image directly. The experiments regarding the preprocessing show that for the diffeomorphic registration of fetal brain images rigid alignment (translation, rotation) and image masking is necessary, but the algorithm is able to model scaling transformations using a two step parametrisation procedure. The experimental results show that no relation between the DC and GW-difference of pairwise registered binary brain images is observable. The last group of experiments documented in this chapter shows that it is possible to use a vector field learned on gray-value images to initialise the registration procedure of binary images.

CHAPTER 6

Automatic Tissue Labeling Framework

This chapter gives an overview of the structure and functionality of the developed automatic tissue labeling framework which represents the solution to the following problem:

Is it possible to automatically compute cortex and ventricle segmentations of MR images of fetal brains between GW 18 and GW 30 using geodesic regression and graph cuts?

Figure 6.1 illustrates the proposed framework, which automatically segments ventricle and cortical tissue (OUTPUT) of a fetal brain MR volume (INPUT). First the input gray value image I_{new} at time point t_{new} is preprocessed. Subsequently, the longitudinal diffeomorphic fetal brain atlas (red) is used to estimate a time point corresponding diffeomorphic transformation for computing an time-dependent intensity image I_A and a time-dependent segmentation for ventricular and cortical tissue S_A^{tissue} in atlas space (red). In a pairwise registration procedure a transformation T from the new image I_{new} to the atlas-based intensity image I_A is estimated. The inverse of the computed transformation T^{-1} is used to transform the atlas based segmentations S_A^{tissue} to the subject's space ($S_A^{tissue} \circ T^{-1} = S_{GC}^{tissue}$). As next step the transformed segmentations S_{GC}^{tissue} (blue) and I_{new} are used as input parameters for the multi label graph cut segmentation refinement. The output of the framework are segmentations for ventricular and cortical brain tissues S_{new}^{tissue} of the input image I_{new} .

The MRI acquisition setup of the dataset used to learn the atlas is documented in Section 6.1. Based on the analysis of state-of-the-art approaches (cf. Chapter 2) and the results obtained of the preliminary experiments (cf. Chapter 5) a preprocessing pipeline for fetal brains is created and introduced in Section 6.2. The Atlas learning routine and corresponding analysis introducing three different registration schemes are explained in Section 6.3. The parametrisation of the graph cut approach and corresponding analysis are documented in Section 6.4. The same denotation introduced in Section 3.1 and 4.1 is used in this chapter.

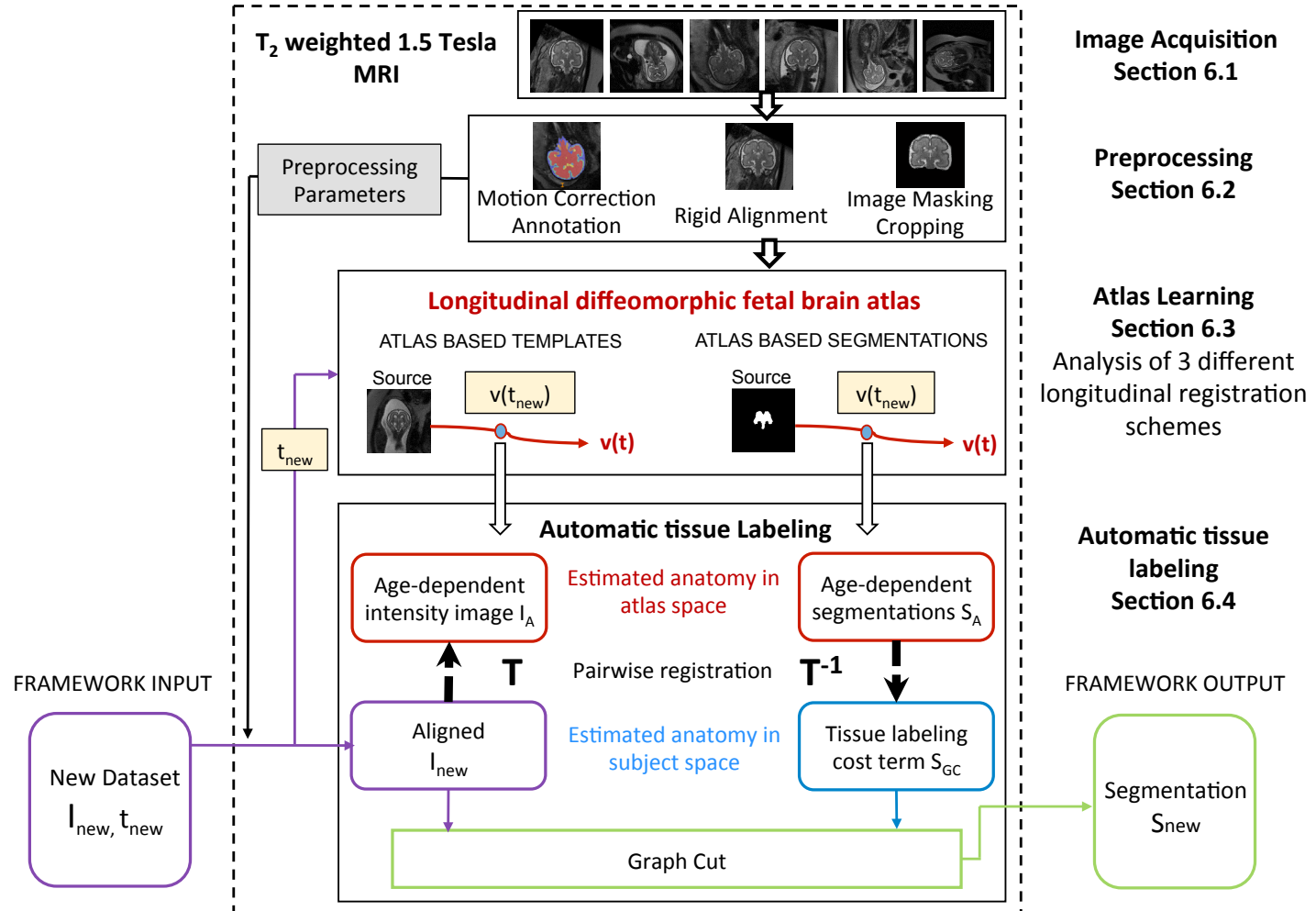


Figure 6.1: Fetal brain tissue labeling framework.

6.1 MRI Acquisition Setup

The proposed tissue labeling framework is evaluated using an image time series MRI dataset consisting of 46 healthy fetal brains. The gestational age lies between the 18th and 30th GW. The MR image acquisition is performed using an 1.5 Philips Gyroscan superconducting unit scanner performing a single-shot, fast spin-echo T2-weighted MR sequence. The corresponding setup is summarized in Table 6.1.

Table 6.1: Setup of the single-shot, fast spin-echo T2-weighted MRI sequence

Scanner	Philips Gyroscan superconducting unit, 1.5 Tesla
In-plane resolution	0.78-0.9 pixels per mm
Slice thickness	3-4.4mm
Acquisition matrix	256×256
Field of view	200-230mm
Specific Absorption Rate (SAR)	< 100%/4.0W/kg
Image acquisition time	≤ 20s, TE (Echo Time) 100-140ms, TR (Repetition Time) 9000-19000ms

Figure 6.2 shows examples of extracted 2D slices at different GWs of the dataset used (the abbreviation D stands for gestational days). The fetal brains in the slices are neither aligned according to a certain position nor rotated for obtaining the same orientation. Also the mother tissue is not excluded.

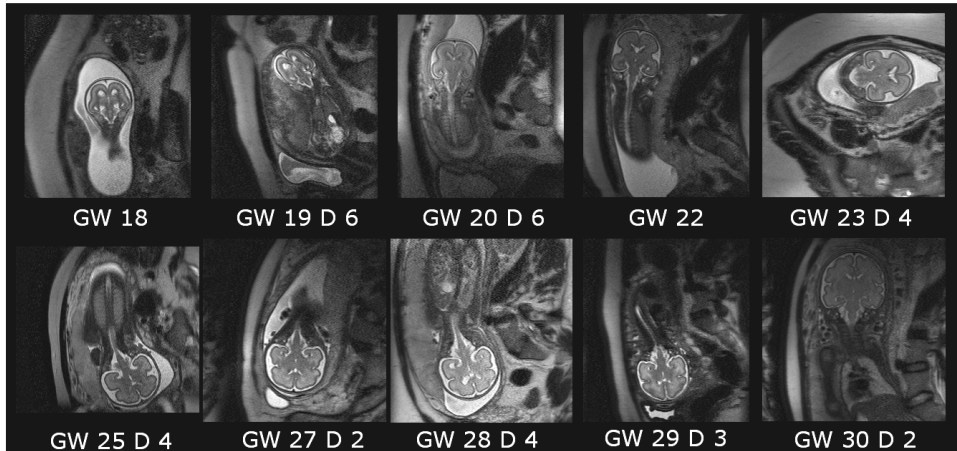


Figure 6.2: MRI slices of healthy fetuses between GW 18 and GW 30 GD 2 of the dataset for 2D analysis. MR images courtesy of Medical University of Vienna (MUW).

6.2 Preprocessing

For this master's thesis the atlas learning as well as the graph cut segmentation are analysed in 2D as well as in 3D.

The 2D image dataset used for analysing the behaviour of the diffeomorphic registration framework and geodesic regression algorithm is created by extracting slices at the same position of the MR 3D volumes of different healthy fetuses as well as at the corresponding annotations. For producing the required images (binary, gray value) for performing analysis in 2D, a Graphical User Interface (GUI) is programmed using MATLAB. With this application it is possible to load 2D annotation images as well as gray value images. In the annotation case also a binary image can be created. To this aim, the user chooses which structure (cortex, ventricle, both) should appear as foreground. With both image types it is possible to center, rotate and scale the fetal brains. By clicking on the button "New Selection" six points are selected. For rotating an image a rotation vector is needed, which is described by the first two selected points. They have to lie on an axis and are marked at the end of the brain stem and the deepest point of the IHF. Figure 6.3 illustrates the GUI of the preprocessing software. The last four points are marked in

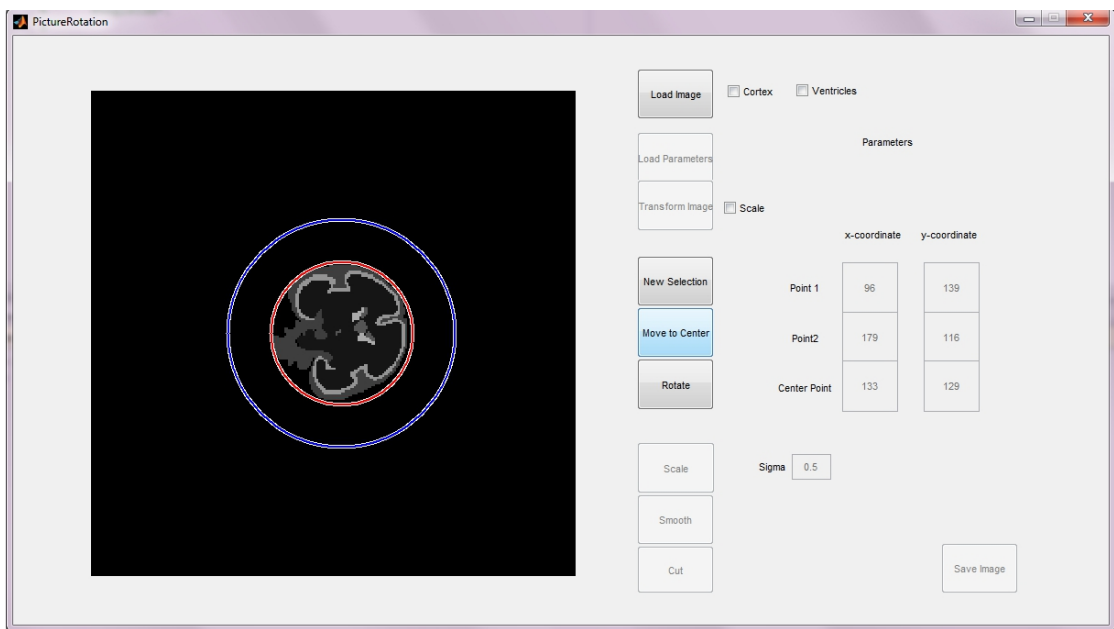


Figure 6.3: GUI of the preprocessing software. This screenshot shows a loaded annotated picture and two circles around the fetal brain (red...current size, blue...scaled size) which visualize the resize factor if the image is scaled.

a circular way around the brain. According to the selected positions, a circle around the fetal brain, its radius and its middle are estimated. In the centering procedure (started by the button "Move to Center") the image is shifted by moving the computed central point towards the middle pixel of the image. After pushing "Rotate" the picture is rotated through an angle which is

determined by the previously defined rotation axis around the middle of the image. For scaling an image, the estimated radius of the circle is used to resize all brains to a fixed radius size of 60 pixels. The button "Cut" cuts the preprocessed images to the fixed size 181×181 , by preserving the middle point position. The Gaussian smoothing operation is started by pressing "Smooth" and choosing a value for the σ parameter. An unsmoothed version of the picture is always kept in the background. The smoothed as well as the unsmoothed picture are stored by pushing "Save Image". For documentation issues and traceability of the preprocessing changes all preprocessing parameters are stored in a textfile. The user interface is able to load these files (Button "Load Parameters") and to transform and store images (Button "Transform Image") by the same protocol.

The acquired 3D MR images are preprocessed using the pipeline illustrated in Figure 6.4. First



Figure 6.4: Preprocessing pipeline for fetal brain MR volumes

the images are **motion corrected** using the toolkit for fetal brain MR images published by Rousseau et al. [60]. Subsequently the **annotation** of the following brain structures is manually performed by an expert in the dataset used: Cortex, left and right eye, ventricle and occipital foramen magnum. According to the analysis of the longitudinal registration algorithm used, **rigid alignment** of the volumes is required. Therefore, a triangle is assumed between the point where the skull ends (occipital foramen magnum (O)), the midpoint of the left (L) and the right eye sphere (R) (cf. Figure 6.5). Figure 6.6 illustrates the position of the triangle before and after

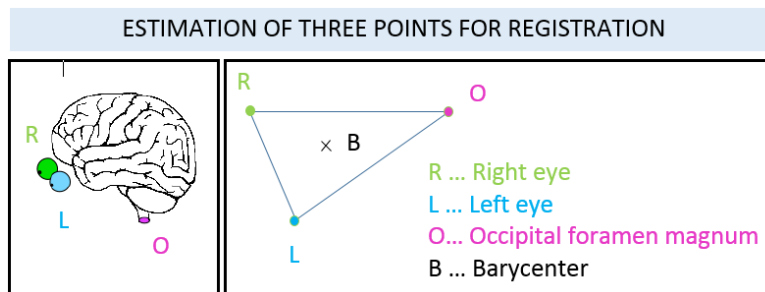


Figure 6.5: Three point estimation for rigid registration. Left image modified from [23].

the alignment procedure. For rigid alignment the barycenter (B) of the computed triangle and the corresponding normalvector (N) are calculated. Subsequently, the segmentations are translated,

so that the barycenter of the estimated triangle lies in the origin. For rigid alignment following

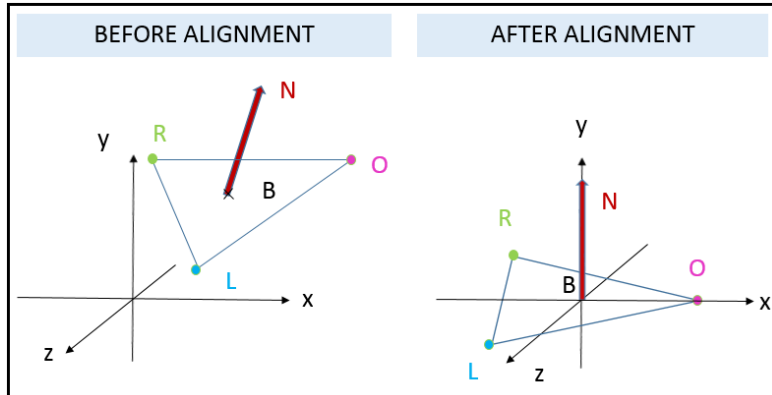


Figure 6.6: Rigid alignment using barycenter and corresponding normalvector, for estimating translation and rotation parameters.

constraints have to be satisfied after rotating the MR volumes: the normalvector coincides with the y-axis of the coordinate system and the point O has to lie on the x-axis (cf. Figure 6.6). The estimated alignment parameters of the segmentations are applied subsequently in the alignment procedure of the gray value volumes. After alignment, the surrounding mother tissue is excluded in a **masking** preprocessing step. For reducing computational costs in the longitudinal registration procedure **volume cropping** is performed, by transforming the aligned data to a uniform size of $90 \times 140 \times 140$ voxels. Therefore, a bounding box is computed, integrating all images in the dataset.

6.3 Learning a Continuous Model of Fetal Brain Development

For learning a continuous model of fetal brain development a longitudinal geodesic regression algorithm is analysed. This section starts with an introduction to the algorithm used and subsequently three different longitudinal registration schemes are presented and analysed in 2D. Corresponding analysis and evaluation results in 3D are presented in Chapter 7.

The Geodesic Image Regression Algorithm

The algorithm used for (DARTEL) Diffeomorphic Anatomical RegistratiOn using Exponential Lie algebra of Ashburner et al. [2] [1] for geodesic regression is integrated in the Statistical Parametric (SPM) tool box - release SPM8¹. In the course of this master's thesis it is modified with respect to the usage of brain images of fetuses. The longitudinal registration algorithm needs three input parameters to compute an optimised time-dependent velocity field: A normalised image dataset of N images sorted in ascending order by GA in days, an integer array t containing

¹<http://www.fil.ion.ucl.ac.uk/spm/>; [accessed 13-September-2015]

the GA in days of the corresponding images in ascending order and a set of parameters *options* (cf. Table 6.2). The algorithm initialises with a consistency check of input parameters and subsequently performs image regression using different voxel resolutions. The resolution levels are increased iteratively. The results of every resolution level are added as last computation part of this algorithm. For every resolution the following procedure is executed:

- Loading of current resolution information and resampling data to current resolution
- Calculation of the age range for the dataset, time span between images and greatest common divisor to obtain regular sampled time points, taking into account that all the data in the dataset are included. Estimation of amount of observed time points through the dataset (multiple represented time points are counted as one).
- Precomputation of K by Fast Fourier Transformation (FFT) of the kernel of deconvolution using function **spm-shoot-greens**. K acts at the derivation of velocity from momentum as smoothing operator.
- Computation of internal representation with functions **bspline**, **bsplins** that estimate an initial velocity field using B-splines.
- Gauss-Newton optimisation of v_0

Gauss-Newton Optimisation

The Gauss-Newton optimisation procedure requires as input parameter the dataset, the options and the parameters representing the internal representation. For every iteration step $iter = 1, \dots, numIter$, the cost function expressed in Equation 6.1 is minimized in the following procedure:

- Computation of the current forward deformation φ_{t_N} from source I_{t_0} to target I_{t_N} , its Jacobian determinant $|J_{t_N}|$ and tensor, gradient g^{iter} and Hessian H^{iter} , and the transformed image of the iteration step $I_{est}(t_N)$.
- Computation of the cost function E (cf. Equation 6.1) [2].

$$E^{iter} = \frac{1}{2} \|L^\dagger L v_0\|^2 + \frac{1}{2} \sum_{i=1}^N \left(\int_{x \in \Omega} \|I_{t_0} - I_{t_i}(\varphi_{t_i})\|^2 dx \right) \quad (6.1)$$

- If E^{iter} is worse than E^{iter-1} , then decrease ϵ , where ϵ represents a scaling parameter to prevent overshooting updates.
- Update of v_0 using Equation 6.2.

$$v_0^{iter+1} = v_0^{iter} - \epsilon(K^{-1} + H^{iter})^{-1}(K^{-1}v_0^{iter} + g^{iter}) \quad (6.2)$$

Computation of the time dependent deformation field φ_{t_N}

The time dependent deformation field φ_{t_N} is computed between the images representing the extremes of the gestational age range of the dataset (source I_{t_0} and target I_{t_N}) as illustrated in Figure 6.7. First the initial momentum m_0 is derived from the initial velocity field ($m_0 = K^{-1}v_0$)

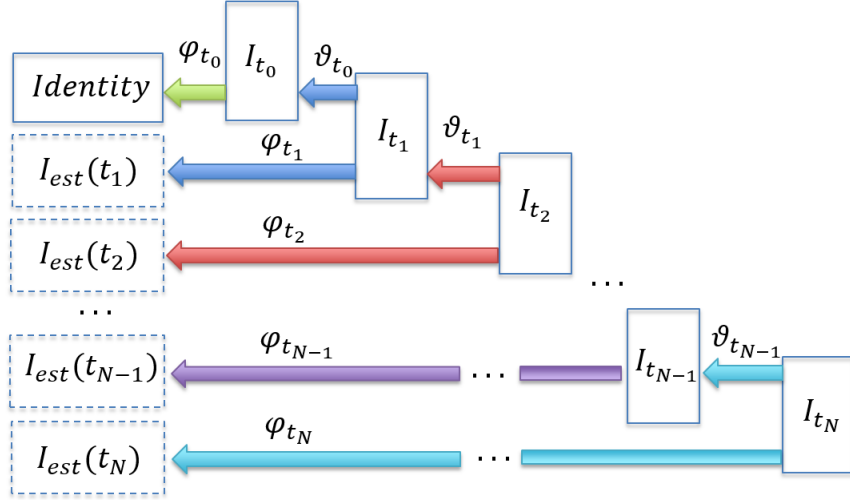


Figure 6.7: Schematic illustration of estimating the deformation φ_{t_N} , which maps the target I_{t_N} to the source I_{t_0} , considering N images I_{t_n} at time points t_n in the dataset, where $n=1,\dots,N$. φ_{t_n} and δ_{t_n} denote the forward and backward deformations of the image I_{t_n} at time point t_n . The forward transformed image $I_{est}(t_n)$ is denoted as $I_{est}(t_n)$.

and φ_{t_0} is set to the identity transformation. In a second step the forward transformation φ_{t_N} , which deforms the target image to $I_{est}(t_N)$, is computed: For every image n in the dataset a backward transformation $\delta_{t_{n-1}}$ is estimated. For computing the forward transformation φ_{t_n} from the current observed image I_{t_n} to the source I_{t_0} , the following composition is made: $\varphi_{t_n} = \varphi_{t_{n-1}} \circ \delta_{t_{n-1}}$. Subsequently, its Jacobian tensor and determinant are estimated to check if the diffeomorphic constraint is preserved. For calculating $I_{est}(t_n)$, the observed image I_{t_n} is deformed by the estimated forward deformation φ_{t_n} [2]. After the computation of the time-dependent vector field φ_{t_N} , the approximations of its gradient g and Hessian H are estimated.

Definition of Registration Options

For understanding the behaviour of longitudinal registration using geodesic regression, first the optimal parametrisation of the algorithm has to be estimated. Therefore, a short overview of the influence of the used parameters is given and illustrated in Table 6.2. The left column expresses the name of the parameter, the middle column the data type and in the right column a short description is given.

Table 6.2: Option parameters for the regression algorithm

Parameter	Data type	Explanation
M	Logical Matrix	Image mask
visu	Boolean	Visualization flag
numIter	Integer	Maximum number of iterations to perform
epsilon (ϵ)	Double	Gradient descent step size
voxSize	Integer array of size 1×3	Voxel size
ker _ type	Integer between 0 and 2	0: linear elastic, 1: membrane (Laplacian), 2: bending (biharmonic/thin plate)
ker _ args	Double array of size 1×5	Vector field regularisation parameters
fmg _ args	Integer array of size 1×3	Full Multi Grid (FMG) arguments: # integration steps, # cycles, # iterations
spl _ deg	Integer	Spline degrees
wrapDim	Boolean array of size 1×3	Wrapping on/off in x/y/z direction
maxStepLen	Integer	Minimal temporal resolution
mc	Integer	Multichannel flag to discriminate between 3D and 2D multichannel
v0	Double matrix	Previously computed vector field for initialising a warm-starting registration
Tolit	Double	Return if change in energy is smaller than 'minChange'*100
mineps (ϵ_{min})	Double	Minimum optimization step
maxeps (ϵ_{max})	Double	Maximum optimization step
pltSl	Boolean	Which slice to plot, necessary if 3D images are used, in 2D pltSl=1
nRes	Integer	Number of resolution levels
solver	Boolean	Which solver to use. 0: DARTEL, 1: MATLAB
optimizer	Integer between 0 and 2	Which optimizer to use. 0: Gauss-Newton, 1: Hamiltonian Markov Chain, 2: Stochastic Newton (Markov Chain Monte Carlo (MCMC))

Parameters epsilon (ϵ), epsmin (ϵ_{min}) and epsmax (ϵ_{max})

The parameter ϵ influences the speed of convergence and the stability of the algorithm. The minimizing of the ϵ parameter (**gradient descent step size**) leads to a faster convergence, but the stability of the algorithm decreases [1]. Additionally, the **minimum and maximum optimization step** ($\epsilon_{min}, \epsilon_{max}$) are defined for being able to weight the optimisation result of an iteration. The weighting parameters change depending on the result of the computed cost function and lie in the defined range between ϵ_{min} and ϵ_{max} .

Parameter wrapDim

The parameter **wrapDim** handles the boundary condition and influences the wrapping of functions around the boundary, i.e. a disappearing point on the left side appears again on the right side of the image [1].

Parameters ker_type, ker_args and voxSize

The velocity field $u(x)$ at position x is parametrised using a linear combination of i basis functions. Such basis functions consist of a vector of coefficients c_i and a i^{th} first degree B-spline basis function $\rho_i(x)$ (cf. Equation 6.3) [1].

$$u(x) = \sum_i c_i \rho_i(x) \quad (6.3)$$

Aim of the DARTEL implementation is to estimate an optimized parameterisation of c . The energy cost term E in Equation 6.1 is reformulated in terms of finding the coefficients of c for a given dataset D with maximum probability (cf. Equation 6.4). A maximization of the probability leads to the minimization of its negative logarithm and thus, is used to interpret registration of data D as a minimization procedure of the objective function E . It consists of a prior term $E_1(c)$ and a likelihood term $E_2(c)$ and is expressed in Equation 6.5 [1].

$$E(v) = E_1(c) + E_2(c) \quad (6.4)$$

$$-\log p(c, D) = -\log p(c) - \log p(D|c) \quad (6.5)$$

- **Prior term ($-\log p(c)$)**

The prior term denotes the prior probability $p(c)$. In this approach an inverse of a covariance matrix K is used to encode the variability in all spatial locations. Three different models for K are implemented. The models differ in influencing the deformations and how they interpolate between features in the images. With the parameter **ker_type** a linear elastic model, a membrane energy model (Laplacian model) or a bending energy model (biharmonic, thin plate) are chooseable. The chosen model is regularized by the parameter **ker_args** $[\lambda_1, \lambda_2, \lambda_0, \mu, \lambda]$ and influences the bending energy, stretching, sharing (not rotation) as well the divergence and amount of volumetric expansion or contraction [1].

- λ_0 encodes the penalisation of absolute displacements.
- λ_1 penalises the difference between two neighboured vectors by observing the first derivatives (linear term) of the displacements.
- λ_2 penalises the difference between the first derivatives of two neighboured vectors by observing the second derivatives of the displacements.
- λ denotes the variability of the spatial locations (divergence of each point in the flow field) with a constant value. Increasing λ leads to increasing smoothing of the flow vector field and preserves volumes during the transformation.
- μ encodes the variance according to symmetric components, rotations and the penalisation of scaling and shearing.

The parameter **voxSize** [$\delta_1 \delta_2 \delta_3$] represents the height, width and depth of a voxel and has to be defined as well.

- **Likelihood term** ($-\log p(D|c)$)

The likelihood term encodes the probability of c given the data D [1]. It represents the implementation of a mean-squared difference measure between a warped template deformed by the calculated transformation and the target image (cf. Equation 6.6).

$$E_2 = \frac{1}{2} \sum_{i=1}^N \left(\int_{x \in \Omega} \|I_{t_0} - I_{t_i}(\varphi_{t_i})\|^2 dx \right) \quad (6.6)$$

Parametrisation of the Full Multi Grid (fmg_args)

A Full Multi Grid (FMG) approach is used to solve the equation (cf. Equation 6.2) which is needed to update the vector field during its optimising procedure. Therefore, the images are observed in different scales. For every resolution level multigrid methods recursively estimate the field, starting at the coarsest scale and computing the residual to solve the update equations on the current grid. Subsequently, the solution is prolongated to the next finer grid [1].

Longitudinal Registration Experiments using Geodesic Regression

The challenge of longitudinal registration of fetal brains lies in finding a suitable regularisation of the time dependent vector field to model the increasing cortical folding between GW 25 and 30 [80] and the changes in brain size. In the scope of this master's thesis, an initialisation procedure for computing time-dependent vector fields and three different longitudinal registration schemes are created and analysed. The DC is calculated using the manual brain structure segmentation of the gray value input image and the corresponding estimated atlas-based segmentation at the same gestational age. Table 6.3 shows the eight different regularisation kernels used for analysing the regularisation of longitudinal registration.

Table 6.3: Parametrisation of the kernels No.1-8 used for analysing the regularisation of longitudinal registration.

Kernel No.	λ_1	λ_2	λ_0	λ	μ
1	0.01	0.01	$9e^{-6}$	$1e^{-5}$	$1e^{-5}$
2	$9e^{-6}$	$9e^{-6}$	$9e^{-6}$	0.01	$1e^{-5}$
3	$1e^{-3}$	$9e^{-6}$	$9e^{-6}$	$1e^{-3}$	$1e^{-5}$
4	0.01	$9e^{-6}$	$9e^{-6}$	0.01	$1e^{-5}$
5	$9e^{-6}$	$1e^{-5}$	$9e^{-6}$	$1e^{-5}$	$1e^{-5}$
6	$9e^{-6}$	0.01	$9e^{-6}$	0.01	$1e^{-5}$
7	0.01	0.01	$9e^{-6}$	0.01	$1e^{-5}$
8	$1e^{-4}$	$1e^{-4}$	$9e^{-6}$	$1e^{-5}$	$1e^{-5}$

Longitudinal Registration Scheme 1

The first longitudinal registration scheme observes the longitudinal registration behaviour using a cascade procedure to estimate an initial vector field. The precomputed velocity field is parametrised by the amount of initialisation levels used. Figure 6.8 illustrates the analysed initialisation cascade. Every level $l = 1 \dots N$ uses gray value data at the extremes of the age range (t_0 : GW 18 and t_1 : GW 30 day 2) and at $\frac{x}{2^N}$ regular sampled time points, where $x = 1, \dots, (2^N - 1)$. The resulting time dependent vector field of a level is used to initialise

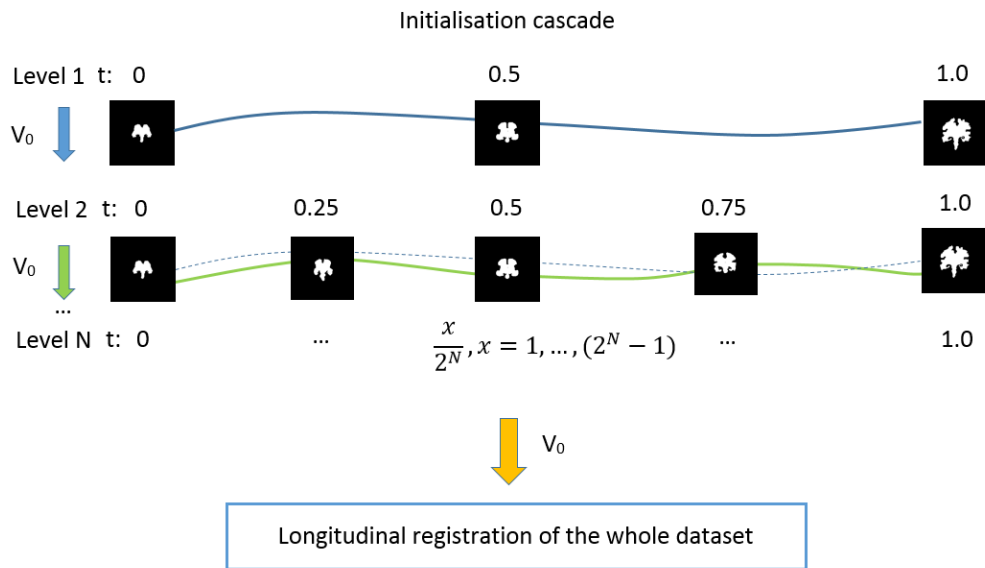


Figure 6.8: Illustration of the initialisation cascade to estimate an initial time-dependent velocity vector field for longitudinal registration of the whole dataset.

the next higher level or at the n^{th} level, the whole registration of the dataset. The initialisation cascade procedure uses an unique option parameter set for all N levels and the longitudinal registration of the whole dataset:

Parameter setting: solver=0 (Gauss-Newton), numIter=50, TolIt = 0.001, nRes=6, epsilon= $4e^{-5}$, minEps= $8e^{-3}$, maxEps=0.4, maxStepLen = 1, ker_type=0 (linear elastic model), spl_deg=[6 6 6], wrapDim=[0 0 0], voxSize=[1 1 1], fmg_arg=[15 5 5], multichannel=0.

Number of cascade levels analysed: 2 and 5

Results: In Figure 6.9, 6.10, 6.11 and 6.12 on the right side the DC distribution over the gestational age of five cascade levels and of the whole dataset (with and without initialisation) is illustrated for all eight kernels. The aim of this experiment is to identify if there is an improvement of DC using an initialisation cascade for longitudinally registering the whole dataset compared to using no precomputed vector field. The analysis of the influence of kernels 3, 5

and 8 show an increase of DC about 0.01 to 0.03 for gestational ages higher than GD 190 (GW 28 day 3) using initialisation procedure (cyan line) instead of no initialisation (black line). The remaining kernels show no significant difference regardless of using an initialisation scheme or not. Subsequently, according to an increased DC in the lower cascade initialisation level 2 (green dotted line), the longitudinal registration procedure was analysed using only 2 cascade levels. The corresponding results are shown in Figure 6.9, 6.10, 6.11 and 6.12 on the left side and illustrate the DC distribution over the gestational age of the two cascade levels and the whole dataset (with and without initialisation) for all eight kernels. Only kernel 8 shows a higher rising of DC about 0.03, compared to the usage of 5 levels at ages older than GD 190 (GW 28 day 3). In contrast to this, kernel 5 shows a decrease of the DC for ages older than GD 190 (GW 28 day 3) using cascade initialisation. According to the results of the registration scheme 1, it is concluded that longitudinal registration using only 3-5 images at regular sampled time points instead of the whole dataset lead to a higher DC compared to the registration of the whole dataset (with or without initialisation). Therefore, the registration kernel has to be chosen carefully to achieve a stable registration with a DC over 0.6 (e.g. results kernel 5, Figure 6.11).

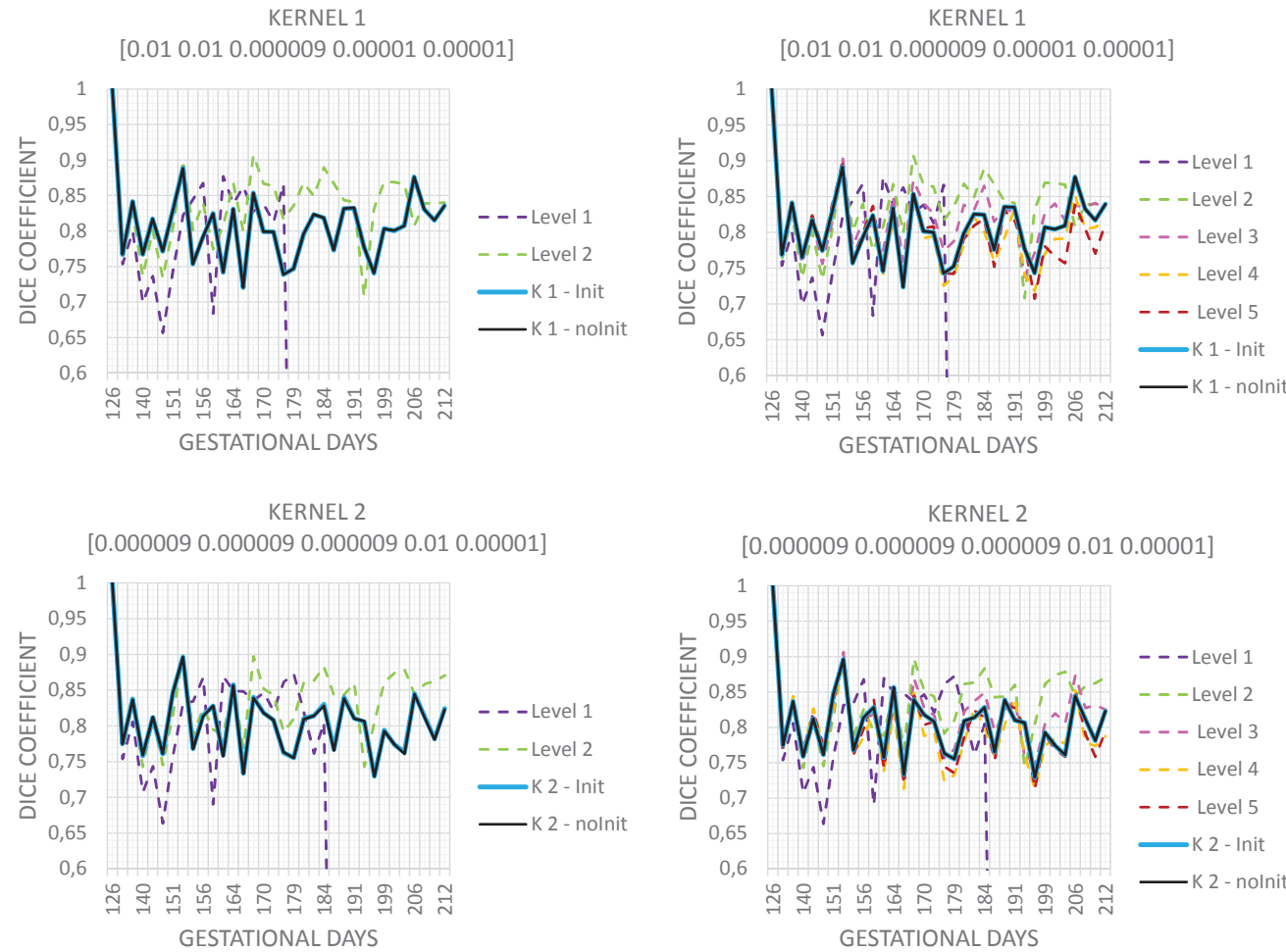
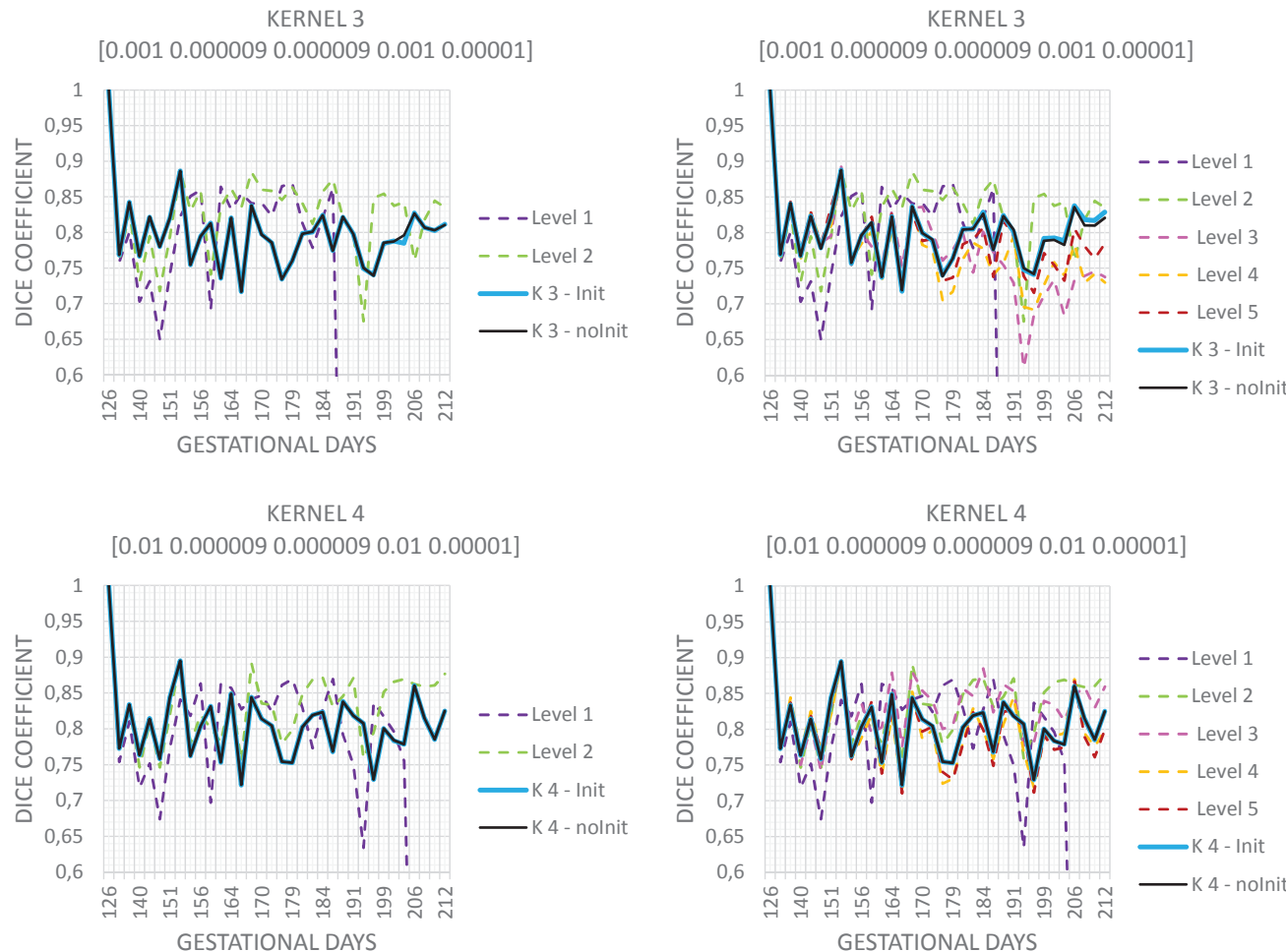


Figure 6.9: Scheme 1 DC distribution over gestational ages of the initialisation procedure using regularisation kernel 1 and kernel 2. Cascade level 1 is marked in green, level 2 in purple, level 3 in magenta, level 4 in orange, level 5 in dark red, the registration of the whole dataset with cascade initialisation in cyan and without initialisation in black.



17

Figure 6.10: Scheme 1 DC distribution over gestational ages of the initialisation procedure using regularisation kernel 3 and kernel 4. Cascade level 1 is marked in green, level 2 in purple, level 3 in magenta, level 4 in orange, level 5 in dark red, the registration of the whole dataset with cascade initialisation in cyan and without initialisation in black.

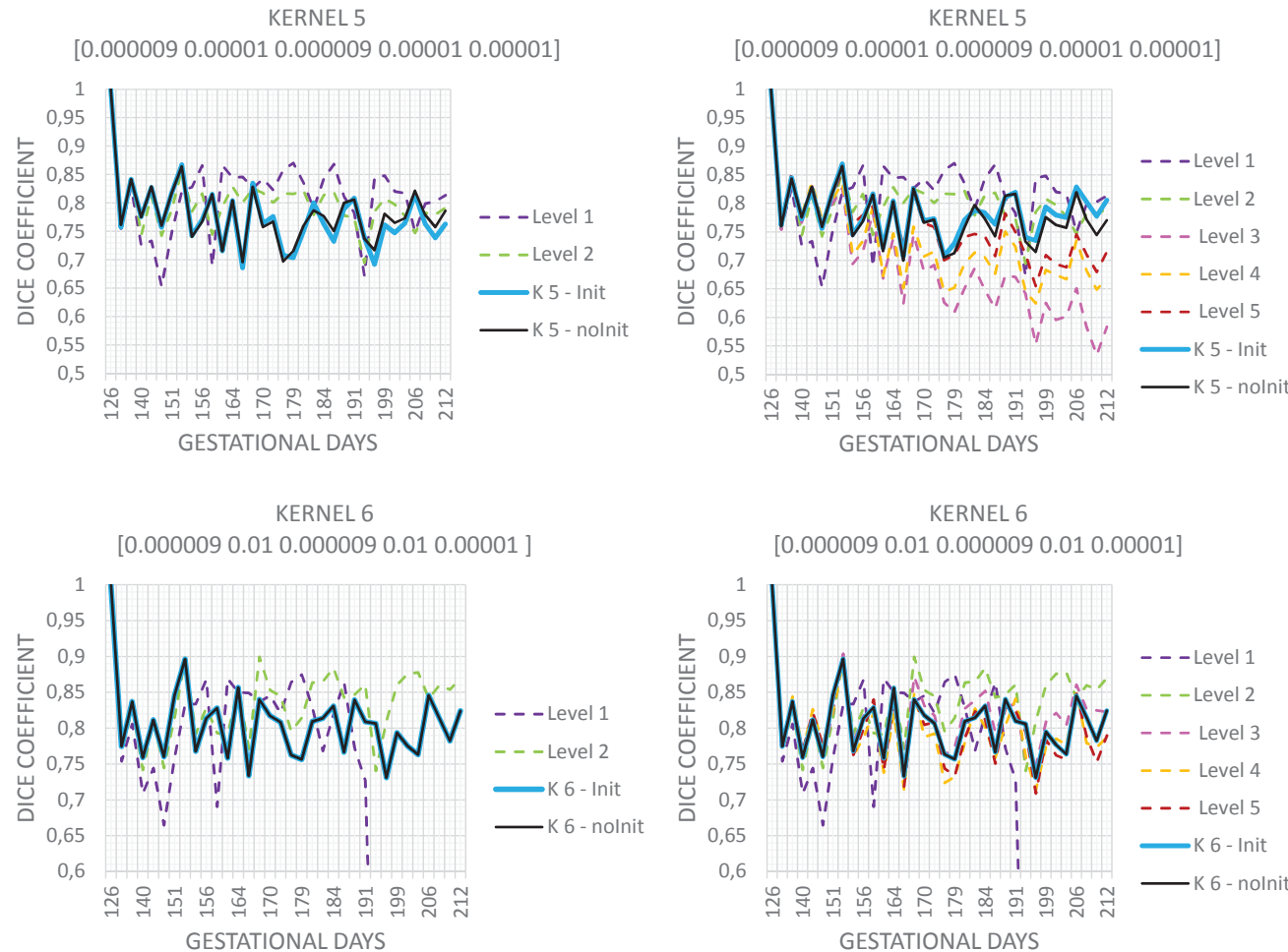


Figure 6.11: Scheme 1 DC distribution over gestational ages of the initialisation procedure using regularisation kernel 5 and kernel 6. Cascade level 1 is marked in green, level 2 in purple, level 3 in magenta, level 4 in orange, level 5 in dark red, the registration of the whole dataset with cascade initialisation in cyan and without initialisation in black.

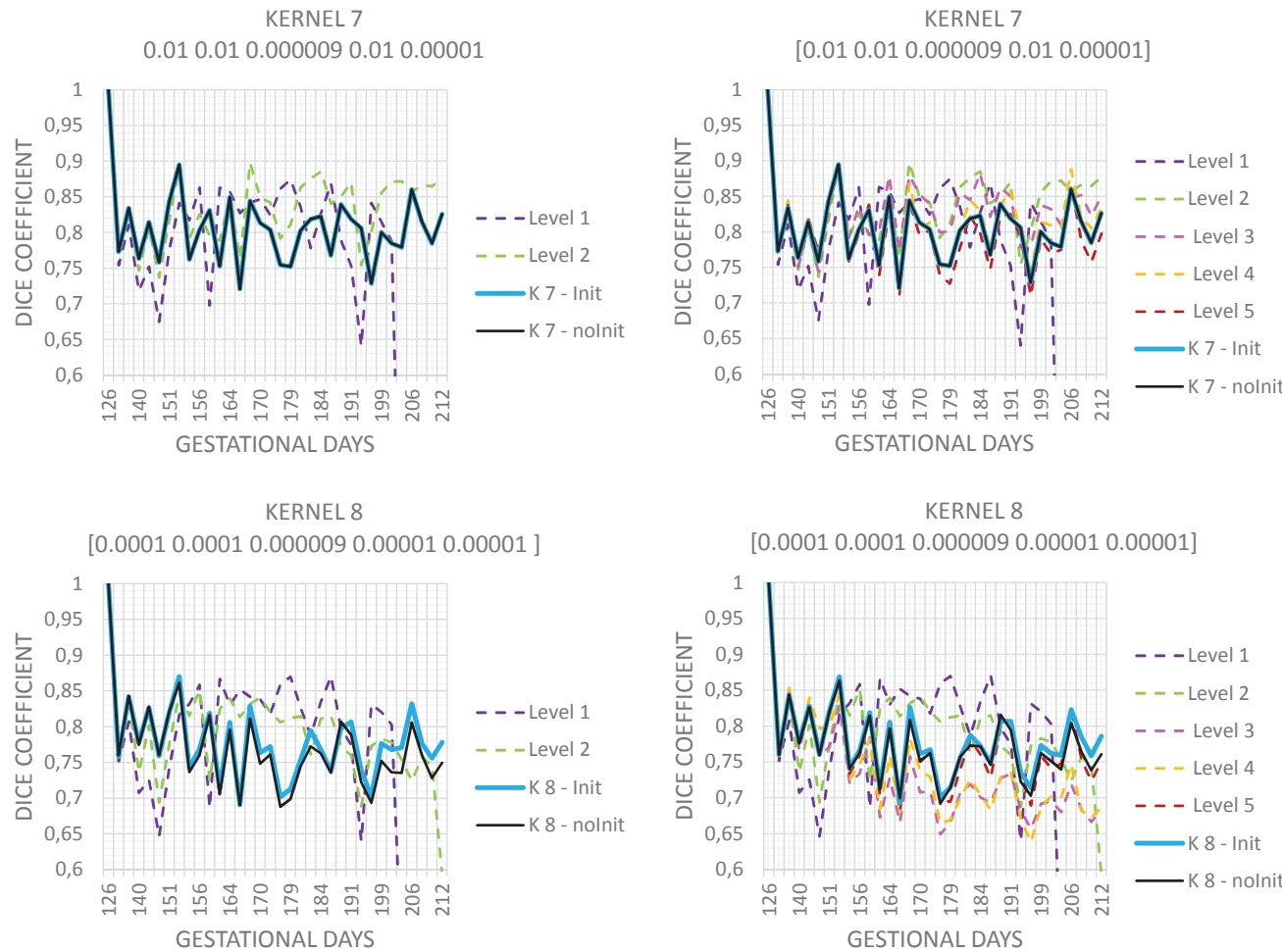


Figure 6.12: Scheme 1 DC distribution over gestational ages of the initialisation procedure using regularisation kernel 7 and kernel 8. Cascade level 1 is marked in green, level 2 in purple, level 3 in magenta, level 4 in orange, level 5 in dark red, the registration of the whole dataset with cascade initialisation in cyan and without initialisation in black.

Longitudinal Registration Scheme 2

In the second longitudinal registration scheme the whole dataset is longitudinally registered three times, using a different parametrisation of the regularisation kernel for every run. For the second and the third run the resulting velocity field of the previous run is used as initialisation. This procedure is illustrated in Figure 6.13.

Parameter setting run 1: $M = []$, solver=0 (Gauss-Newton), numIter=40, TolIt = $1e^{-3}$, nRes=6, epsilon= $4e^{-5}$, minEps= $8e^{-3}$, maxEps=0.4, maxStepLen = 1, ker_type=0 (linear elastic model), spl_deg=[6 6 6], wrapDim=[0 0 0], voxSize=[1 1 1], fmg_arg=[15 5 5], multichannel=0.

Parameter setting run 2: $M = []$, solver=0 (Gauss-Newton), numIter=35, TolIt = $1e^{-3}$, nRes=6, epsilon= $4e^{-5}$, minEps= $8e^{-3}$, maxEps=0.4, maxStepLen = 1, ker_type=0 (linear elastic model), spl_deg=[6 6 6], wrapDim=[0 0 0], voxSize=[1 1 1], fmg_arg=[15 5 5], multichannel=0.

Parameter setting run 3: $M = []$, solver=0 (Gauss-Newton), numIter=60, TolIt = $1e^{-3}$, nRes=7, epsilon= $4e^{-5}$, minEps= $8e^{-3}$, maxEps=0.4, maxStepLen = 1, ker_type=0 (linear elastic model), spl_deg=[6 6 6], wrapDim=[0 0 0], voxSize=[1 1 1], fmg_arg=[15 5 5], multichannel=0.

Results: At the top of Figure 6.14, the result of the registration scheme 2 is illustrated, us-

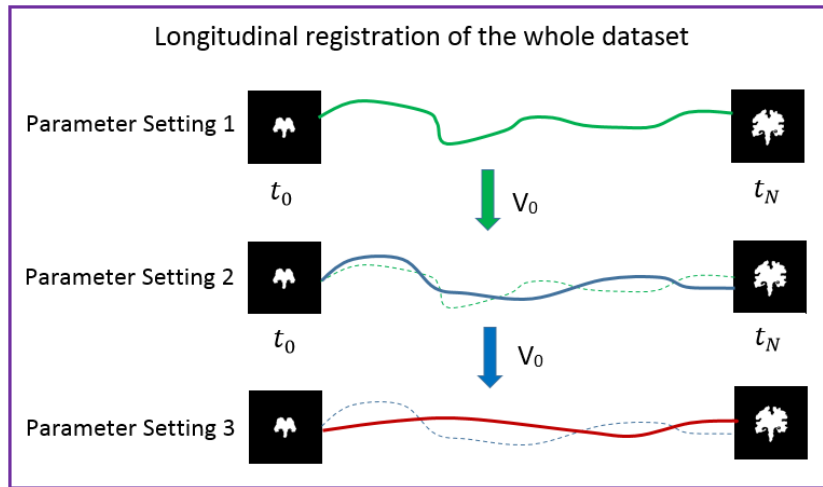


Figure 6.13: Scheme 2 longitudinal registration procedure

ing kernel 3 in the first run, kernel 7 in the second run and kernel 2 in the third run. In the middle of Figure 6.14 the result of the registration scheme 2 is shown, using kernel 8 in the first run, kernel 1 in the second and kernel 3 in the third run. The bottom part of Figure 6.14 presents the results of the registration scheme 2, applying kernel 1 in the first run, kernel 8 in the second and kernel 7 in the third run. Using registration scheme 2 and kernels 3, 7, 2 an increase of the DC between the first and third run of 0.02 from GD 146 to 164 and 0.04 from GD 168 to 197 (GW 24 - 28 day 1) is achievable. Also the usage of kernels 8, 2, 3 and 1, 8, 7 leads to an increase

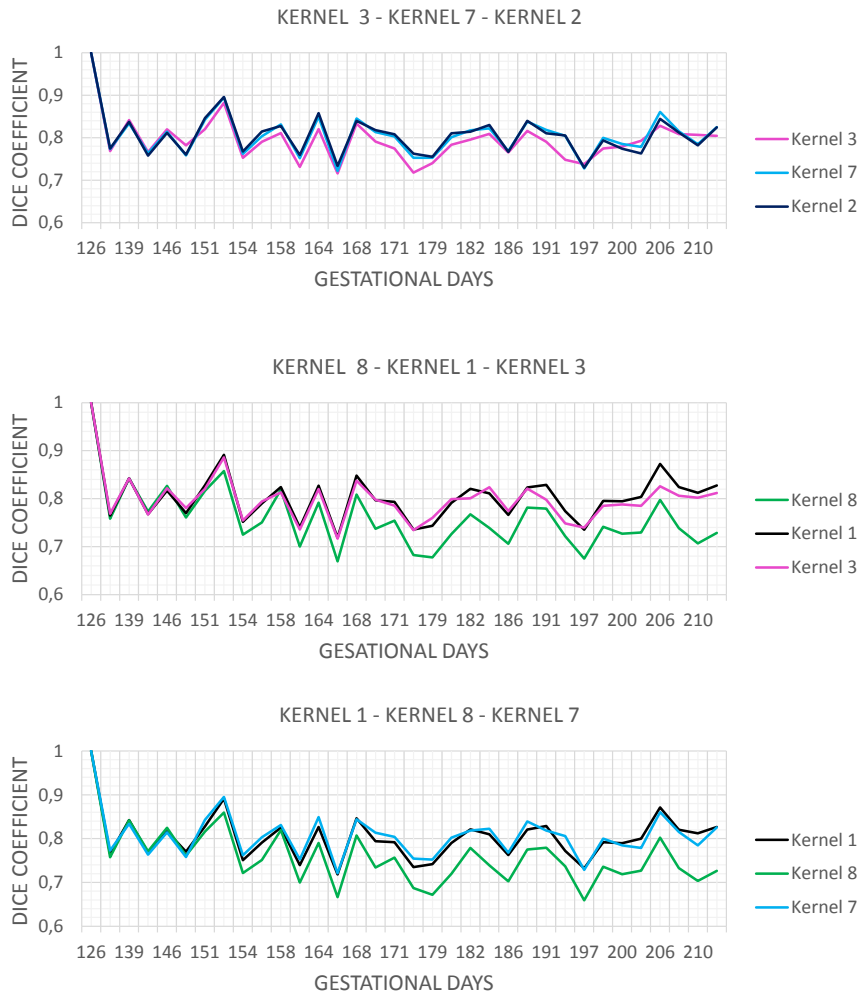


Figure 6.14: DC distribution of longitudinal registration using scheme 2.

of the DC of 0.03 between GD 151 to 168 (GW 21 day 1 to 24) and of 0.06 from GD 168 to 212 (GW24 to 30 day 2) between run 1 and 3. In all cases no increase of the DC is observed between the GD range from 126 to 146 (GW 18 to 20 day 6). This leads to the conclusion that an increase of the DC is achievable by using scheme 2, but depends on the parametrisation of the kernels and order of usage in the registration procedure. Additionally, it is observed that the increasing amount of the DC is dependent on the age range in all three analysed cases.

Longitudinal Registration Scheme 3

For the third longitudinal registration scheme three different age ranges are defined:

- age range 1: GD 126 (GW 18 day 0) - GD 160 (GW 22 day 6)

- age range 2: GD 160 (GW 22 day 6) - GD 180 (GW 25 day 5)
- age range 3: GD 180 (GW 25 day 5) - GD 212 (GW 30 day 2)

For every age range a dataset is used which contains images of gestational ages in the covered time period. Eight different regularisation kernels (Kernel 1 - Kernel 8 cf. Section 6.3) and the following **parameter setting** for every age range is used:

$\text{epsilon}=4e^{-5}$, $\text{maxEps}=4e^{-3}$, $\text{minEps}=0.4$, $\text{maxStepLen}=1$, $\text{voxSize}=[1\ 1\ 1]$,
 $\text{fmg_arg}=[15\ 5\ 5]$, $\text{spl_deg}=[6\ 6\ 6]$, $\text{ker_type}=0$ (linear elastic model), $\text{solver}=0$ (Gauss-Newton),
 $\text{TolIt}=1e^{-3}$, $\text{nRes}=6$, $\text{multichannel}=0$, $\text{wrapDim}=[0\ 0\ 0]$.

Results: Figure 6.15 illustrates the DC distribution over the gestation ages for age range 1 to 3. The results of age range 2 show a higher kernel depending DC deviation compared to the other age ranges, due to accelerated cortical folding and brain growth starting at GD 172 (GW 24 day 3). It illustrates the dependence of the brain growth modelling on the used regularisation kernel, where kernel 7 leads to the highest DC of 0.85 from GD 165 to 180 (GW 23 day 4 to 25 day 5) and kernel 3 to the lowest DC of 0.15. Regularisation kernels (6, 7, 2) with low λ_1 values between $9e^{-6}$ and $1e^{-5}$ and high λ values of 0.01, lead to higher DC compared to other kernels. According to this fact, it is concluded that higher penalisation of the difference between two neighboured vectors (λ_1) and a higher smoothness of the vector field (λ) lead to the improved modelling of the brain growth at every observed age range.

Conclusion Longitudinal Registration Schemes

The analysis of the three registration schemes shows that registration scheme 3 has the highest deviation between DCs using different regularisation kernels, since developmental dependent age ranges are defined. It makes it possible to parametrise the vector field regularisation according to the developmental stage of the fetus and thus is chosen as longitudinal registration procedure to learn a fetal brain atlas.

6.4 Automatic Tissue Labeling using Graph Cuts

For the 2D analysis of the CMF based graph cut the algorithm proposed by Yuan et al. [82] is taken. They use a CMF and convex formulation of the Potts model and a CUDA² based implementation for segmenting volumes. Table 6.4 shows the input parameters for running this algorithm. For analysing the preprocessing of atlas based segmentations three longitudinal atlases of three different age ranges are learned using the geodesic regression algorithm [1]. For computing the atlases the parameter setup of registration scheme 3 (cf. Section 6.3) and regularisation kernel 7 is used. For tissue labeling using a graph cut three input parameters are necessary. A data term, a cost (unary) term, and a penalty (binary) term.

²CUDA: NVIDIA architecture for parallel computing <http://www.nvidia.co.uk/object/cuda-parallel-computing-uk.html>; [accessed 13-September-2015]

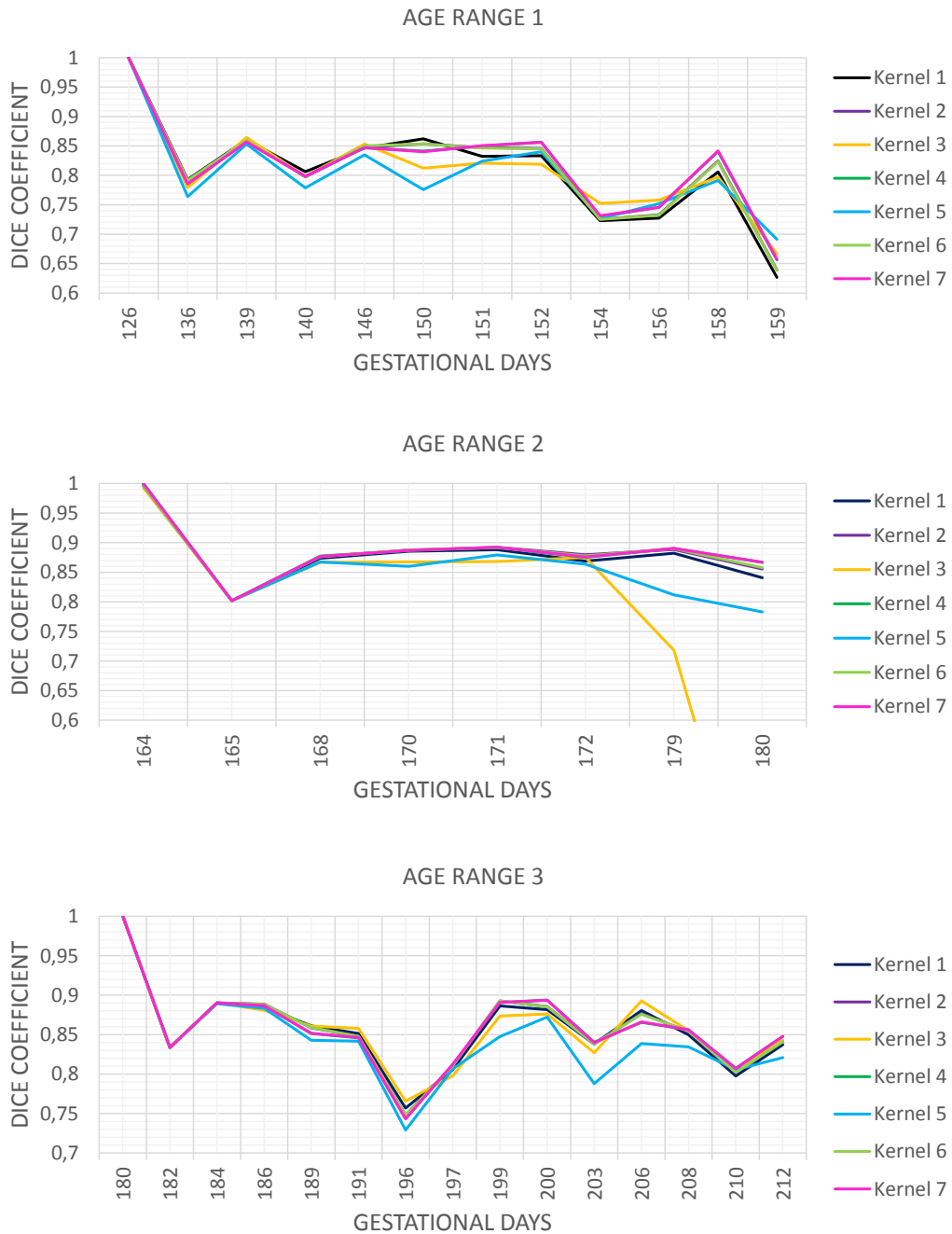


Figure 6.15: DC distribution over the gestational ages of the analysis of the longitudinal registration scheme 3

Table 6.4: Option parameters of the graph cut algorithm of Yuan et al. [82]

Option	Data type	Explanation
rows	Integer	Rows of the input image
cols	Integer	Columns of the image
maxIter	Integer	Maximum number of iterations
nlab	Integer	Total number of labels
errorBound	Double	Error bound for convergence
cc	Double	Step-size of augmented Lagrangian method
stepSize	Double	Step-size for the gradient-projection of the spatial flow fields
ulab	Double	Label corresponding values

- **Data (D):** Gray value volume at age t
- **Cost term (C):** For computing an unary term for the graph cut approach, atlas based segmentations for cortex and ventricle tissue $S_{tissue} = \{S_{cortex}, S_{ventricle}\}$ at age t are estimated and smoothed with a Gaussian filter K_G . The parameter δ is defined to weight the smoothed result with a constant factor. The unary term is illustrated in Equation 6.7, where $*$ denotes the convolution operator.

$$C = \delta * (S_{tissue} * K_G) \quad (6.7)$$

- Penalty term: In the course of the graph cut analysis three different binary terms are evaluated:
 - **Penalty term 1 (P_1)** is a weighted norm of the data term’s D gradient (cf. Equation 6.8), where δ denotes the same weighting term as used for the cost term and a, b are constant weighting parameters.

$$P_1 = \delta * \frac{b}{1 + (a * \|\nabla D\|)} \quad (6.8)$$

- **Penalty term 2 (P_2)** denotes a gray value based term and is calculated separately for cortex and ventricle segmentation (cf. Equation 6.9). Tissue type corresponding gray values are modelled as Gaussian distributions, which parameters μ_{tissue} and σ_{tissue} are estimated using the a-priori atlas segmentation. These parameters are used to calculate the probability of every pixel belonging to cortex or ventricle. Subsequently, the gradient of the resulting probability map P and its norm are computed and weighted by the parameters δ, a, b as shown in Equation 6.8.

$$P_2 = \delta * \frac{b}{1 + (a * \|\nabla P(\mu_{tissue}, \sigma_{tissue})\|)} \quad (6.9)$$

- **Penalty term 3 (P_3)** represents an exponential formulation and is expressed in Equation 6.10. u is a constant and v a linear weighting parameter. w weights the norm of the image’s D gradient non-linearly in the exponential term.

$$P_3 = u + v * \exp\left(-\frac{\|\nabla D\|}{w}\right) \quad (6.10)$$

Graph Cut Parameter Setting: $\epsilon=1.25$, $a=50$, $b=1$, $u=0.9$, $v=0.1$, $w=0.05$, $\text{maxIter}=200$, $nlab=3$, $\text{errorBound}=1e^{-3}$, $cc=1.0$, $\text{stepSize}=9e^{-3}$, $\text{ulab}(\text{background})=0$, $\text{ulab}(\text{brain})=1$, $\text{ulab}(\text{vent})=2$.

Pairwise Registration Setting: For pairwise registration two different parameter sets are used for cortex and ventricles. For cortex regularisation kernel 1 and for ventricles regularisation kernel 2 is used.

Results Graph Cut Analysis

Figure 6.16 illustrates the DC distribution of segmentations of the cortex and ventricles at age range 1. The red line represents the DC of atlas based segmentations, the blue line the DC of transformed segmentations using pairwise registration, the dotted light green, dark green and purple line the DC of graph cut based segmentations computed using penalty terms 1, 2 and 3. For both ventricle and cortex labeling a DC improvement between atlas based and graph cut

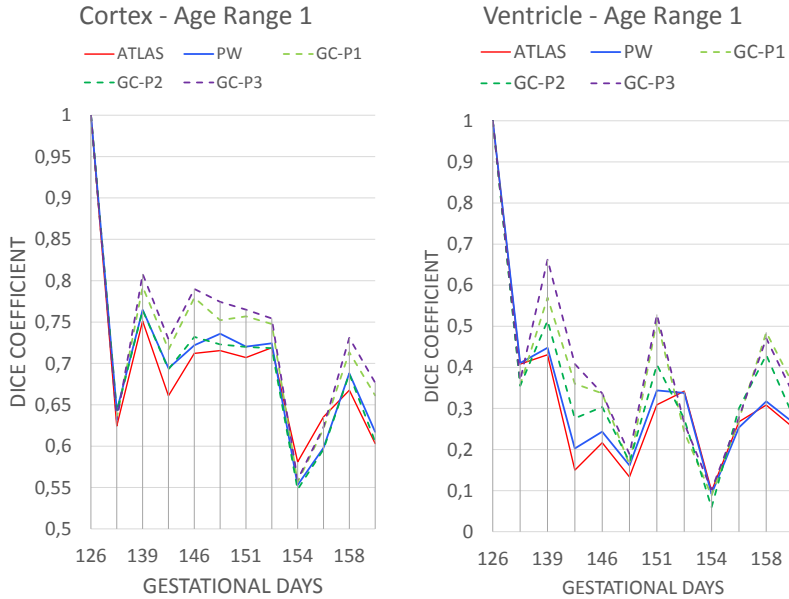


Figure 6.16: DC distribution of cortical (left) and ventricular (right) tissue of the graph cut analysis in 2D for age range 1.

based segmentations is observable at age range 1. Penalty term 3 performs best, with the highest

DC at GD 139 of about 0.81 for cortical and 0.65 for ventricular tissue. The worst results are achieved at GD 154 with a DC of about 0.55 for the cortex and 0.1 for ventricle. In Figure 6.17 an example of a labeling result of cortex and ventricle at age range 1 - GD 146 (GW 20 day 6) is presented. In the first row the graph cut input terms are shown: in the first column the data term, from column 2 to 4 the evaluated penalty term and in columns 5 and 6 the cost terms for cortex and ventricle. In the second and third row atlas-based, transformed atlas based, the graph cut outputs using penalty terms 1, 2 and 3 and the manual segmentations are illustrated. The estimated

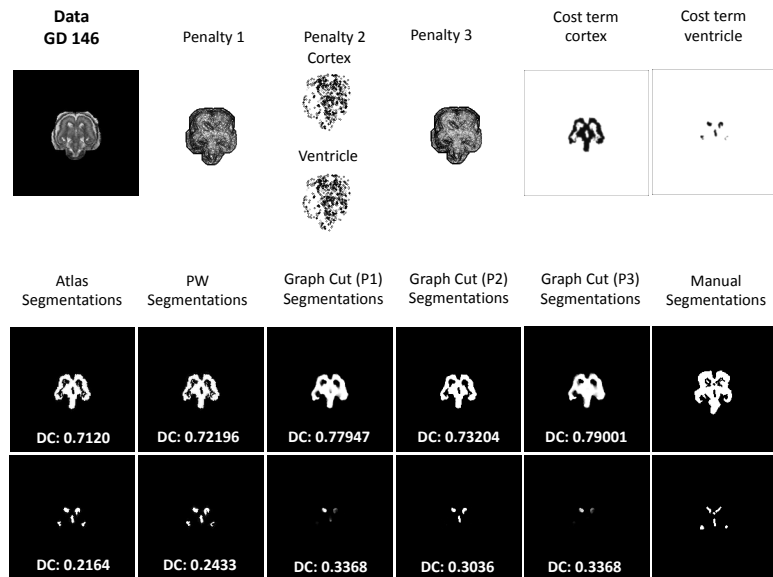


Figure 6.17: Graph cut analysis 2D using the input image at GD 146 (GW 20 day 6)

atlas based segmentations reach a DC of 0.7120 for cortical and 0.2164 for ventricular structure. The pairwise registration from atlas space to the subject's space leads to an DC increase of about 0.01 for cortex and 0.03 for ventricle. The graph cut segmentations using penalty 3 show the highest increase of the DC compared to pairwise (PW) registered segmentations for both tissue types, from 0.72196 to 0.79001 (cortex) and from 0.2433 to 0.3368 (ventricle). The lowest DC increase shows the segmentation result for ventricle as well as for cortex using penalty 2 with a DC of about 0.73204 (cortex) and 0.3036 (ventricle).

Figure 6.18 illustrates the DC distribution of segmentations of the cortex and ventricles at age range 2. The red line represents the DC of atlas based segmentations, the blue line the DC of transformed segmentations using pairwise registration, the dotted light green, dark green and purple line the DC of graph cut based segmentations computed using penalty terms 1, 2 and 3. For the cortex labeling a DC improvement between atlas based and graph cut based segmentations is observable at age range 2. Ventricle segmentations show an increase of DC between atlas and graph cut based segmentations from GD 164 to GD 172, where penalty term 3 performs best, with the highest DC at GD 168 of about 0.86 (cortex) and 0.58 (ventricle). The

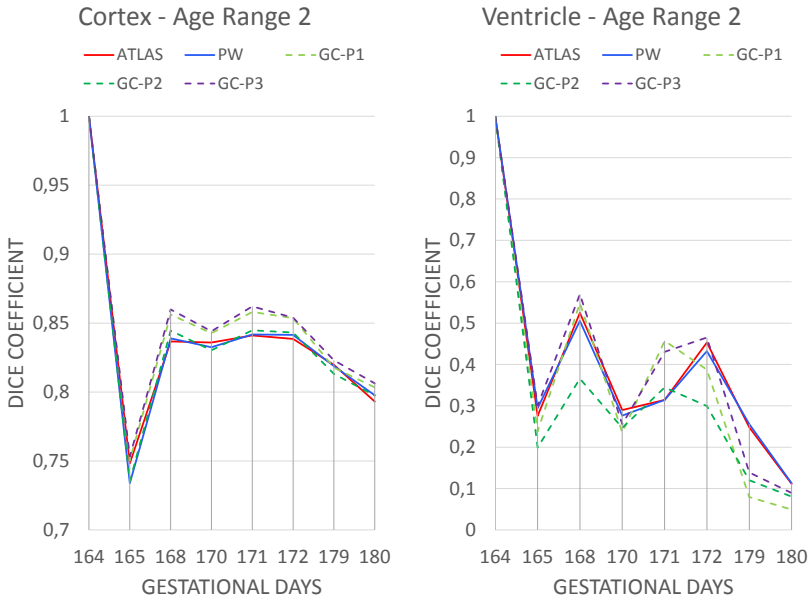


Figure 6.18: DC distribution of cortical (left) and ventricular (right) tissue of the graph cut analysis in 2D for age range 2.

lowest DC is achieved at GD 180 with a DC of about 0.81 for the cortex and 0.1 for ventricle structure. In Figure 6.19 an example of a labeling result of cortex and ventricle at age range 2 is presented. The brain structure and ventricle structure at GD 171 (GW 24 day 3) are labeled. In the first row the graph cut input terms are shown: in the first column the data term, from column 2 to 4 the evaluated penalty term and in columns 5 and 6 the cost terms for cortex and ventricle. In the second and third row atlas-based, transformed atlas based, the graph cut outputs using penalty terms 1, 2 and 3 and the manual segmentations are illustrated. The estimated atlas based segmentations reach a DC of 0.841 for brain and 0.3143 for ventricle structures. No significant DC increase is reached using pairwise registration from atlas space to the subject's space. The graph cut segmentations using penalty 3 show the highest increase of the DC compared to pairwise (PW) registered segmentations for cortical tissue, from 0.8417 to 0.8621. For ventricular tissue penalty term 1 performs best with a DC increase from 0.3143 to 0.4571. The lowest DC increase shows the segmentation result for ventricle as well as for cortex using penalty 2 with a DC of about 0.8448 (cortex) and 0.3444 (ventricle).

Figure 6.20 illustrates the DC distribution of segmentations of the cortex and ventricles at age range 3. The red line represents the DC of atlas based segmentations, the blue line the DC of transformed segmentations using pairwise registration, the dotted light green, dark green and purple line the DC of graph cut based segmentations computed using penalty terms 1, 2 and 3. For the cortex labeling a DC increase between atlas based and graph cut based segmentations (penalty 3) of about 0.05 is observable at age range 3. In contrast to this, ventricle segmentations show a decrease of DC between atlas and graph cut based segmentations. An improvement of atlas based segmentations using pairwise registration is only observable at GD 203. The low-

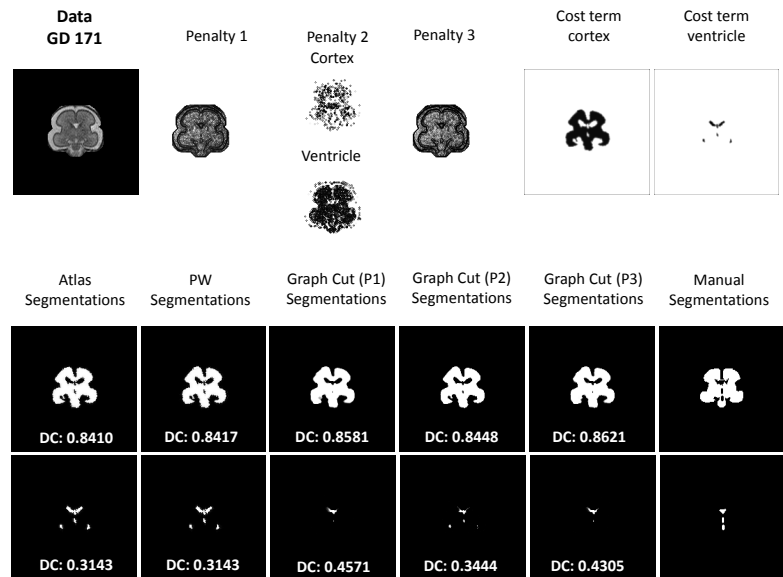


Figure 6.19: Graph cut analysis 2D using the input image at GD 171 (GW 24 day 3).

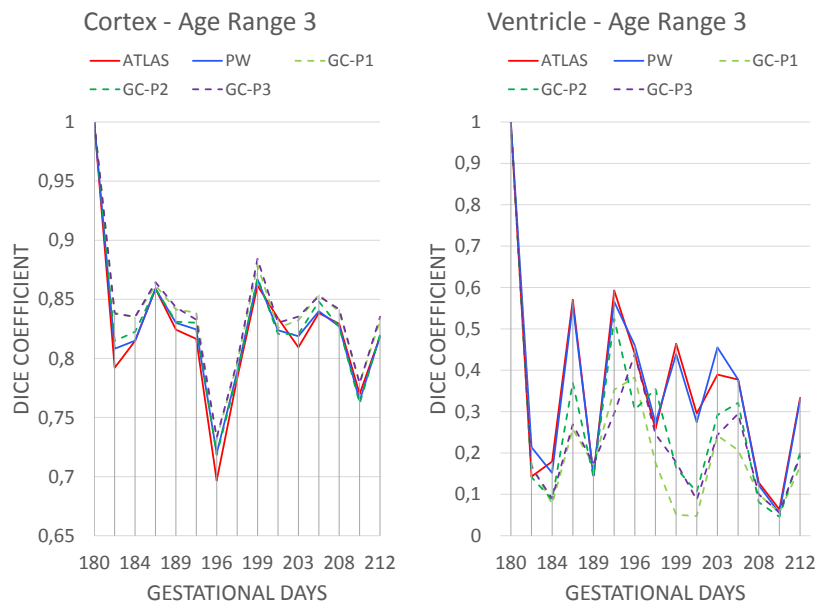


Figure 6.20: DC distribution of cortical (left) and ventricular (right) tissue of the graph cut analysis in 2D for age range 3.

est DC of cortical segmentations is achieved at GD 196 of about 0.72 and of ventricular tissue at GD 199 of about 0.05. The highest DC for cortex labeling of about 0.88 is reached at GD 199. In Figure 6.21 an example of a labeling result of cortex and ventricle at age range 3 is presented. The brain structure and ventricle structure at GD 203 (GW 29 day 0) are labeled. In the first row the graph cut input terms are shown: in the first column the data term, from column 2 to 4 the evaluated penalty term and in column 5 and 6 the cost terms for cortex and ventricle. In the second and third row atlas-based, transformed atlas based, the graph cut outputs using penalty terms 1, 2 and 3 and the manual segmentations are illustrated. The estimated atlas based

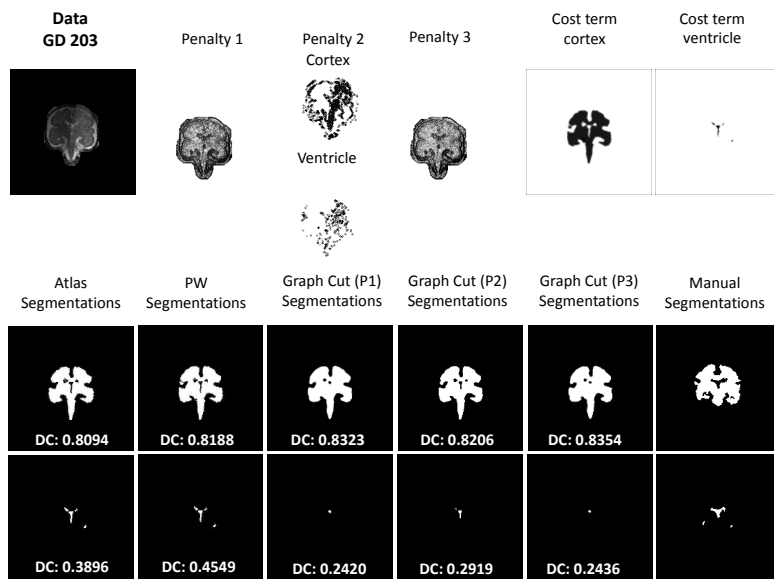


Figure 6.21: Graph cut analysis 2D using the input image at GD 203 (GW 29).

segmentations reach a DC of 0.8094 for brain and 0.3896 for ventricle structures. The pairwise registration from atlas space to the subject's space leads to a DC increase of about 0.01 for cortex and 0.07 for ventricle. The graph cut segmentations using penalty 3 show the highest increase of the DC compared to pairwise (PW) registered segmentations for cortical tissue, from 0.8188 to 0.8354. In contrast to this, graph cut refinement of ventricular tissue at age range 3 leads to a decrease of the DC from 0.4549 to 0.2919.

The 2D analysis of the graph cut shows that independent from the age an increase of the DC between atlas-based and graph cut based segmentations is achievable. It is observed that penalty terms 1 and 3 achieve better results than penalty term 2. A possible reason is the gray value discrepancy caused by the MR imaging technique (cf. Chapter 2.1), since penalty term 2 incorporates the gray value information of the input image. Thus, the labeling result is dependent on the quality of atlas-based segmentations and also on the gray value variances for a tissue type caused by the MR imaging technique.

6.5 Summary

In this chapter the proposed tissue framework, its functionality and structure are introduced. The acquisition setup of the dataset used as well as the created preprocessing pipeline for 2D and 3D images are explained. Subsequently, the state-of-the-art algorithms applied for longitudinal registration and graph cut labeling are presented and their analysis in 2D are documented.

In the course of this thesis three different longitudinal registration schemes are developed and analysed, regarding the ability to model the fetal brain development. Scheme one focuses on using a unique parametrisation for a cascade of initialisation levels using a different number of images. In contrast to this, scheme two aims to register the whole dataset. Three runs with different parametrisation of the vector field regularisation are performed using the learned vector field of the previous run as initialisation. For scheme three development stage dependent age ranges are defined and corresponding datasets are created. For every age range different option parameters for longitudinal registration are used. The results indicate that the scheme that uses three age ranges with different parametrisation of the velocity vector field regularisation shows the best longitudinal registration behaviour, compared to the remaining schemes. It makes it possible to parametrise the vector field regularisation according to the stage of brain development. The analysis of the graph cut approach used tests the automatic tissue labeling procedure for gray value images using atlas based segmentations as initialisation term. Three different parameter sets for this labeling technique are analysed and the corresponding documentation concludes this chapter.

Evaluation of the Tissue Labeling Framework

This chapter summarizes the evaluation results of the tissue labeling framework. Evaluation is performed using leave-one-out-cross validation (LOOCV). A dataset (cf. Section 6.1) of m volumes is divided into a test dataset consisting of a volume at age t and into a training dataset consisting of $m - 1$ volumes at ages not equal to t . The evaluation procedure is performed for each age range separately:

Age range 1: 20 GW day 6 (146 GD) - 23 GW day 3 (164 GD)

Age range 2: 23 GW day 3 (164 GD) - 26 GW day 2 (184 GD)

Age range 3: 26 GW day 2 (184 GD) - 30 GW day 2 (212 GD)

The following sequence is performed for every time-point:

- Assemble test and training datasets for corresponding age range
- Learn atlas using training set.
- Estimate atlas based template at testing time-point.
- Obtain a transformation T using pairwise registration from the test MR volume to the atlas-based template.
- Transform the atlas based segmentation to the test-subject's space using transformation T^{-1} .
- Compute the segmentation of the test volume using the transformed atlas.

Three performance measurements are used within the evaluation process: First the **Dice overlap** is computed between the test dataset and the atlas based, the transformed atlas based and the

graph cut based segmentations of the cortex and ventricles. As second and third features the **volume** of the cortex and ventricles and the **area of the cortical surface** of the atlas based segmentations are calculated.

7.1 Evaluation of the Continuous Model of Fetal Brain Development

The first part of this chapter documents the evaluation of the accuracy of estimated atlas-based segmentations. According to the experimental results of the image regression algorithm of Ashburner et al. [1] documented in Section 6.3 the same parameter setting of scheme 3 is used for longitudinal registration. The regularisation kernels (ker_args) evaluated are listed in Table 7.1.

Table 7.1: Parametrisation of the kernels used for analysing the regularisation of longitudinal registration.

Kernel No.	λ_1	λ_2	λ_0	λ	μ
1	0.01	0.01	$9e^{-6}$	$1e^{-5}$	$1e^{-5}$
2	$9e^{-6}$	$9e^{-6}$	$9e^{-6}$	0.01	$1e^{-5}$
3	$1e^{-3}$	$9e^{-6}$	$9e^{-6}$	$1e^{-3}$	$1e^{-5}$
4	0.01	$9e^{-6}$	$9e^{-6}$	0.01	$1e^{-5}$
5	$9e^{-6}$	$1e^{-5}$	$9e^{-6}$	$1e^{-5}$	$1e^{-5}$
6	$9e^{-6}$	0.01	$9e^{-6}$	0.01	$1e^{-5}$
7	0.01	0.01	$9e^{-6}$	0.01	$1e^{-5}$
8	$1e^{-4}$	$1e^{-4}$	$9e^{-6}$	$1e^{-4}$	$1e^{-5}$
9	0.9	0.9	$9e^{-6}$	0.01	$1e^{-5}$
10	$9e^{-6}$	$9e^{-6}$	$9e^{-6}$	$1e^{-5}$	$1e^{-5}$
11	$9e^{-6}$	$9e^{-6}$	$9e^{-6}$	$1e^{-4}$	$1e^{-5}$
12	$9e^{-6}$	$9e^{-6}$	$9e^{-6}$	$1e^{-3}$	$1e^{-5}$
13	0.5	0.5	$9e^{-6}$	0.01	$1e^{-5}$
14	$1e^{-5}$	$9e^{-6}$	$9e^{-6}$	$1e^{-5}$	$1e^{-5}$
15	$1e^{-4}$	$9e^{-6}$	$9e^{-6}$	$1e^{-4}$	$1e^{-5}$
16	0.1	0.1	$9e^{-6}$	0.01	$1e^{-5}$
17	0.01	0.01	$9e^{-6}$	0.1	$1e^{-5}$
18	$1e^{-3}$	$1e^{-3}$	$9e^{-6}$	$1e^{-3}$	$1e^{-5}$
19	$9e^{-6}$	$1e^{-4}$	$9e^{-6}$	$1e^{-4}$	$1e^{-5}$
20	$9e^{-6}$	$1e^{-3}$	$9e^{-6}$	$1e^{-3}$	$1e^{-5}$
21	$1e^{-5}$	$1e^{-5}$	$9e^{-6}$	$1e^{-5}$	$1e^{-5}$
A	$5e^{-3}$	$5e^{-3}$	$3e^{-5}$	$1e^{-5}$	$9e^{-6}$

Three different measures are observed for choosing a suitable regularisation kernel for an age range. The Dice Coefficient (DC) gives information about the similarity between an estimated atlas-based segmentation and test dataset and consequently the quality of segmentation. Beside the DC also the behaviour of the regularisation of the volume expansion and changes of the area

of cortical surface have to be taken into account when choosing a suitable kernel. The cortical volume of the fetal brain is measured in cm^3 by counting the corresponding voxels (voxel size $1 \text{ mm} \times 1 \text{ mm} \times 1 \text{ mm}$). The area of the cortical surface of the fetal brain is measured in cm^2 and is computed by summing up the area of the triangles, which are estimated in a triangulation process for extracting the brain surface. Heron's formula is used for the computation of the triangle area. The behaviour of image regression using 21 different regularisation kernels is evaluated for every age range in the following sections. Atlas-based cortical and ventricle segmentations are studied.

Atlas Evaluation Results Age Range 1

Figure 7.1 illustrates the DC of cortex segmentations and Figure 7.4 of ventricle segmentations over gestational days. The results show that the deviation of the DC is higher for ventricle segmentations, approximately with a deviation about 0.10 compared to cortical segmentations about 0.07. For both brain structures kernel 1, 4 and 7 yield the best DCs between 0.55 and 0.85 for cortical and between 0.1 and 0.60 for ventricle segmentations. These kernels share the penalisation of the first derivative (kernel argument λ_1) of the vector fields of about 0.01. The worst DC results are achieved by kernel 5, 10 and 11 with values between 0.45 and 0.82 for the cortex and between 0.05 and 0.55 for the ventricles. The kernels have a low penalisation of the first derivative of about $9e^{-6}$ in common. Figure 7.2 illustrates the volume of the estimated atlas-based cortical segmentations and Figure 7.5 the volume of the ventricle segmentations over the gestational days. GT denotes the ground truth obtained by the manual annotations of the test dataset. It is also observed that kernel 1, 7 and 4 represent best the development of cortical volume over time with the lowest deviation from the manual segmentations. The volume lies between 62 cm^3 at GD 150 to 75 cm^3 at GD 164 in average. The volume of atlas-based ventricle segmentations is modelled best using kernels 1, 7 and 4 and shows an average volume expansion from 4 cm^3 to 5 cm^3 . Figure 7.3 shows the area of the cortical surface of estimated atlas-based segmentations over gestational days. The influence of the regularisation kernels used is shown and a deviation about 7 cm^2 between the areas of cortical surface is observable. Kernel 1 performs best with the lowest average deviation from the test dataset compared to the remaining kernels. The area takes values between 17 cm^2 at GD 150 to 23 cm^2 at GD 164.

Atlas Evaluation Results Age Range 2

Figure 7.6 illustrates the DC of cortex segmentations and Figure 7.9 of ventricle segmentations over gestational days. The results indicate that the deviation of the DC is higher for ventricle segmentations, with a deviation of 0.40 compared to 0.15 for cortical segmentations. Kernels 1, 2 and 4 show the best DCs between 0.60 and 0.83 for the cortex and between 0.22 and 0.46 for the ventricles. For cortical and ventricle tissue the worst but non zero DC results are achieved by kernel 12, 14 and 21 with values between 0.35 and 0.75 for the atlas-based cortex segmentations and between 0.03 and 0.14 for ventricle segmentations. Kernel 21 is characterised by a low smoothness of the velocity vector field (λ) of about $1e^{-5}$. For both brain structures an unstable behaviour (i.e. DC with zero values) is only observed at GD 180 using kernel 8, 15, 6 and at

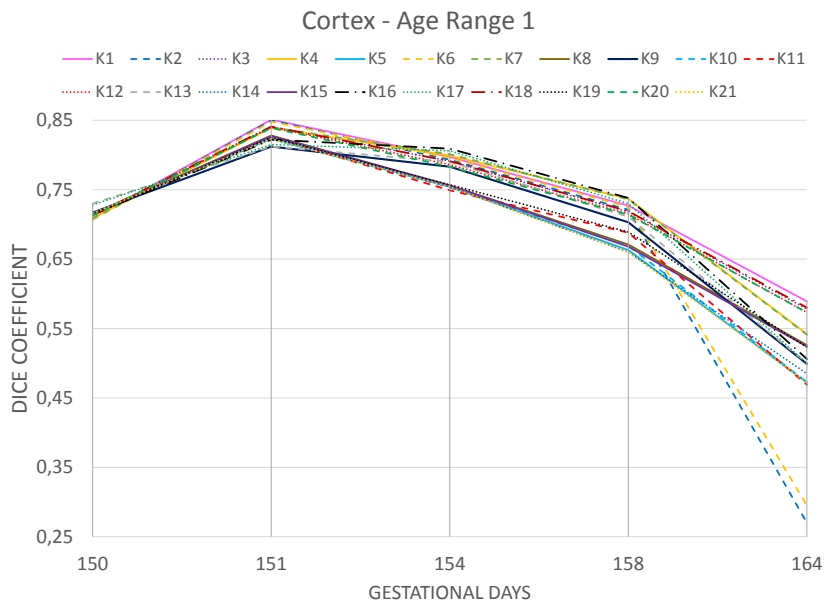


Figure 7.1: DC of cortical segmentations for age range 1.

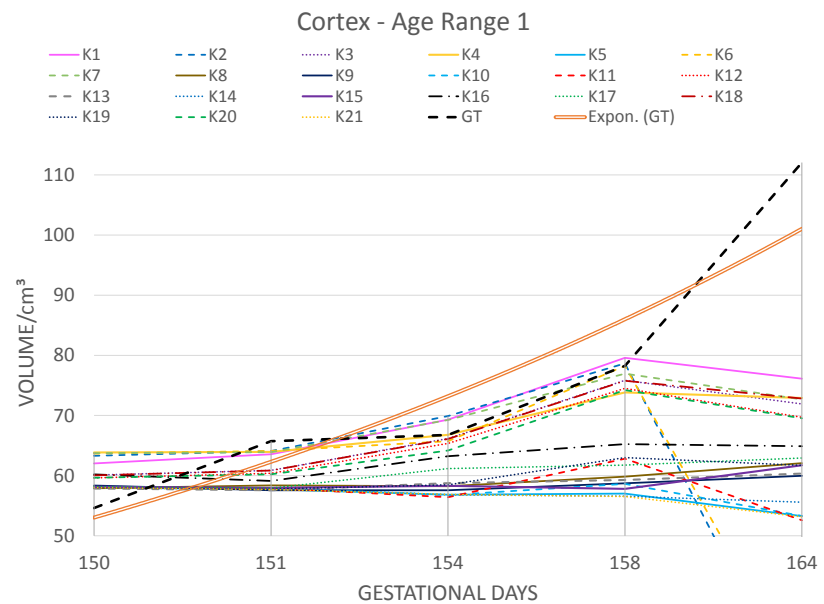


Figure 7.2: Volume of cortical segmentations for age range 1.

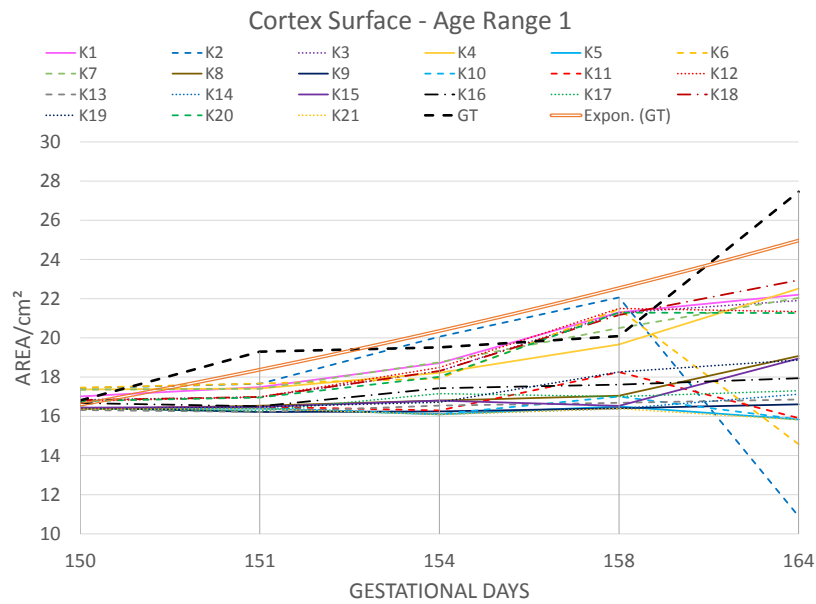


Figure 7.3: Area of the surface of cortical segmentations for age range 1.

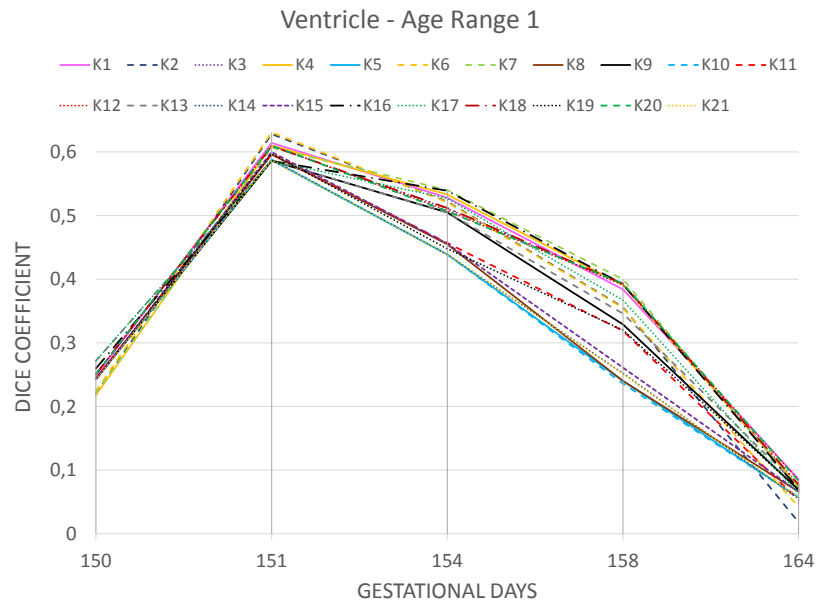


Figure 7.4: DC of ventricle segmentations for age range 1.

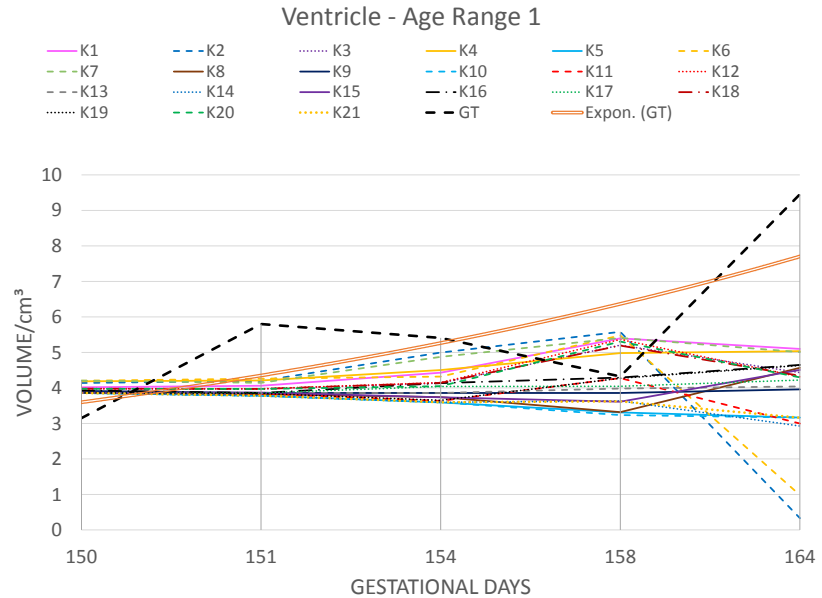


Figure 7.5: Volume of ventricle segmentations for age range 1.

GD 184 using kernels 10, 5, 19, 20, 7 and 16. The kernels leading to unstable results at GD 184 have a smoothness λ lower than $2e^{-3}$ and also a low penalisation of second derivatives λ_2 in common. Kernel 8, 15 and 6 have in common a low penalisation of first derivatives λ_1 less than $4e^{-4}$. Figure 7.7 illustrates the volume of the estimated atlas-based cortical segmentations and Figure 7.10 the volume of the ventricle segmentations over the gestational days. GT denotes the ground truth obtained by the manual annotations of the test dataset. The orange line illustrates the exponential trend line of the ground truth volumes. Kernel 1, 2, 4 and 14 represent best the cortical volume expansion rate over time (first derivative) compared to the average trend, but the volume error lies between 10 cm^3 to 60 cm^3 . At this point of evaluation the volume of atlas based templates (in atlas' space) are compared to the test dataset (in subject's space). No pairwise registration is used to transform atlas based templates to the subject space. This results in scaling differences and consequently in higher volume errors. The scaling of the fetal brains is adapted in a next step which is not part of the atlas learning evaluation. It is modelled in the labeling procedure of the tissue labeling framework using pairwise registration and its evaluation is documented in Section 7.2. The average trend of the ventricle volumes of manual annotations show a shrinkage over the gestational days. Kernel 1, 2, and 4 show the best regularisation behaviour with a deviation from the groundtruth volume of in average 1.5 cm^3 over the gestational ages, but do not model a thinning of ventricles over time. Figure 7.8 shows the area of the cortical surface of estimated atlas-based segmentations over gestational days. Kernel 1 shows a good approximation to the groundtruth area between GD 171 and 180. In contrast to this, kernel 21 shows the lowest average deviation from the groundtruth of about 8 cm^2 and as well as kernel 14 the best modelling results of the brain surface between GD 180 and

184. During this age range cortical folding processes and growing processes take place. This explains the different sensitivity of kernels used for different ages. λ is set to $1e^{-5}$ for kernels 1, 14, 21 in common which indicates that the varying results for a certain age range is dependent on the parametrisation of λ_1 and λ_2 . A low penalisation of first and second derivatives of the flow vector field lead to better results at gestational ages greater than 175 GDs. According to Wright et al. [80] and Pugash et al. [57] cortical folding increases rapidly between GW 25 (GD 175) and GW 30 (GD 210). Here, the positions corresponding to neighboring voxels show a higher change in terms of velocity and acceleration compared to ages smaller than 175 GD with no rapid cortical folding. A low penalisation of second and first derivative allows to accurately model these changes in the flow vector field, which results in a more accurate modelling of brain surface area.

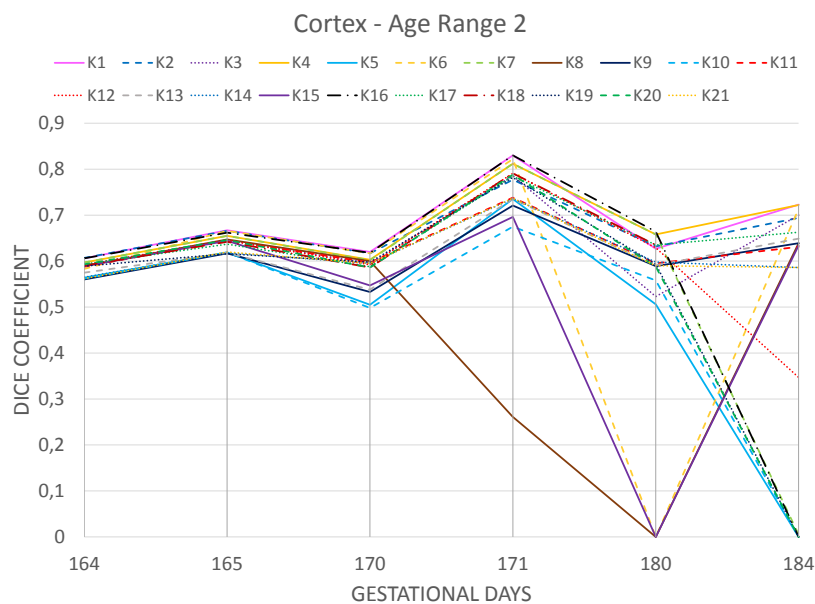


Figure 7.6: DC of atlas-based cortical segmentations for age range 2.

Atlas Evaluation Results Age Range 3

Figure 7.11 illustrates the DC of cortex segmentations over gestational days. The results show that the DC deviation of the different kernels is higher for ventricle segmentations with an average value of 0.20 compared to cortical segmentations of about 0.15. Also age range 3 is dominated by rapid cortical folding and volume changes of the brain [80] [57]. This facts explains the observation that no kernel performs best at every time point of the age range 3. From GD 184 to 196 there is only a DC deviation of 0.01. Differences of regularisation are visible at time point GD 197, where kernel 1, 20, 4 and 19 show the best DCs of about 0.65 for cortical segmentations. In contrast to this at time points between GD 199 and 207, kernel 16, 17, 9

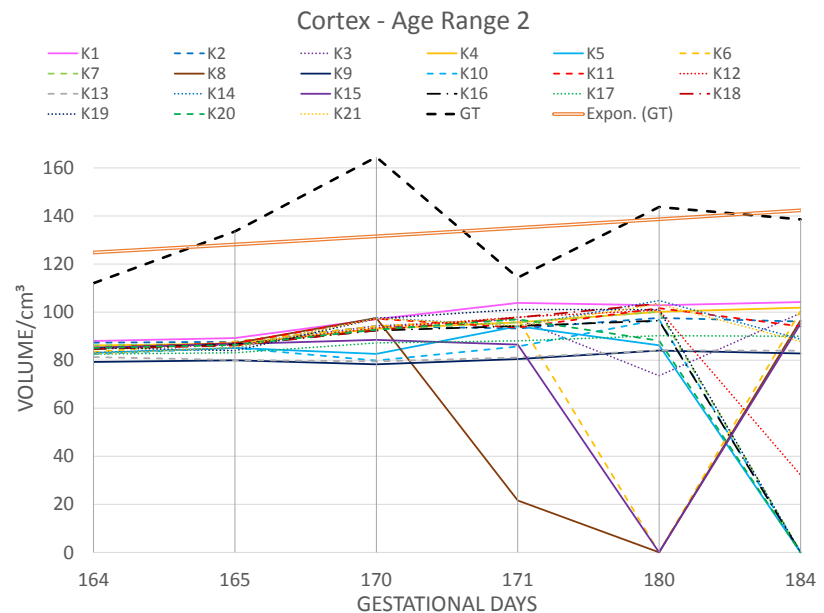


Figure 7.7: Volume of atlas-based cortical segmentations for age range 2.

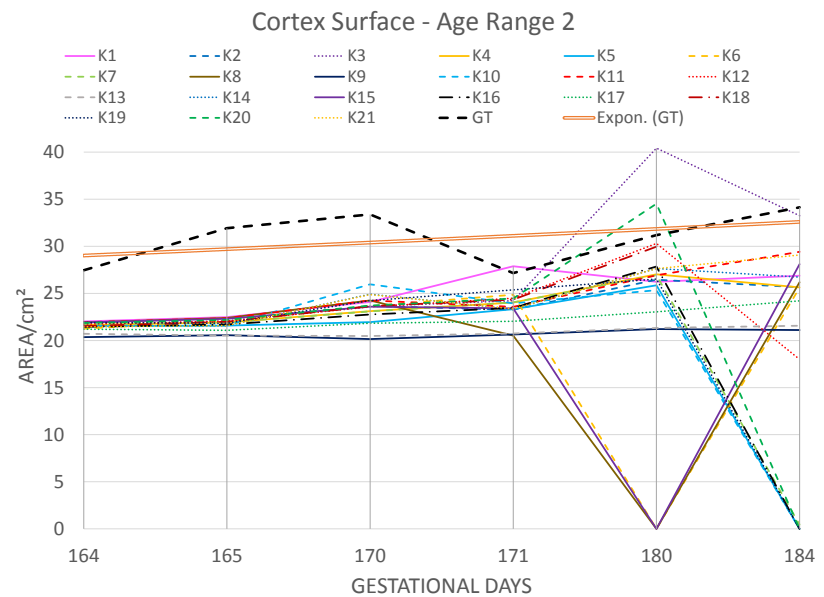


Figure 7.8: Area of the surface of atlas-based cortical segmentations for age range 2.

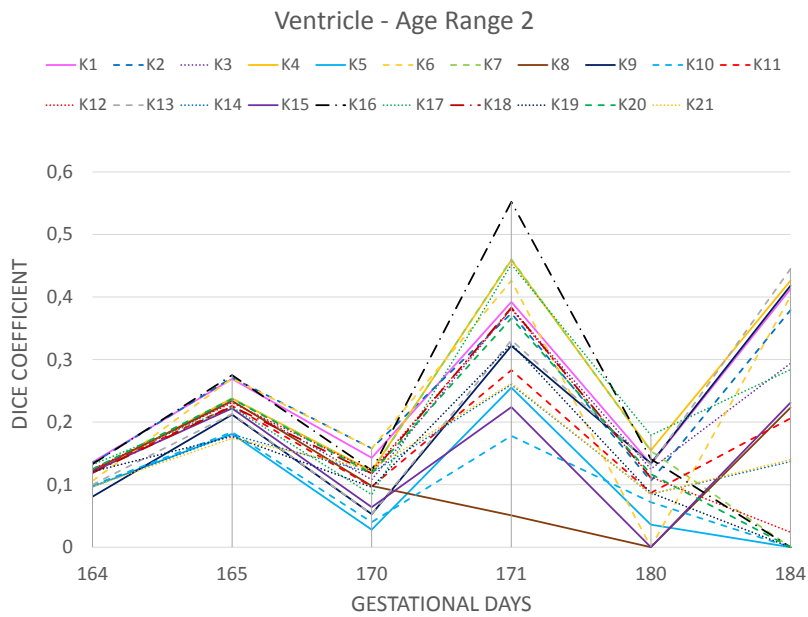


Figure 7.9: DC of ventricle segmentations for age range 2.

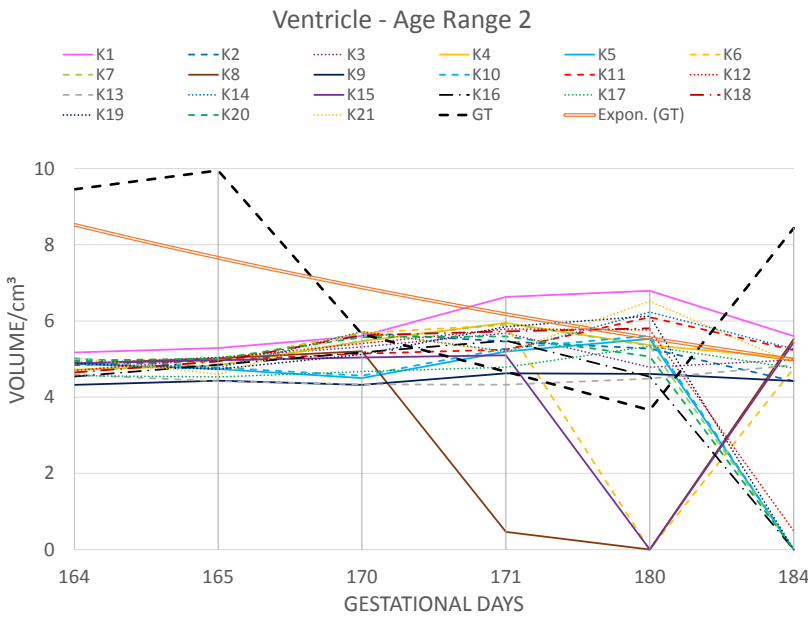


Figure 7.10: Volume of ventricle segmentations for age range 2.

and 13 outperform with the highest DCs between 0.73 and 0.83, but show the worst results at ages older GD 207 with a DC between 0.68 and 0.73. Figure 7.12 presents the DC of ventricle segmentations over the gestational days. From GD 186 to 203 kernel 16, 13, 17 and 9 show the best DC results with 0.45 at GD 203.

Figure 7.13 illustrates the volume of the estimated atlas-based cortical segmentations and Fig-

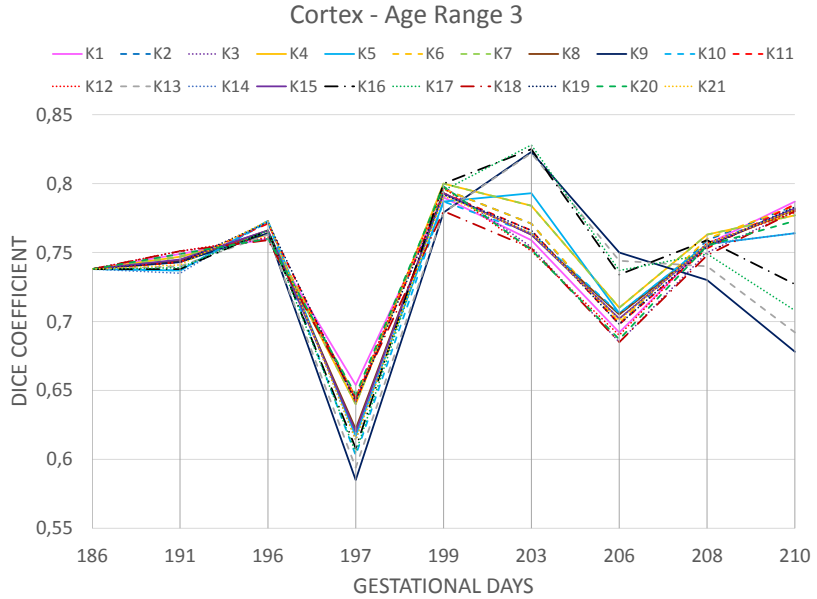


Figure 7.11: DC for cortical segmentations for age range 3.

ure 7.14 the volume of the ventricle segmentations over the gestational days. GT denotes the ground truth obtained by the manual annotations of the test dataset. The orange line illustrates the exponential trend line of the ground truth volumes. The ground truth shows a high variability of occurring volumes in the dataset at neighboured time points, which makes it more challenging to identify a suitable regularisation kernel. Kernels with the best DC results for cortical or ventricle segmentations show a worse ability to model volume changes over time, e.g. 20 cm^3 of volume change using kernel 16 for cortical or 1 cm^3 volume change for ventricle segmentations. In contrast to this, kernels achieving the lowest DCs show a higher volume change over time, e.g. 40 cm^3 of expansion using kernel 18 for cortical and 6 cm^3 of expansion for ventricle segmentations.

Figure 7.15 shows the area of the cortical surface of estimated atlas-based segmentations over gestational days. The modelling of the area of cortical surface shows the same regularisation behaviour as in modelling the volume. Kernels with the best DC results for cortical surface show a worse ability to model area changes over time, e.g. 3 cm^2 using kernel 16. In contrast to this, kernels achieving the lowest DCs show a higher surface change over time, e.g. 23 cm^2 using kernel 18.

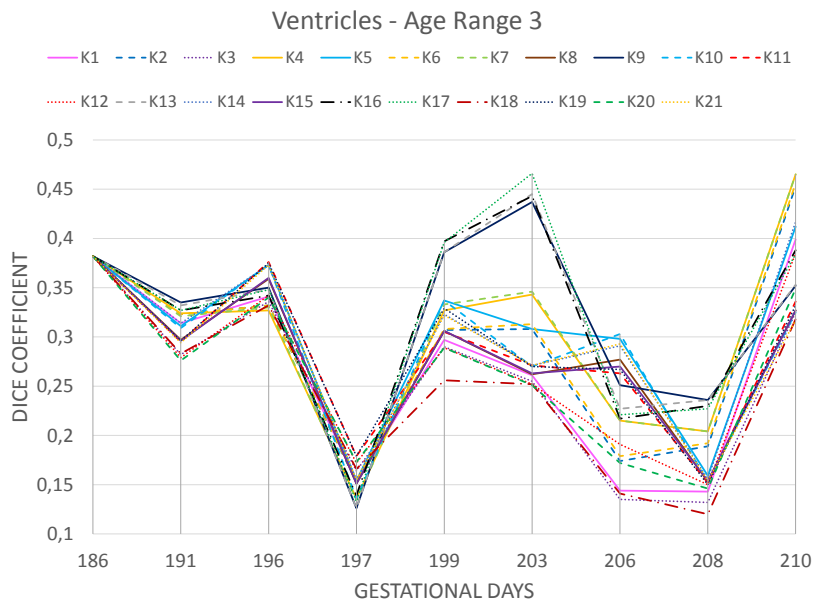


Figure 7.12: DC for ventricle segmentations for age range 3.

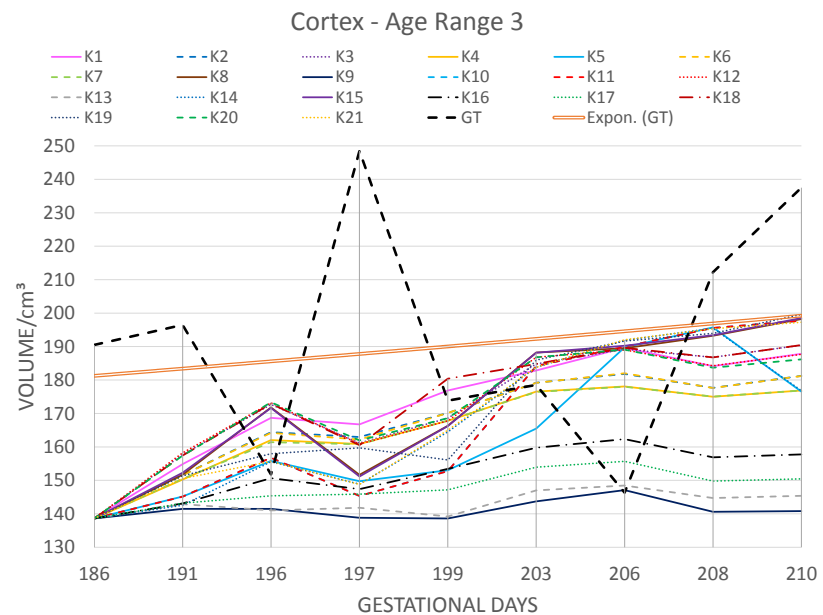


Figure 7.13: Volume for cortical segmentations for age range 3.

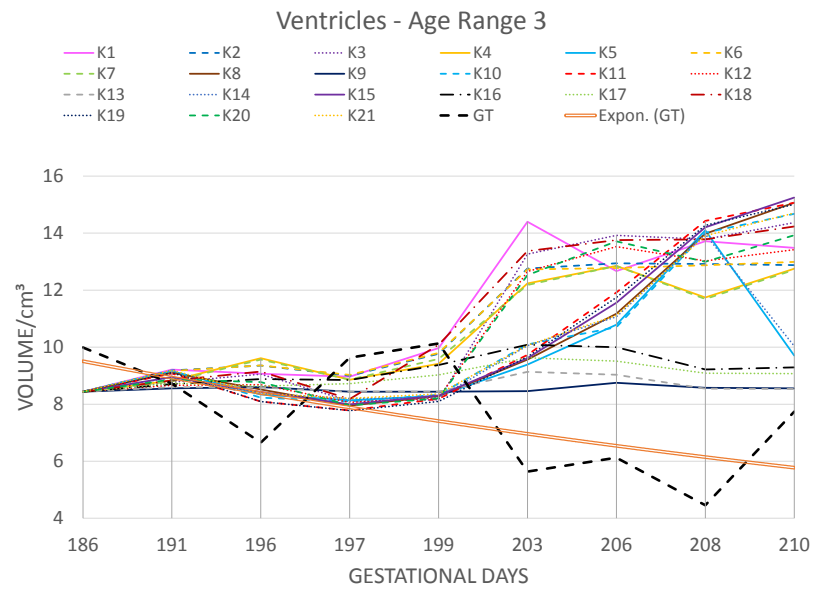


Figure 7.14: Volume of ventricle segmentations for age range 3.

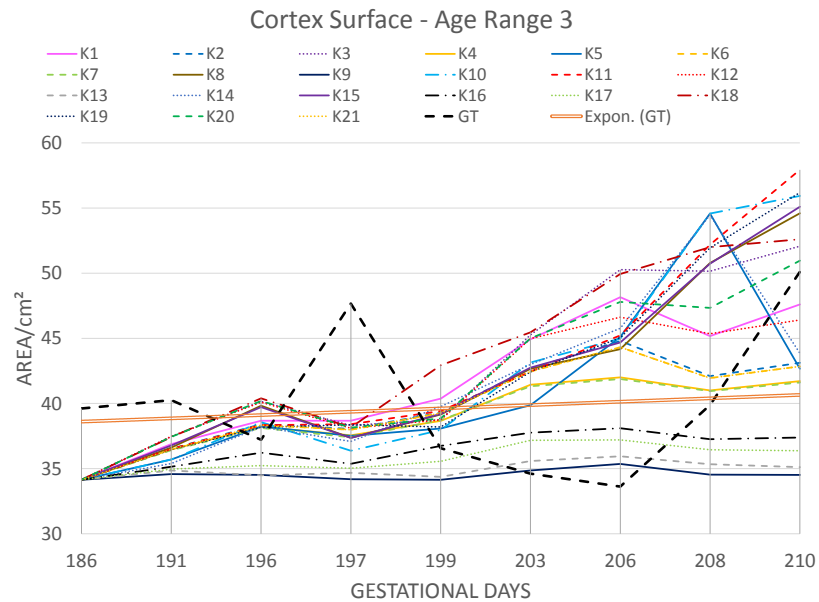


Figure 7.15: Area for segmentation of the cortical surface for age range 3.

Results Atlas-based Templates

Figure 7.16 illustrates the atlas-based templates for age range 1, 2 and 3. For every age range coronal, axial and sagittal slices are illustrated in the first, second and third rows respectively.

According to the evaluation results, kernel 1 is chosen as suitable regularisation for fetal brain

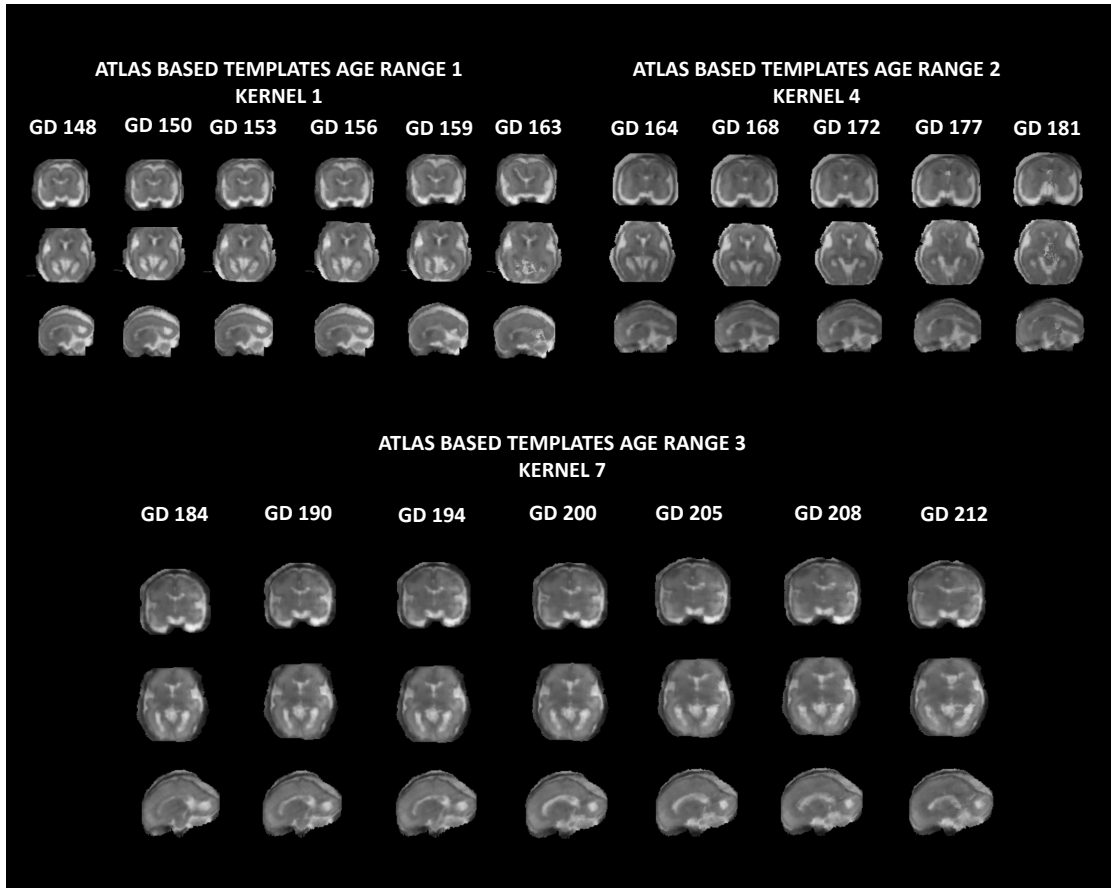


Figure 7.16: Atlas based templates of age range 1, 2 and 3 between GW 21 day 1 (GD 148) and GW 30 day 2 (GD 212).

atlas learning at age range 1, because it shows the highest average DC of about 0.70 for cortical and 0.40 for ventricle structure. Kernel 4 is used for age range 2, since it shows an average DC of 0.70 for cortical and 0.35 for ventricle tissue. Also the volume change rate is similar to the trend of the ground truth data and is able to model the occurring changes of cortical surfaces over the gestational age with an average deviation from ground truth of approximately 7 cm^2 . For the atlas of age range 3 a setting using kernel 7 is considered, since it shows an average DC of about 0.70 for cortical and 0.30 for ventricle segmentations. Figure 7.17 illustrates anatomical details of the estimated atlas based templates at age GW 21 day 4 (GD 151), GW 24 day 3 (GD 171) and GW 29 (GD 203). Coronal slices are shown in the first row, axial in the second row

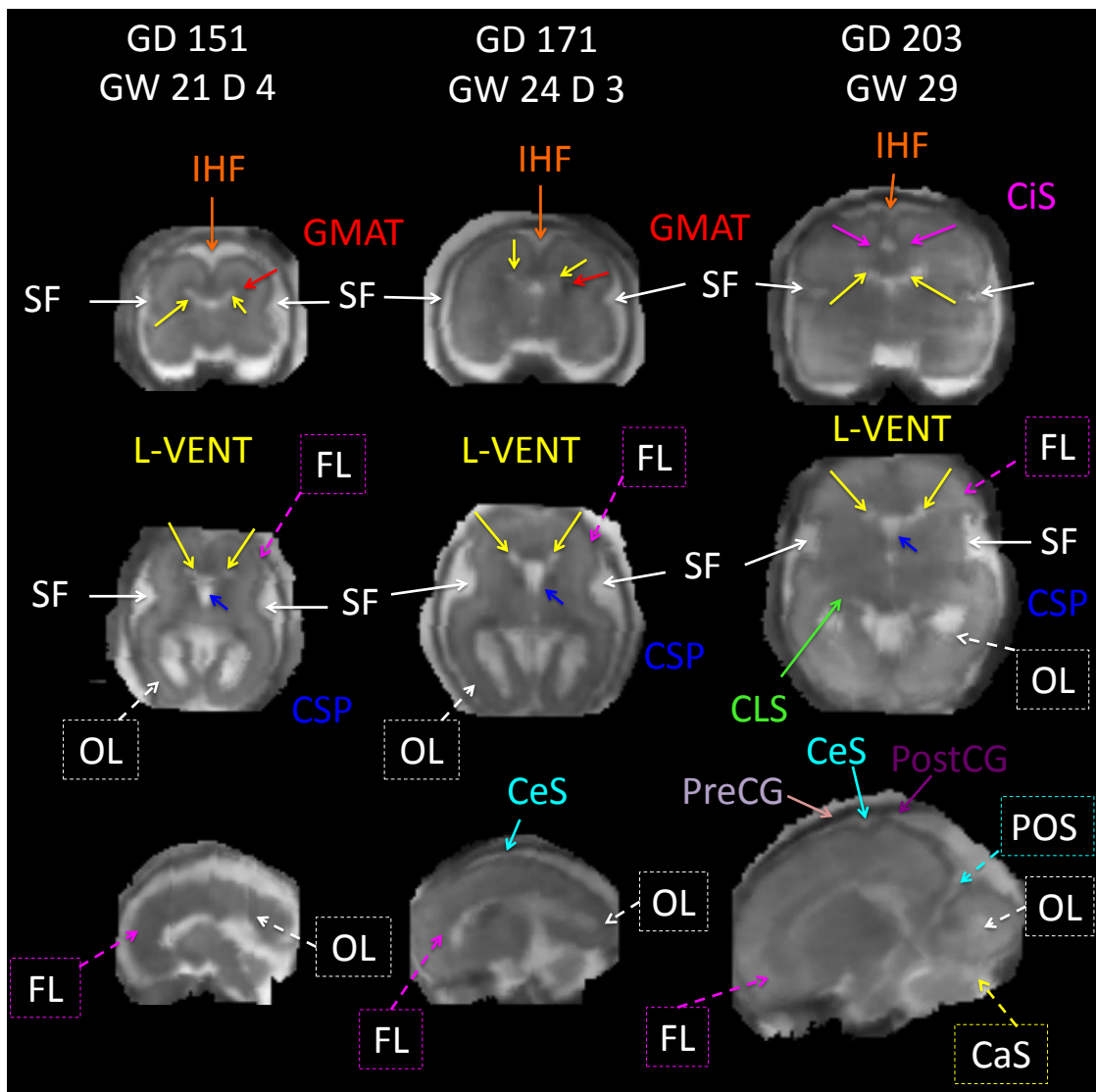


Figure 7.17: Anatomical details of atlas based templates at age GW 21 day 4 (GD 151), GW 24 day 3 (GD 171) and GW 29 (GD 203). Coronal (first row), axial (second row) and sagittal (third row) slices are illustrated. Observable structures at every age range are Sylvian Fissure (SF), Lateral VENTricle (L-VENT), InterHemispheric Fissure (IHF), Cavum of Septum Pellucidum (CSP), Occipital Lobe (OL) and Frontal Lobe (FL). The Germinal MATrix (GMAT) is existent until age range 2 and disappears later in the third trimester of pregnancy. The Central Sulcus (CeS) formation starts at age range 2 and gets more apparent at age range 3 as well as the PreCentral Gyrus (PreCG) and PostCentral Gyrus (PostCG). The Collateral Sulcus (CLS) is visible at age range 3 as well as Cingulate Sulcus (CiS) and Calcarine Sulcus (CaS).

and sagital in the third row. Observable structures at every age range are Sylvian Fissure (SF), Lateral VENTricle (L-VENT), InterHemispheric Fissure (IHF), Cavum of Septum Pellucidum (CSP), Occipital Lobe (OL) and Frontal Lobe (FL). The Sylvian Fissure (SF) show in the coronal and axial slices a smooth bending at age range 1 and develop to a deep fold at the lateral side of the brain at age range 3. Also the InterHemispheric Fissure (IHF) shows a deeper folding at age range 3 with Cingulate Sulcus (CiS) as additional forming compared to age range 1. The Germinal MATrix (GMAT) is existent until age range 2 and disappears later in the third trimester of pregnancy. The Central Sulcus (CeS) formation starts at age range 2 and gets more apparent at age range 3 as well as the developing of the PreCentral Gyrus (PreCG) and PostCentral Gyrus (PostCG). Also the ColLateral Sulcus (CLS) develops at age range 3 and is observable in the atlas based templates. Figure 7.18 shows a 3D visualisation of the computed atlas-based fetal brain model at age GW 21 day 6 (GD 151), GW 24 day 3 (GD 171) and GW 29 (GD 203). Figure 7.19 shows a 3D visualisation of the computed atlas-based fetal ventricle model at age GW 21 day 6 (GD 151), GW 24 day 3 (GD 171) and GW 29 (GD 203). In both figures the growth of the brain structures is observable. The 3D brain model at age range one is characterised by a smoother cortex surface in comparison to a brain at a higher age range. It also visualises the increase of the cortical folding grade. According to Pugash et al. [57], the ventricle achieve their thickest size in early gestation and regress in the third trimester, which is not visible in Figure 7.19. The regularisation term for geodesic regression is not able to model location specific volume expansion and shrinkage at the same time. This leads to worse modelling results, compared to cortical structure, since a kernel is used which models expansion. Additionally, the subject specific variability of age-dependent ventricle size in the dataset and the complex form of ventricles complicate the registration procedure.

7.2 Evaluation of the Tissue Labeling Procedure

According to the evaluation results for the continuous fetal brain model reported in Section 7.1, the following regularisation parameters are used for the longitudinal registration of the three atlases at age range 1, 2 and 3:

- Atlas regularisation age range 1 (GD 126 - GD 165): kernel 1
- Atlas regularisation age range 2 (GD 165 - GD 180): kernel 4
- Atlas regularisation age range 3 (GD 180 - GD 212): kernel 7

For transforming the atlas based templates into the subject's space, pairwise registration is used.

Pairwise parameter setting: $M = []$, numIter=100, epsilon=0.0004, maxEps=0.4, minEps=0.008, maxStepLen=1, voxSize=[1 1 1], fmg_arg=[15 5 5], spl_deg=[6 6 6], ker_type=1 (membrane energy model (Laplacian model)), solver=0 (Gauss-Newton), TolIt=0.001, nRes=5, multichannel=0, wrapDim=[0 0 0] and regularisation kernel A (cf. Table 7.1).

To perform the graph cut refinement of the atlas based segmentation, penalty terms P_1 , P_2 and

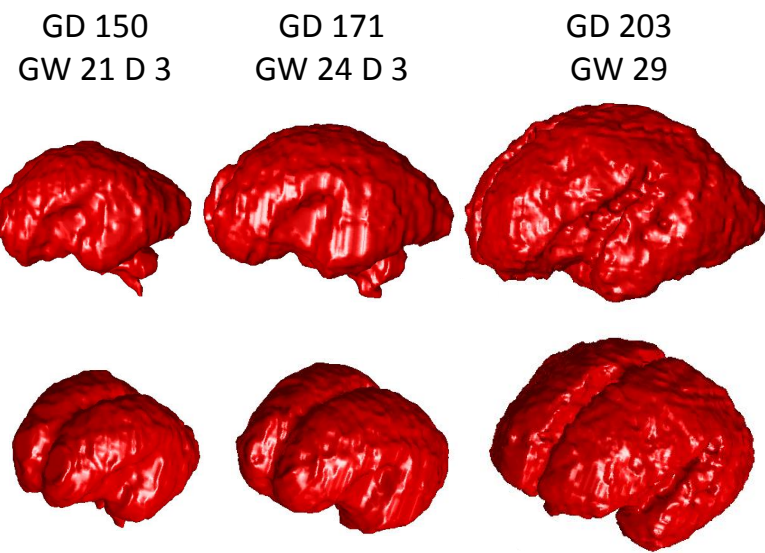


Figure 7.18: 3D visualisation of the computed fetal brain model of the cortex at age GW 21 day 3 (GD 150), GW 24 day 3 (GD 171) and GW 29 (GD 203).

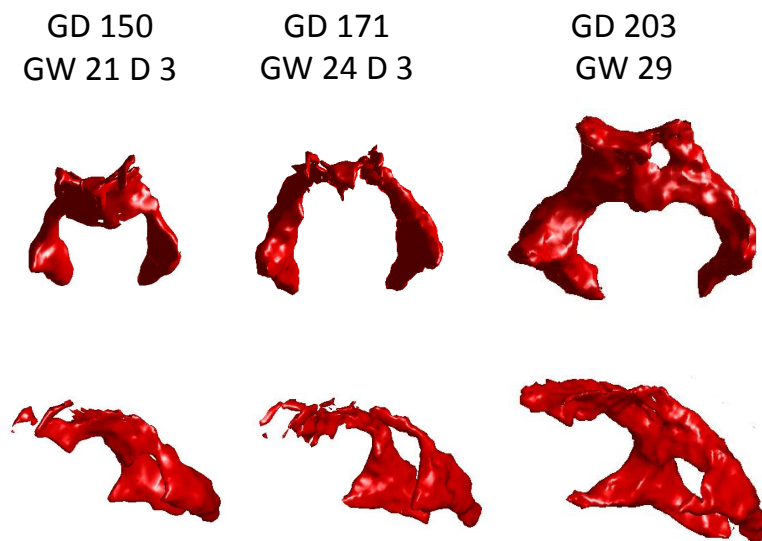


Figure 7.19: 3D visualisation of the computed fetal brain model of the ventricle at age GW 21 day 3 (GD 150), GW 24 day 3 (GD 171) and GW 29 (GD 203).

P_3 (cf. Section 6.4) are evaluated. The graph cut is parametrised using a different setting for cortex and ventricle labeling.

Graph cut parameter setting cortex: $\delta=1.25$, $a=50$, $b=1$, $u=0.9$, $v=0.1$, $w=0.01$, $\sigma=0.9$, $\text{maxIter}=200$, $\text{nlab}=3$, $\text{errorBound}=0.0001$, $\text{cc}=1.5$, $\text{stepSize}=0.009$, $\text{ulab}(\text{background})=0$, $\text{ulab}(\text{cortex})=1$, $\text{ulab}(\text{ventricle})=2$.

Graph cut parameter setting ventricle: $\delta=1.25$, $a=290$, $b=2$, $u=0.9$, $v=0.1$, $w=0.05$, $\sigma=0.9$, $\text{maxIter}=200$, $\text{nlab}=3$, $\text{errorBound}=0.0001$, $\text{cc}=1.5$, $\text{stepSize}=0.009$, $\text{ulab}(\text{background})=0$, $\text{ulab}(\text{cortex})=1$, $\text{ulab}(\text{ventricle})=2$.

Discussion Results Cortex Segmentations

The DC distribution of segmentations of the cortex for age range 1 are illustrated in Figure 7.20, for age range 2 in Figure 7.21 and for age range 3 in Figure 7.22. The red line represents the DC of atlas based segmentations, the blue line the DC of transformed segmentations using pairwise registration, the dotted light green, dark green and purple line the DC of graph cut based segmentations computed using penalty terms 1, 2 and 3. For age range 1 the highest

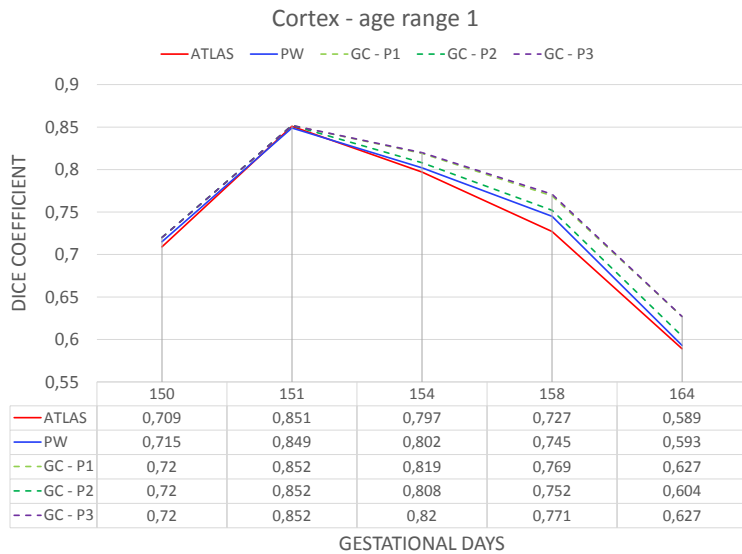


Figure 7.20: Dice Coefficient of atlas based (red), transformed atlas based (blue) and graph cut based segmentations of the cortex at age range 1 using penalty 1 (light green), penalty 2 (dark green) and penalty 3 (purple).

DC improvement from 0.727 to 0.771 at GD 158 is achieved by pairwise registration and graph cut refinement compared to atlas based segmentations. In contrast to this no improvement is reached at GD 151, but shows the highest DC of about 0.851. At GDs older than 154 the graph cut refining using penalty 1 and penalty 2 achieve a higher DC increase of about 0.02 compared

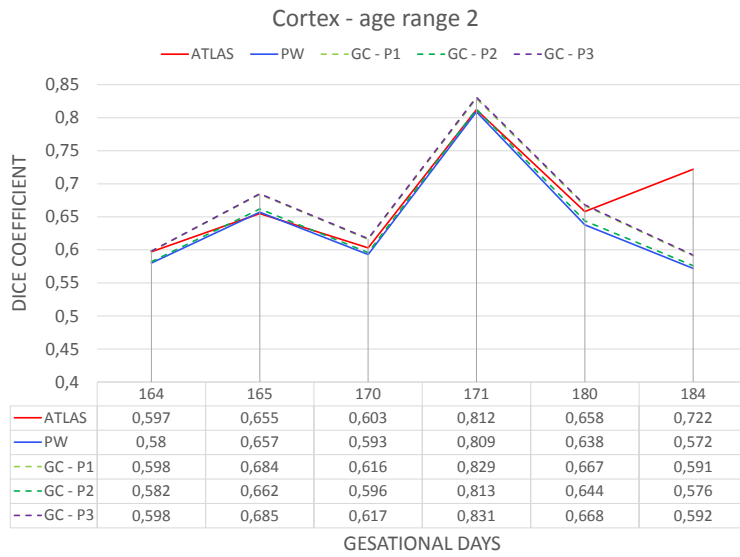


Figure 7.21: Dice Coefficient of atlas based (red), transformed atlas based (blue) and graph cut based segmentations of the cortex at age range 2 using penalty 1 (light green), penalty 2 (dark green) and penalty 3 (purple).

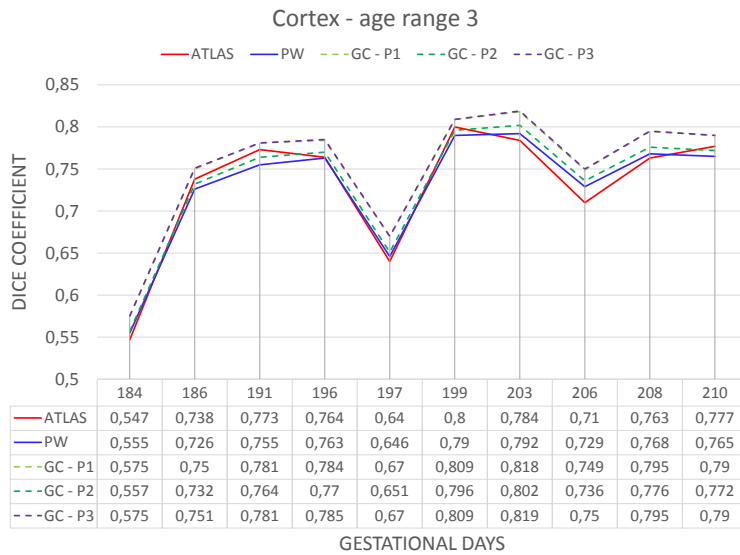
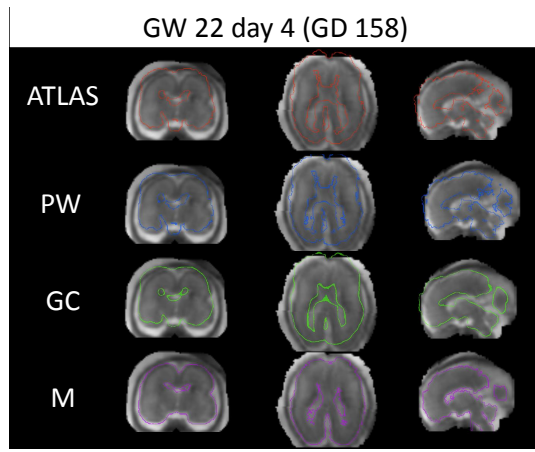


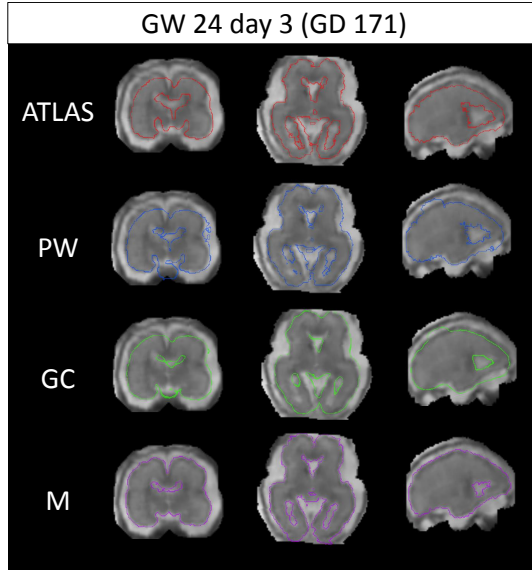
Figure 7.22: Dice Coefficient of atlas based (red), transformed atlas based (blue) and graph cut based segmentations of the cortex at age range 3 using penalty 1 (light green), penalty 2 (dark green) and penalty 3 (purple).

to using penalty 3. At age range 2 no improvement of transformed atlas based segmentations is observed after pairwise registration, which leads to a decrease of the DC. It is observed that the labeling result of the pairwise registration has influence on the graph cut labeling since it acts as initialization of this procedure. This is best visible at GD 184. The graph cut refinement is able to compensate the results of the pairwise registration between GD 164 and 184 and shows an increase of the DC between atlas-based and graph-cut based segmentations in average of about 0.02. At age range 3 an increase of DC at every age range is achievable using graph cut refinement. The highest improvement between atlas-based segmentations and graph cut based segmentations is reached at GD 206 with an DC increase from 0.71 to 0.795. The highest DC at age range 3 of about 0.819 is achieved at GD 203 and the lowest of about 0.575 at GD 184.

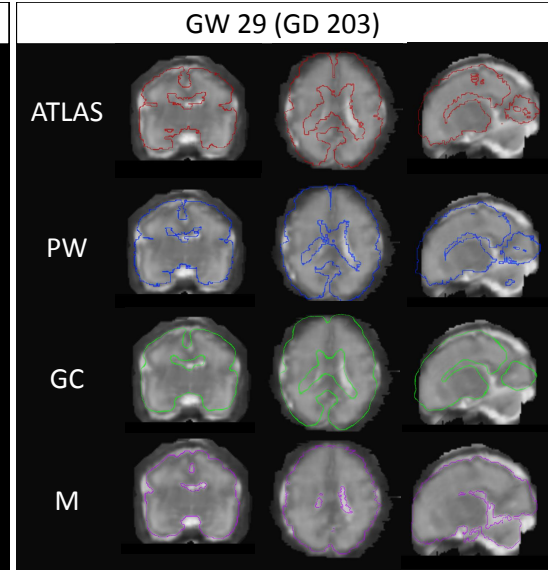
Figure 7.23 illustrates the test data and corresponding estimated segmentations of cortical tissue at GD 158 (7.23a), 171 (7.23b) and 203 (7.23c). The graph cut segmentations are computed using the penalty term 3, since it shows the best improvement between atlas-based and graph cut based segmentations for ventricle and cortex. Atlas based segmentations (red), pairwise registration computed segmentations (blue), graph cut based segmentations (green) and manual segmentations (purple) are visualised. Coronal slices are illustrated in the first column, axial slices in the second and sagittal slices in the third. The volume of the estimated atlas-based segmentation at GD 158 is bigger than the manual segmentation's volume. Additionally a displacement to the right is observable. Pairwise registration which uses kernel A for regularisation is not capable to compensate these differences. According to the atlas' bigger volume the atlas-based segmentation of the temporal lobe is estimated at the skull border. The graph cut approach avoids the cutting through regions of a high gradient, since this would lead to increasing costs in the energy minimisation procedure. Thus, the graph cut is not capable to refine the segmentation to the border of the temporal lobe. The segmentations at GD 171 show a better initial alignment of atlas based labeling with the manual segmentation than at GD 158 but a misplacement of the IHF to the border of the left temporal lobe. The SFs are modelled accurately by the atlas, but the pairwise registration hinders the segmentations of the left one, which is best observable in the axial view. At the sagittal view it is observable that pairwise segmentations lead to an out-grow of the superior border of the cortex which influences the graph cut labeling. In contrast to this, the graph cut refinement is capable to refine the alignment between brain and ventricle tissue. Also the inferior temporal lobe shows a low deviation from the manual segmentations. The labeling for the cortex at GD 203 shows a stepwise refinement from atlas-based to graph-cut based segmentations. Also the inferior temporal lobe covers the manual segmentations. The left SF is deeper estimated by the atlas compared to the manual segmentation, but the graph cut is able to refine this change. At the sagittal view it is observed that the atlas estimates a cortex segmentation with an interception between the occipital and the parietal lobe. The hypointense border caused by the POS impaires the reunion of the two cortex segmentation parts in the graph cut refinement step.



(a) GD 158



(b) GD 171



(c) GD 203

Figure 7.23: Segmentations of the cortex at GD 150, 171 and 203 estimated by the atlas (red), after the pairwise registration procedure (blue), estimated by the graph cut approach (green) and manual segmentations (purple). Coronal slices are illustrated in the first column, axial slices in the second and sagittal slices in the third.

Discussion Results Ventricle Segmentations

The DC distribution of segmentations of the ventricles for age range 1 are illustrated in Figure 7.24, for age range 2 in Figure 7.25 and for age range 3 in Figure 7.26. The red line represents the DC of atlas based segmentations, the blue line the transformed segmentations using pairwise registration and the dotted light green, dark green and purple line the DC of the graph

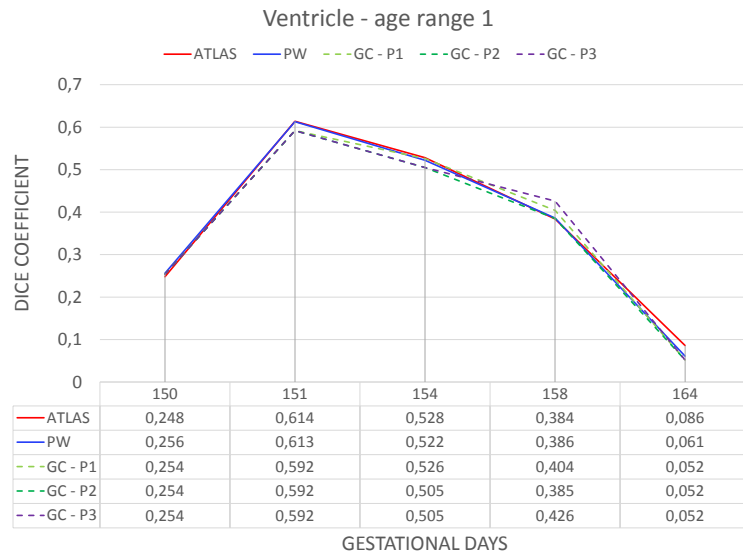


Figure 7.24: Dice Coefficient of atlas based (red), transformed atlas based (blue) and graph cut based segmentations of the ventricles at age range 1 using penalty 1 (light green), penalty 2 (dark green) and penalty 3 (purple).

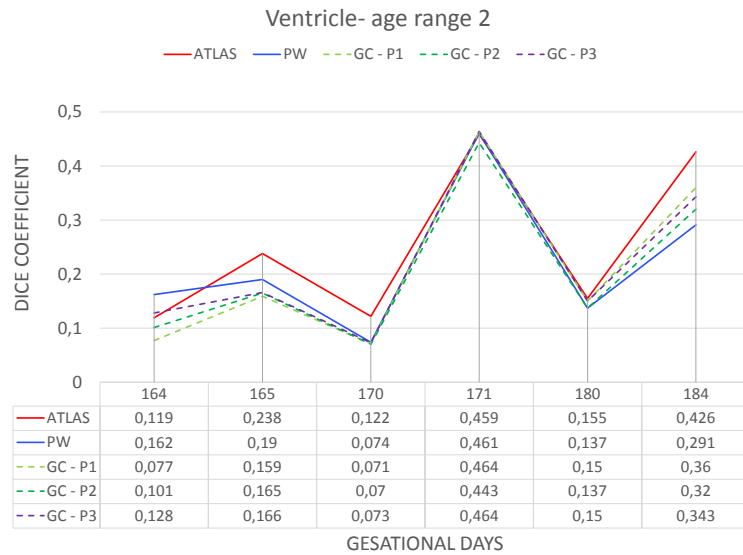


Figure 7.25: Dice Coefficient of atlas based (red), transformed atlas based (blue) and graph cut based segmentations of the ventricles at age range 2 using penalty 1 (light green), penalty 2 (dark green) and penalty 3 (purple)..

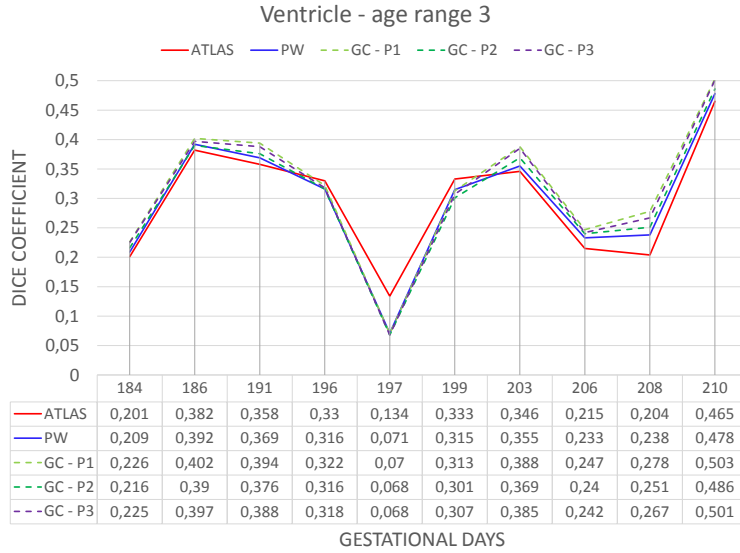
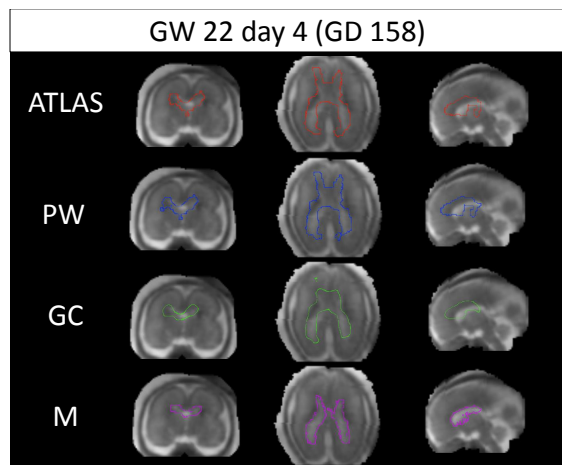


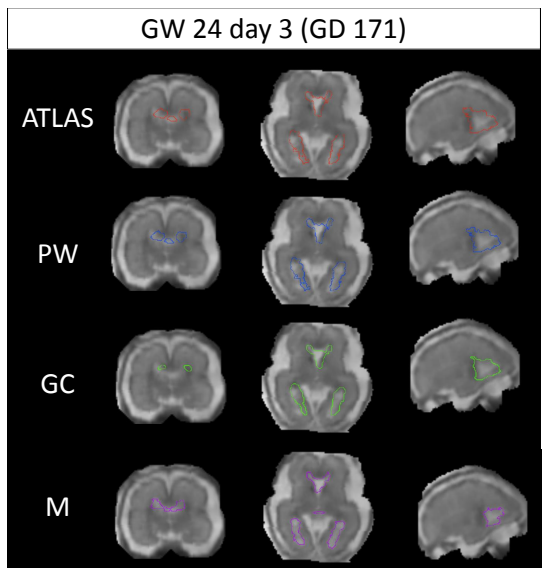
Figure 7.26: Dice Coefficient of atlas based (red), transformed atlas based (blue) and graph cut based segmentations of the ventricles at age range 3 using penalty 1 (light green), penalty 2 (dark green) and penalty 3 (purple).

cut based segmentations computed using penalty terms 1, 2 and 3. At age range 1 only at GD 158 the graph cut refinement using penalty 1 and 3 shows an increased DC of about 0.04. A maximal DC decrease of about 0.02 at GD 151 and 164 is observed. The highest DC is achieved at GD 151 with a value of about 0.592. At age range 2 no improvement of the DC of ventricle segmentations is achievable. One reason is the decrease of the DC after pairwise registration. The regularisation kernel for cortical segmentations is not suitable for the pairwise registration of ventricle segmentations at age range 2. A maximal DC decrease of about 0.08 is achieved at GD 184 between atlas based and graph cut based segmentations. The highest DC is achieved at GD 171 with a value of 0.464. At age range 3 an improvement between atlas-based and graph cut based segmentations using penalisation 1 is observable from GD 184 to 191 and from GD 203 to 210 with an DC increase between 0.02 and 0.07. At GD 197 the lowest DC of about 0.068 is reached. The highest DC at age range 3 is observed at GD 210 with a value of 0.503 using penalty 1.

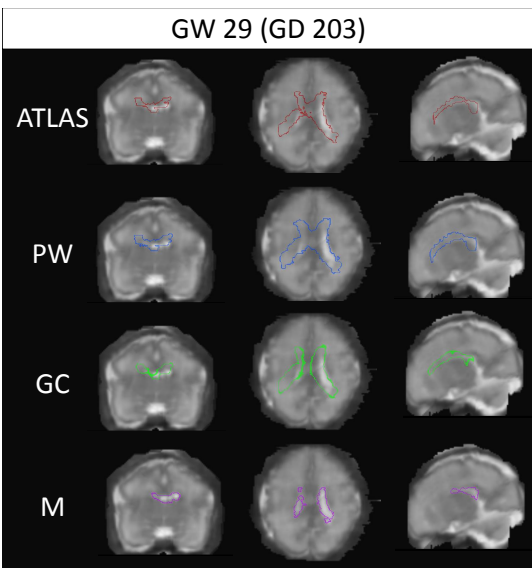
Figure 7.27 illustrates the test data at gestational age GD 158, 171 and 203 and corresponding estimated segmentations of ventricle tissue. The graph cut estimations are computed using the penalty 3 term. Atlas-based (red), transformed atlas based by pairwise registration (blue), graph cut based (green) and manual segmentations (purple) are visualised. Coronal slices are illustrated in the first column, axial slices in the second and sagittal slices in the third. The atlas based segmentations of ventricle structure at GD 158 show a bigger volume compared to the manual annotations and a displacement to the right. The graph cut based segmentation is able to improve the segmentation of the superior and inferior part of the CSP and lateral ventricles,



(a) GD 158



(b) GD 171



(c) GD 203

Figure 7.27: Segmentations of the ventricle at GD 158, 171 and 208 estimated by the atlas (red), after the pairwise registration procedure (blue), estimated by the graph cut approach (green) and manual annotations (purple).

visible as thinning at coronal slices. On the sagittal slices a more accurate graph cut based labeling of the inferior part of the ventricle's frontal horn is visible, compared to the temporal lobe adjacent part. At age range 2 the ventricle segmentation shows a refinement from atlas to graph cut similar to the manual annotations and is best visible in the axial and sagittal slices. At the coronal slices a displacement of atlas based segmentations to the left is visible, this leads to a thinning of the segmentations in the graph cut approach, since pairwise registration is not

capable of compensating these differences. At GD 203 the atlas based ventricle segmentations show a bigger volume compared to the manual segmentations. Pairwise registration leads to a wider segmentation border instead of compensating the volume differences. At the axial slices it is observed that the atlas estimates an entire ventricle segmentation from left to right, in contrast to the manual segmentations which show two regions. The graph cut refinement is capable to obtain two separate structures, which show an alignment of the left segmentation borders to the ventricle structure (axial slice). The occipital part of the graph cut based segmentation in the sagittal slice shows a low deviation from the manual segmentations, but illustrates a false segmentation towards the frontal lobe.

7.3 Summary and Contributions

The contribution of this work lies in the proposing of an automatic tissue labeling framework by integrating a continuous, quantifiable model of brain development and an automated labeling procedure. For that a suitable registration technique to learn a spatio-temporal fetal brain atlas has to be identified and its incorporation in an automatic tissue labeling framework has to be evaluated.

Continuous, Quantifiable Model of Brain Development

Research Questions:

Is geodesic image regression a suitable technique to learn a longitudinal atlas for fetal brains?
Is a preprocessing pipeline necessary? Is it possible to model the changes of the fetal brain in size and morphology over time?

The analysis of state-of-the-art approaches show that geodesic image regression is a suitable longitudinal registration technique (cf. Chapter 2). This is capable to model fetal brain development continuously in time without combining a template and an interpolation technique. Instead a time dependent vector field is estimated, which computation requires a preprocessing pipeline (corresponding analysis cf. Chapter 5 and structure cf. Chapter 6). As contribution to this thesis a novel longitudinal registration scheme using three age ranges is developed and evaluated, which enables the parametrisation of the vector field regularisation dependent on the developmental stage of the fetal brains. In this chapter the evaluation of 21 different vector field regularisations per age range for atlas learning is documented. It is observed that age range dependent regularisation is necessary to obtain improved registration results. The computed time-dependent vector field is able to transform segmentations of the cortex or the ventricles continuously in time to compute age dependent atlas based segmentations. The learned time dependent vector field is able to model the changes in shape and size of the cortex and its folding (cf. Section 7.1). Compared to the cortical structure, the ventricular structure shrinks from age range 1 to age range 3. Since the proposed method uses one regularisation type per age range, it is identified that geodesic regression is not able to regularise location specific volume expansion and shrinkage at the same time. Thus, according to these results tissue and age range specific regularisation are required to model fetal brain development using geodesic regression.

Automatic Tissue Labeling Procedure

Research Questions:

How to create an automatic tissue labeling framework for fetal brains? How can atlas-based segmentations be used as an initialisation term of a graph cut approach? Are segmentation refinements achievable using a graph cut?

The integration of the atlas learned in a segmentation framework is designed in the following way: In the course of this thesis geodesic shooting is identified as suitable technique to map estimated time-dependent atlas based segmentations and templates of the cortex and ventricle to the space of a subject. Also for pairwise geodesic shooting registration different regularisation parameters are evaluated (cf. Section 7.2). The results show that also tissue dependent regularisation is necessary to obtain an improved segmentation result. It is observed that a segmentation refinement of atlas-based segmentations is achievable using a graph cut approach, but is dependent on the result of the pairwise registration procedure. It has influence on the graph cut based labeling, since the transformed atlas based segmentations are used as tissue specific prior maps.

7.4 Conclusion

In this master's thesis an automatic fetal brain tissue labeling framework is presented. According to the analysis of the state-of-the-art approaches, geodesic image regression for time-series has been evaluated only using adult- and child-brain datasets, which record changes of brain structure over time. In the course of this work this technique is identified to also be suitable as registration approach to longitudinally model the changes in size and shape of the brain during the 18th and 30th GW. One advantage of this approach is the diffeomorphic formulation of the deformation model, which preserves smooth structures and obtains physically valid templates - an important fact in the medical field. A further advantage is the provision of a time-dependent transformation from a source to a target brain, instead of combining a template building technique and interpolation technique to obtain continuity in time. The analysis of diffeomorphic registration shows that rigid alignment, masking and motion correction are needed as preprocessing steps to perform longitudinal registration and to reduce registration errors. For analysing the atlas learning procedure, three registration schemes are created, where the scheme that uses three separate age ranges performs best. Instead of registering the whole dataset at once, separate age ranges show more flexibility in parametrising the regularisation of the deformation model due to the age range dependent changes, like cortical folding and rapid brain growth and consequently achieve improved results. The atlas learned is evaluated using a leave-one-out cross validation approach for every age range and 21 different regularisation kernels are analysed according to their behaviour regarding volume expansion, modelling of cortical surface and Dice similarity to manual annotations. The fetal brain atlas proposed is not capable of modelling the shrinkage or thinning of ventricles from age range 1 to age range 3. Since the proposed method uses one regularisation kernel per age range, geodesic regression is not able to regularise location specific volume expansion and shrinkage at the same time. To overcome this issue, the usage of tissue specific regularisation and consequently the computation of separate ventricle atlases

are a possible solution. In contrast to this, the increase of the cortical folding grade and of the volume over time are integrated in the proposed longitudinal model. The labeling of cortex and ventricles is included in the presented automatic tissue labeling framework, by propagating the atlas based segmentation to the space of a new subject using pairwise geodesic registration. The transformed annotations are used as a probability map for a graph cut approach with a CMF formulation to refine the annotations. For pairwise registration the same 21 regularisation kernels, which are used in the longitudinal registration procedure are evaluate but show no improvement of the DC of atlas-based segmentations over time. Thus, an additional kernel is defined and used for every age range. The quality of transformed atlas based segmentations to subject's space using pairwise registration leads to the conclusion that the kernel for pairwise registration has to be defined differently according to the age range and also tissue type, for being able to improve the graph cut initialisation term. Additionally it is shown that the quality of graph cut labeling is dependent on the initialisation cost term (atlas segmentation) and the penalty term. A false or displaced atlas segmentation hinders as cost term the refinement of graph cut based labeling. Finally the proposed automatic tissue labeling framework is able to estimate cortex segmentations with a DC up to 0.85 and ventricle segmentations up to 0.60. This master's thesis shows that image regression is also capable to model the variability of fetal brains in time and is qualified to be used for building a spatio-temporal atlas as basis for fetal brain tissue segmentation.

7.5 Future Work

For this master's thesis the possible future work lies in the following fields:

- Different datasets
- Classification of fetal developmental stadium
- Model of the developing cortical surface
- Improvement of preprocessing
- Model additional brain structures
- Atlas based initialisation and labeling

The focus of this thesis lies on building a spatio-temporal model of the healthy fetal brain using MRI volumes. Regarding the healthy cases, additional data of a wider age range can be added to study early brain development at GW smaller 18 or for example the cortical folding appearing after GW 30. An adaptation of the model for studying brain affecting diseases during pregnancy is possible using a dataset containing also pathological cases. Also the combination of MRI and functional MRI datasets of the fetal brain can be considered in future works for studying signal perception and localisation or to identify multi-variate patterns of brain activity. For future work the learned continuous model of brain development can be used for training a classifier (Random Forest, Markov Random Field, Support Vector Machine) to identify the developmental stage of a fetal brain and additionally to estimate the deviation from a brain at a certain gestational age.

Also including additional shape descriptors, like gyrification index and measures for surface curvature can be used to predict fetal age and to study cortical folding patterns. The evaluation of the cortical labeling results for age range 1, 2 and 3 show that a single kernel for pairwise registration for every age range is not suitable. The estimation of age range dependent regularisation will be a main issue for the improvement of the labeling procedure and consequently the quality of graph cut based segmentation. Additionally a combination of global rigid and local deformable pairwise registration could be analysed for transforming atlas based segmentations to the subject's space as extension to this thesis. A further field for future work lies in the combination of atlas based initialisation with other segmentation approaches or in the usage of atlas based segmentations for the definition of relations between tissue structures to refine the probabilities of tissue labeling. An automatic localisation of fetal brain and eyes can be included in the preprocessing pipeline for improving the automatic alignment. An additional refinement of the masking procedure can be achieved by analysis of the surrounding mother tissue to identify fetal tissue. Since the dataset used in this thesis was annotated by one expert, the resulting annotation bias can be reduced by incorporating more experts in the labeling procedure. Also additional brain structures can be studied for future work, by labeling e.g. CSF, GMAT GM and WM, cerebellum or medulla oblungata.

APPENDIX A

Acronyms

ADNI Alzheimer's Disease Neuroimaging Initiative

CaS Calcarine Sulcus

CeS Central Sulcus

CiS Cingulate Sulcus

CLS ColLateral Sulcus

CMF Continuous Max-Flow

CSF CerebroSpinal Fluid

CSP Cavum of Septum Pellucidum

CT Computer Tomography

DARTEL Diffeomorphic Anatomical RegistratiOn using Exponential Lie algebra

DC Dice Coefficient

FFT Fast Fourier Transformation

FL Frontal Lobe

FN False Negative

FP False Positive

FSE Fast Spin-Echo

GA Gestational Age

GD Gestational Days

GM Gray Matter

GMAT Germinal MATrix

GUI Graphical User Interface

GW Gestational Week

IHF InterHemispheric Fissure

LDDMM Large Deformation Diffeomorphic Metric Mapping

L-VENT Lateral VENTricle

MR Magnetic Resonance

MRI Magnetic Resonance Imaging

ODE Ordinary Differential Equation

OL Occipital Lobe

PET Positron Emission Tomography

PL Parietal Lobe

POS ParietoOccipital Sulcus

PostCG PostCentral Gyrus

PreCG PreCentral Gyrus

SF Sylvian Fissure

SSFSE Single Shot Fast Spin-Echo

TP True Positive

TN True Negative

WM White Matter

Bibliography

- [1] J. Ashburner. A fast diffeomorphic image registration algorithm. *NeuroImage*, 38(1):95–113, October 2007.
- [2] J. Ashburner and K.J. Friston. Diffeomorphic registration using geodesic shooting and Gauss-Newton optimisation. *NeuroImage*, 55(3):954–967, April 2011.
- [3] J. Ashburner and G.R. Ridgway. Symmetric diffeomorphic modeling of longitudinal structural MRI. *Brain Imaging Methods*, 6:197, 2013.
- [4] M. Bach Cuadra, M. Schaer, A. Andre, L. Guibaud, S. Eliez, and J.-Ph. Thiran. Brain tissue segmentation of fetal MR images. In *Workshop on Image Analysis for Developing Brain, in 12th International Conference on Medical Image Computing and Computer Assisted Intervention*, 2009.
- [5] M. Becker and N. Magnenat-Thalmann. Deformable models in medical image segmentation. In N. Magnenat-Thalmann, O. Ratib, and H.F. Choi, editors, *3D Multiscale Physiological Human*, pages 81–106. Springer London, January 2014.
- [6] M.F. Beg, M.I. Miller, A. Trouvé, and L. Younes. Computing large deformation metric mappings via geodesic flows of diffeomorphisms. *International Journal of Computer Vision*, 61(2):139–157, February 2005.
- [7] F.E. Bloom, M.F. Beal, and D.J. Kupfer. *The Dana Guide to Brain Health a Practical Family Reference from Medical Experts*. Dana; University Presses Marketing [distributor], New York; Bristol, 2006.
- [8] Y. Boykov and O. Veksler. Graph cuts in vision and graphics: Theories and applications. In N. Paragios, Y. Chen, and O. Faugeras, editors, *Handbook of Mathematical Models in Computer Vision*, pages 79–96. Springer US, January 2006.
- [9] L. Breysem, H. Bosmans, S. Dymarkowski, D. Van Schoubroeck, I. Witters, J. Deprest, P. Demaerel, D. Vanbeckevoort, C. Vanhole, P. Casaer, and M. Smet. The value of fast MR imaging as an adjunct to ultrasound in prenatal diagnosis. *European Radiology*, 13(7):1538–1548, July 2003.
- [10] K. Briechle and U.D. Hanebeck. Template matching using fast normalized cross correlation. *Proc. SPIE*, 4387:95–102, 2001.

- [11] R. Brooks. A quantitative theory of the hounsfield unit and its application to dual energy scanning. *Journal of Computer Assisted Tomography*, 1(4):487–493, October 1977.
- [12] P.C. Brugger. Methods of fetal MRI. In D. Prayer, editor, *Fetal MRI*, Medical Radiology, pages 65–80. Springer Berlin Heidelberg, 2010.
- [13] S.C. Bushong. *Magnetic Resonance Imaging*. Mosby, St. Louis, Mo.; London, 2003.
- [14] M. Cabezas, A. Oliver, X. Lladó, J. Freixenet, and M. Bach Cuadra. A review of atlas-based segmentation for magnetic resonance brain images. *Computer Methods and Programs in Biomedicine*, 104(3):e158–e177, December 2011.
- [15] T. Chapman, M. Matesan, E. Weinberger, and D.I. Bulas. Digital atlas of fetal brain MRI. *Pediatric Radiology*, 40(2):153–162, September 2009.
- [16] M.M. Chen, F.V. Coakley, A. Kaimal, and R.K.Jr Laros. Guidelines for computed tomography and magnetic resonance imaging use during pregnancy and lactation. *Obstetrics & Gynecology August 2008*, pages 333–340, 2008.
- [17] I. Claude and J.-L. and Sebag, G. Daire. Fetal brain MRI: segmentation and biometric analysis of the posterior fossa. *IEEE transactions on bio-medical engineering*, 51(4):617–626, April 2004.
- [18] M. Clemence. How to shorten MRI sequences. In D. Prayer, editor, *Fetal MRI*, Medical Radiology, pages 19–32. Springer Berlin Heidelberg, 2011.
- [19] C. Clouchoux, A.J. du Plessis, M. Bouyssi-Kobar, W. Tworetzky, D.B. McElhinney, D.W. Brown, A. Gholipour, D. Kudelski, S.K. Warfield, R.J. McCarter, R.L. Robertson, A.C. Evans, J.W. Newburger, and C. Limperopoulos. Delayed cortical development in fetuses with complex congenital heart disease. *Cerebral Cortex (New York, N.Y.: 1991)*, 23(12):2932–2943, December 2013.
- [20] C. Clouchoux, D. Kudelski, A. Gholipour, S.K. Warfield, S. Viseur, M. Bouyssi-Kobar, J.-L. Mari, A.C. Evans, A.J. du Plessis, and C. Limperopoulos. Quantitative in vivo MRI measurement of cortical development in the fetus. *Brain Structure & Function*, 217(1):127–139, January 2012.
- [21] W.R. Crum, T. Hartkens, and D.L.G. Hill. Non-rigid image registration: Theory and practice. *The British Journal of Radiology*, 77 Spec(2):140–153, 2004. PMID: 15677356.
- [22] L.R. Dice. Measures of the amount of ecologic association between species. *Ecology*, 26(3):297–302, July 1945.
- [23] E. Dittrich. *Assesing Fetal Brain Development Based on a Spatio-Temporal in vivo Atlas Learned from Ultra-Fast Magnetic Resonance Images*. PhD thesis, Medical University of Vienna, Computational Imaging Research (CIR) Lab, 2012.

- [24] P. Dupuis and U. Grenander. Variational problems on flows of diffeomorphisms for image matching. *Q. Appl. Math.*, LVI(3):587–600, 1998.
- [25] S. Durrleman, X. Pennec, A. Trouvé, J. Braga, G. Gerig, and N. Ayache. Toward a comprehensive framework for the spatiotemporal statistical analysis of longitudinal shape data. *International Journal of Computer Vision*, 103(1):22–59, May 2013.
- [26] S.F. Eskildsen, P. Coupé, V. Fonov, J.V. Manjón, K.K. Leung, N. Guizard, S.N. Wassef, L.R. Østergaard, D.L. Collins, and Alzheimer’s Disease Neuroimaging Initiative. BEaST: brain extraction based on nonlocal segmentation technique. *NeuroImage*, 59(3):2362–2373, February 2012.
- [27] M. Esteghamatian, Z. Azimifar, P. Radau, and G. Wright. Real time cardiac image registration during respiration: a time series prediction approach. *Journal of Real-Time Image Processing*, 8(2):179–191, May 2011.
- [28] A.C. Evans, D.L. Collins, S.R. Mills, E.D. Brown, R.L. Kelly, and T.M. Peters. 3D statistical neuroanatomical models from 305 MRI volumes. In *Nuclear Science Symposium and Medical Imaging Conference, 1993., 1993 IEEE Conference Record.*, volume 3, pages 1813–1817, 1993.
- [29] J. Fishbaugh, M. Prastawa, G. Gerig, and S. Durrleman. Geodesic image regression with a sparse parameterization of diffeomorphisms. In F. Nielsen and F. Barbaresco, editors, *Geometric Science of Information*, number 8085 in Lecture Notes in Computer Science, pages 95–102. Springer Berlin Heidelberg, January 2013.
- [30] A. Gholipour, A. Akhondi-Asl, J.A. Estroff, and S.K. Warfield. Multi-atlas multi-shape segmentation of fetal brain MRI for volumetric and morphometric analysis of ventriculomegaly. *NeuroImage*, 60(3):1819–1831, April 2012.
- [31] A.A. Goshtasby. *2-D and 3-D Image Registration: for Medical, Remote Sensing, and Industrial Applications*. Wiley-Interscience A John Wiley & Sons, Inc., Publication, London, 1. edition, 2005.
- [32] P. Gowland. Safety of fetal MRI scanning. In D. Prayer, editor, *Fetal MRI*, pages 49–54. Springer Berlin Heidelberg, Berlin, Heidelberg, 2010.
- [33] P.A. Habas, K. Kim, J.M. Corbett-Detig, F. Rousseau, O.A. Glenn, A.J. Barkovich, and C. Studholme. A spatiotemporal atlas of MR intensity, tissue probability and shape of the fetal brain with application to segmentation. *NeuroImage*, 53(2):460–470, November 2010.
- [34] P.A. Habas, K. Kim, F. Rousseau, O.A. Glenn, A.J. Barkovich, and C. Studholme. A spatiotemporal atlas of the human fetal brain with application to tissue segmentation. *Medical image computing and computer-assisted intervention : MICCAI International Conference on Medical Image Computing and Computer-Assisted Intervention*, 12(Pt 1):289–296, 2009.

- [35] P.A. Habas, K. Kim, F. Rousseau, O.A. Glenn, A.J. Barkovich, and C. Studholme. Atlas-based segmentation of developing tissues in the human brain with quantitative validation in young fetuses. *Human Brain Mapping*, 31(9):1348–1358, September 2010.
- [36] M. Hazewinkel. *Encyclopaedia of Mathematics*. Springer-Verlag, Berlin; New York, 2002.
- [37] R.K. Hobbie and B.J. Roth. *Intermediate Physics for Medicine and Biology*. Springer, New York, 2007.
- [38] Y. Hong, Y. Shi, M. Styner, M. Sanchez, and M. Niethammer. Simple geodesic regression for image time-series. In B.M. Dawant, G.E. Christensen, J.M. Fitzpatrick, and D. Rueckert, editors, *Biomedical Image Registration*, number 7359 in Lecture Notes in Computer Science, pages 11–20. Springer Berlin Heidelberg, January 2012.
- [39] J. Hu, M. Grossberg, and G. Mageras. Survey of recent volumetric medical image segmentation techniques. In C.A. Barros de Mello, editor, *Biomedical Engineering*. InTech, October 2009.
- [40] K. Keraudren, M. Kuklisova-Murgasova, V. Kyriakopoulou, C. Malamateniou, M. A. Rutherford, B. Kainz, J.V. Hajnal, and D. Rueckert. Automated fetal brain segmentation from 2D MRI slices for motion correction. *NeuroImage*, 101:633–643, November 2014.
- [41] K. Kim, P.A. Habas, F. Rousseau, O.A. Glenn, A.J. Barkovich, and C. Studholme. Intersection based motion correction of multislice MRI for 3-D in utero fetal brain image formation. *IEEE Transactions on Medical Imaging*, 29(1):146–158, January 2010.
- [42] M. Kuklisova-Murgasova, P. Aljabar, L. Srinivasan, S.J. Counsell, V. Doria, A. Serag, I.S. Gousias, J.P. Boardman, M.A. Rutherford, A.D. Edwards, J.V. Hajnal, and D. Rueckert. A dynamic 4D probabilistic atlas of the developing brain. *NeuroImage*, 54(4):2750–2763, February 2011.
- [43] M. Kuklisova-Murgasova, G. Quaghebeur, M.A. Rutherford, J.V. Hajnal, and J.A. Schnabel. Reconstruction of fetal brain MRI with intensity matching and complete outlier removal. *Medical Image Analysis*, 16(8):1550–1564, December 2012.
- [44] K. Leithner. The psychic state of the pregnant woman and prenatal diagnostic procedures. In D. Prayer, editor, *Fetal MRI*, Medical Radiology, pages 55–64. Springer Berlin Heidelberg, 2010.
- [45] K.T.-K. Leung. *Principal Ranking Meta-algorithms*. PhD thesis, University of California at Los Angeles, Los Angeles, CA, USA, 2010. AAI3452137.
- [46] F.P. Li, M. Rajchl, J.A. White, A. Goela, and T.M. Peters. Generation of synthetic 4D cardiac CT images for guidance of minimally invasive beating heart interventions. In D. Barratt, S. Cotin, G. Fichtinger, P. Jannin, and N. Navab, editors, *Information Processing in Computer-Assisted Interventions*, number 7915 in Lecture Notes in Computer Science, pages 11–20. Springer Berlin Heidelberg, January 2013.

- [47] G. Li, L. Wang, F. Shi, A.E. Lyall, W. Lin, J.H. Gilmore, and D. Shen. Mapping Longitudinal Development of Local Cortical Gyrification in Infants from Birth to 2 Years of Age. *The Journal of Neuroscience*, 34(12):4228–4238, March 2014.
- [48] S. Liao, H. Jia, G. Wu, D. Shen, and The Alzheimer’s Disease Neuroimaging Initiative. A novel framework for longitudinal atlas construction with groupwise registration of subject image sequences. *NeuroImage*, 59(2):1275–1289, January 2012.
- [49] H. Lippert and T. Deller. *Lehrbuch Anatomie*. Urban & Fischer, Munich, 6. edition, 2003.
- [50] N. Magnenat-Thalmann, H.F. Choi, and D. Thalmann. Towards effective diagnosis and prediction via 3D patient model: A complete research plan. In N. Magnenat-Thalmann, O. Ratib, and H.F. Choi, editors, *3D Multiscale Physiological Human*, pages 3–22. Springer London, January 2014.
- [51] J.B.A. Maintz and M.A. Viergever. A survey of medical image registration. *Medical Image Analysis*, 2(1):1–36, March 1998.
- [52] M.I. Miller, A. Trouvé, and L. Younes. Geodesic shooting for computational anatomy. *Journal of Mathematical Imaging and Vision*, 24(2):209–228, March 2006.
- [53] M. Mongelli and J. Gardosi. Birth weight, prematurity and accuracy of gestational age. *International Journal of Gynecology & Obstetrics*, 56(3):251–256, March 1997.
- [54] M. Niethammer, Y. Huang, and F.X. Vialard. Geodesic regression for image time-series. *Medical image computing and computer-assisted intervention: MICCAI International Conference on Medical Image Computing and Computer-Assisted Intervention*, 14(Pt 2):655–662, 2011.
- [55] R. O’Rahilly and F. Müller. Neurulation in the normal human embryo. In CIBA Foundation Symposium, editor, *Neural Tube Defects*, pages 70–82. John Wiley & Sons, Institut für Anatomie und Spezielle Embryologie, Universität Freiburg, Freiburg, Switzerland, 1994.
- [56] M. Prastawa, J.H. Gilmore, W. Lin, and G. Gerig. Automatic segmentation of MR images of the developing newborn brain. *Medical Image Analysis*, 9(5):457–466, October 2005.
- [57] D. Pugash, U. Nemec, P.C. Brugger, and D. Prayer. Fetal MRI of Normal Brain Development. In D. Prayer, editor, *Fetal MRI*, Medical Radiology, pages 147–175. Springer Berlin Heidelberg, January 2011.
- [58] L. Risser, F.-X. Vialard, A. Serag, P. Ajabar, and D. Rueckert. Construction of diffeomorphic spatio-temporal atlases using Kärcher means and LDDMM: Application to early cortical development. In *Workshop on Image Analysis of Human Brain Development (IAHBD), in MICCAI International Conference on Medical Image Computing and Computer Assisted Intervention*, September 2011.

- [59] N.M. Roelfsema, W.C.J. Hop, S.M.E. Boito, and J.W. Vladimiroff. Three-dimensional sonographic measurement of normal fetal brain volume during the second half of pregnancy. *American Journal of Obstetrics and Gynecology*, 190(1):275–280, January 2004.
- [60] F. Rousseau, E. Oubel, J. Pontabry, M. Schweitzer, C. Studholme, M. Koob, and J. Dietemann. BTK: An Open-Source Toolkit for Fetal Brain MR Image Processing. *Computer methods and programs in biomedicine*, 109(1):65–73, January 2013.
- [61] D. Ruan, J.A. Fessler, M. Roberson, J. Balter, and M. Kessler. Nonrigid registration using regularization that accommodates local tissue rigidity. *Proc. SPIE*, 6144:614412–1–614412–9, 2006.
- [62] J. Santamaría, O. Cordón, and S. Damas. A comparative study of state-of-the-art evolutionary image registration methods for 3D modeling. *Computer Vision and Image Understanding*, 115(9):1340–1354, September 2011.
- [63] T. Saul, R. E. Lewiss, and M.D.R. Rivera. Accuracy of emergency physician performed bedside ultrasound in determining gestational age in first trimester pregnancy. *Critical Ultrasound Journal*, 4(1):1–5, December 2012.
- [64] J.A. Scott, P.A. Habas, K. Kim, V. Rajagopalan, K.S. Hamzelou, J.M. Corbett-Detig, A.J. Barkovich, O.A. Glenn, and C. Studholme. Growth trajectories of the human fetal brain tissues estimated from 3D reconstructed in utero MRI. *International Journal of Developmental Neuroscience*, 29(5):529–536, August 2011.
- [65] A. Serag, P. Aljabar, G. Ball, S.J. Counsell, J.P. Boardman, M.A. Rutherford, A.D. Edwards, J.V. Hajnal, and D. Rueckert. Construction of a consistent high-definition spatio-temporal atlas of the developing brain using adaptive kernel regression. *NeuroImage*, 59(3):2255–2265, February 2012.
- [66] A. Serag, P. Aljabar, S. Counsell, J. Boardman, J.V. Hajnal, and D. Rueckert. LISA: Longitudinal image registration via spatio-temporal atlases. In *2012 9th IEEE International Symposium on Biomedical Imaging (ISBI)*, pages 334–337, May 2012.
- [67] A. Serag, V. Kyriakopoulou, M.A. Rutherford, A.D. Edwards, J.V. Hajnal, P. Aljabar, S.J. Counsell, J.P. Boardman, and D. Rueckert. A multi-channel 4D probabilistic atlas of the developing brain: Application to fetuse and neonates. *Annals of the BMVA*, 2012(3):1–14, 2012.
- [68] N. Singh, J. Hinkle, S. Joshi, and P.T. Fletcher. A vector momenta formulation of diffeomorphisms for improved geodesic regression and atlas construction. In *2013 IEEE 10th International Symposium on Biomedical Imaging (ISBI)*, pages 1219–1222, April 2013.
- [69] J.G. Sled, A.P. Zijdenbos, and A.C. Evans. A nonparametric method for automatic correction of intensity nonuniformity in MRI data. *IEEE transactions on medical imaging*, 17(1):87–97, February 1998.

- [70] F.W. Smith, A.H. Adam, and W.D.P. Phillips. NMR imaging in pregnancy. *The Lancet*, 321(8314-8315):61–62, January 1983.
- [71] S.M. Smith. Fast robust automated brain extraction. *Human Brain Mapping*, 17(3):143–155, November 2002.
- [72] A. Sotiras, C. Davatzikos, and N. Paragios. Deformable medical image registration: A survey. *IEEE Transactions on Medical Imaging*, 32(7):1153–1190, July 2013.
- [73] C. Studholme. Mapping fetal brain development in utero using magnetic resonance imaging: the big bang of brain mapping. *Annual review of biomedical engineering*, 13:345–368, August 2011.
- [74] J. Talairach and P. Tournoux. *Co-planar Stereotaxic Atlas of the Human Brain: 3-Dimensional Proportional System - an Approach to Cerebral Imaging*. Thieme Medical Publishers, New York, 1. edition, 1988.
- [75] A.W. Toga and P.M. Thompson. 1 - an introduction to maps and atlases of the brain. In A.W. Toga and J.C. Mazziotta, editors, *Brain Mapping: The Systems*, pages 3–32. Academic Press, San Diego, 2000.
- [76] A. Trouvè. An infinite dimensional group approach for physics based models in pattern recognition. Technical Report International Journal of Computer Vision - IJCV, center for imaging science, 1995.
- [77] N.J. Tustison, B.B. Avants, P.A. Cook, Y. Zheng, A. Egan, P.A. Yushkevich, and J.C. Gee. N4ITK: improved N3 bias correction. *IEEE transactions on medical imaging*, 29(6):1310–1320, June 2010.
- [78] F.X. Vialard, L. Risser, D. Rueckert, and C.J. Cotter. Diffeomorphic 3D image registration via geodesic shooting using an efficient adjoint calculation. *International Journal of Computer Vision*, 97(2):229–241, April 2012.
- [79] N.I. Weisenfeld and S.K. Warfield. Automatic segmentation of newborn brain MRI. *NeuroImage*, 47(2):564–572, August 2009.
- [80] R. Wright, V. Kyriakopoulou, C. Ledig, M.A. Rutherford, J.V. Hajnal, D. Rueckert, and P. Aljabar. Automatic quantification of normal cortical folding patterns from fetal brain MRI. *NeuroImage*, 91:21–32, May 2014.
- [81] H. Xue, L. Srinivasan, S. Jiang, M. Rutherford, A.D. Edwards, D. Rueckert, and J.V. Hajnal. Automatic segmentation and reconstruction of the cortex from neonatal MRI. *NeuroImage*, 38(3):461–477, November 2007.
- [82] J. Yuan, E. Bae, and X.-C. Tai. A study on continuous max-flow and min-cut approaches. In *2010 IEEE Conference on Computer Vision and Pattern Recognition (CVPR)*, pages 2217–2224, 2010.

- [83] J. Yuan, E. Bae, X.-C. Tai, and Y. Boykov. A continuous max-flow approach to potts model. In K. Daniilidis, P. Maragos, and N. Paragios, editors, *Computer Vision – ECCV 2010*, number 6316 in Lecture Notes in Computer Science, pages 379–392. Springer Berlin Heidelberg, January 2010.
- [84] J. Zhan, I.D. Dinov, J. Li, Z. Zhang, S. Hobel, Y. Shi, X. Lin, A. Zamanyan, L. Feng, G. Teng, F. Fang, Y. Tang, F. Zang, A.W. Toga, and S. Liu. Spatial-temporal atlas of human fetal brain development during the early second trimester. *NeuroImage*, 82:115–126, November 2013.
- [85] B. Zitová and J. Flusser. Image registration methods: A survey. *Image and Vision Computing*, 21(11):977–1000, October 2003.